Scuola Internazionale Superiore di Studi Avanzati - Trieste

DOCTORAL THESIS

Numerical Approaches Towards the Galactic Synchrotron Emission

CANDIDATE :   Jiaxin Wang

SUPERVISORS :   Prof. Piero Ullio

Dr. Francesca Perrotta

Abstract

The Galactic synchrotron emission contains abundant physics of the magnetized Galactic interstellar medium and has a non-negligible influence on detecting the B-mode polarization of the Cosmic microwave background radiation and understanding the physics during the re-ionization epoch. To catch up with the growing precision in astrophysical measurements, we need not only better theoretical modelings, but also more powerful numerical simulations and analyzing pipelines for acquiring deeper understandings in both the Galactic environment and the origin of the Universe. In this dissertation, we focus on the Galactic synchrotron emission which involves the turbulent and magnetized interstellar medium and energetic cosmic-ray electrons. To study the Galactic synchrotron emission consistently we need a non-trivial Bayesian analyzer with specially designed likelihood function, a fast and precise radiative transfer simulator, and cosmic ray electron propagation solver. We first present version X of the `hammurabi` package, the `HEALPix`-based numeric simulator for Galactic polarized emission. Two fast methods are proposed for realizing divergence-free Gaussian random magnetic fields either on the Galactic scale where a field alignment and strength modulation are imposed or on a local scale where more physically motivated models like a parameterized magneto-hydrodynamic turbulence can be applied. Secondly, we present our effort in using the finite element method for solving the cosmic ray (electron) transport equation within the phase-space domain that has a number of dimensions varying from two to six. The numeric package `BIFET` is developed on top of the `deal.II` library with support in the adaptive mesh refinement. Our first aim with `BIFET` is to build the basic framework that can support a high dimensional PDE solving. Finally, we introduce the work related to the complete design of `IMAGINE`, which is proposed particularly with the ensemble likelihood for inferring the distributions of Galactic components.

Keywords: methods: numerical; methods: statistical; ISM: cosmic rays; ISM: magnetic fields

Acknowledgment

My journey through the four years in astro-particle physics, computing science and Italy has been very pleasant. I am grateful to the PhD program in the astro-particle physics group of SISSA and the high-performance-computing master program conducted jointly by SISSA and ICTP, from which I have gained lots of knowledge and skills. As my PhD supervisors, Prof. Piero Ullio and Dr. Francesca Perrotta have shown me how to do science professionally. I have been inspired by the amazing physical intuition and strict attitude of Prof. Ullio, and started to have a better understanding of the path from an ignorant pupil to an independent scientist. The PhD project may not be carried out smoothly without the master program for high-performance-computing, from which I have been trained to be a programmer competent for numerical scientific tasks. I have to thank Prof. Luca Heltai who taught me the numerical analysis, the experience of working with him has always been very joyful and inspiring. I cannot imagine how could I survive the intensive training of the master program without the help from Dr. Alberto Sartori, who has always been a great friend and indispensable support for all the students in the master program. It was a great fortune of knowing Prof. François Boulanger, who introduced and recommended me to the IMAGINE consortium, and from where I met Prof. Tess R. Jaffe, Prof. Torsten A. Enßlin, Prof. Anvar Shukurov, Prof. Marijke Haverkorn and Dr. Theo Steininger. I do not think I could have been even more fortunate than collaborating with Prof. Jaffe and Prof. Enßlin. I am grateful to all my friends, office mates and colleagues in the theoretical-particle, astro-particle and astrophysical physics groups in SISSA, and from other institutes. Finally I would like to thank my parents and family for their unconditional support and love. In terms of the dissertation, I thank Prof. Dario Grasso and Prof. Marijke Haverkorn for reviewing the draft and providing precious comments and suggestions.

Abbreviations

AMR	adaptive mesh refinement
CR	cosmic ray
CRE	cosmic ray electron
CMB(R)	cosmic microwave background (radiation)
DM	dark matter
FFT	fast Fourier transform
FEM	finite element method
GMF	Galactic magnetic field
ISM	interstellar medium
ISRF	interstellar radiation field
LoS	line of sight
MHD	magneto hydrodynamics
MPI	message passing interface
PDE	partial differential equation
RMHD	radiation magneto hydrodynamics
SNR	supernova remnant
TE	thermal electron
UHECR	ultra high energetic cosmic ray

List of Publications

This thesis is based on the following publications and preprints, listed in chronological order:

- Inferring Galactic magnetic field model parameters using IMAGINE - An Interstellar MAGnetic field INference Engine, T. Steininger, et. al. , arXiv:1801.04341 .

- hammurabi X: Simulating Galactic Synchrotron Emission with Random Magnetic Fields, J. Wang, et. al. , arXiv:1907.00207 .

The research performed by the author during his PhD studies has also lead to the publication

- IMAGINE: A comprehensive view of the interstellar medium, Galactic magnetic fields and cosmic rays, F. Boulanger, et. al. , JCAP 08 (2018) 049 .

Contents

Introduction

In the past decades we have witnessed several exciting discoveries in physics like the detection of the Higgs particle [Aad et al., 2012], and of the gravitation waves emitted from the merging of black holes [Abbott et al., 2016], and the successful reconstruction of the black hole image of M87 [Akiyama et al., 2019]. Behind these thrilling advancements, we realize and acknowledge the power of collaboration not only in joining the brilliant minds but also in exploiting the numerical techniques and computing resources. As like the wisdom of a single man is always limited, there also exists a certain limitation of the conventional computing units beyond which the calculating frequency will be too high and the hardware starts to melt. It is the idea of parallel computing that came to save us from heavy numerical tasks, and the computing technique itself has become a subject to which scientists from all research fields have to pay serious attention. More and more frequently we have heard the word "state-of-art", which characterizes that although the physical phenomena are originated from simple and beautiful theories and mechanisms, the studies are going beyond the pure hand-written calculations and turning to either semi-analytic or pure numerical approaches, e.g., the non-linear and non-perturbative Galactic magnetic turbulence. Standing at the turning point of utilizing massive computing in astro-particle physics, I present, in this dissertation, our efforts in preparing the numerical tools for simulating and analyzing the Galactic synchrotron emission. In the following part of this introduction section, I would like to briefly overview our current understandings of the Galactic components and the connection between the Galactic emissions and the cosmic micro wave background radiation (CMBR), and introduce our concept of the consistent approach towards studying the Galaxy.

The Milky Way (or the Galaxy) we are living in is a typical spiral galaxy which mainly consists of a central bulge, thin and thick disks, and a low density stellar and dark matter (DM) halo with Virial radius extending to roughly larger than 100 kpc. In addition to focusing on the Galactic geometric structure (e.g., the shape of the Galactic disk spiral arms), our work about the Galactic emissions which contaminate the CMBR is more sensitive to the intrinsic properties of thermal interstellar medium (namely the cold/warm/hot thermal plasma, dust and photon field), the magnetic field and the Galactic cosmic rays (CRs), and the interaction among these three components. Here we emphasize the difference between CRs and the thermal interstellar medium (ISM) as the former is relativistic and having different chemical composition than the cold/warm/hot ISM phases. These three components together form a non-linear system, where we may also include implicitly the stellar evolution and feedback, as the star formation in the cold and dense molecular clouds results originally from the instability and cooling of the ISM.

It is believed that the magnetic field plays an important role (not dominant in the weak magnetic field case) in star formation along with the ISM turbulence [Hull et al., 2017]. The CRs are ejected mainly from luminous stars, supernova remnants, pulsars and even the jets of the extra-galactic black holes, and reshape the structure of GMF and thermal ISM which will give birth to young stars. CR particles with energy larger than around the EeV level, namely the ultra-high-energetic cosmic rays (UHECRs), are believed to come from extra-Galactic sources due to the fact that their high energy that cannot be hosted by the Galactic magnetic field strength, in addition, the anisotropic distribution of captured UHECRs reported by Aab et al. [2017] also suggests the extra-Galactic origin. In our study of Galactic emissions, the UHECRs are not considered since the energy is too high to produce the emission at the microwave band, nor to have strong feedback to the GMF, besides the density fraction is too small to exert significant influence on the ISM. The CRs with Galactic origins typically travels a long time in the Galaxy before escaping out or fragmenting/decaying into other particle species or getting trapped in a local region after losing sufficient energy. This is the main reason that the abundance of CR species differs from that produced by stellar evolution. It is the Galactic magnetic turbulence which scatters the CRs and in turn receives energy from the interaction and saturate by increasing the turbulent strength. The amplification of the magnetic turbulence by CR streaming happens mainly near the CR sources and the streaming speed of CRs with respect to the thermal ISM is limited. There are other amplification mechanisms as well, like the mean field dynamo on the Galactic scale. The magnetic field works on the ISM by shaping the motion and distribution of charged particles, whose electric current in turn determine the magnetic field itself. To resolve the Galactic ecology we need sufficient astrophysical measurements and precise and powerful numerical tools.

There are various tracers and probes for each phase of the Galactic components, e.g., the HI absorption and emission for cold and warm neutral ISM, the Hα emission for the ionized warm ISM and the X-ray for the hot ISM. Among which the synchrotron emission traces the distribution of both GMF and CRs. Note that the GMF permeates in different phases of the ISM and so does the CRs, however the shape and strength of GMF depends on the property of its ambient environment which also affect the propagation of CRs. In this way, we expect the synchrotron emission can carry information of the diffusive distribution of all three components. This is quite useful for studying the Galactic environment, since some probes cannot trace the Galactic environments deep into the thick disk or even to the halo.

Besides the intrinsic connection of the Galactic synchrotron emission to the ecology of the Galaxy, it influences the estimation of the CMBR intensity and polarization. Commonly the CMB detectors have spectral range from around 1 GHz to 500 GHz, where the CMB signal is suffering from contamination from the diffuse emissions of the Galaxy. At low frequency (< 100 GHz), the dominant pollution comes from the synchrotron emission of energetic electrons/positrons traversing the magnetized ISM and free-free emissions of thermal electrons. Whereas at high frequency (> 100 GHz), the pollution mainly comes from the polarized thermal emission of spinning dust grins aligned to the magnetic field orientation.

The standard approach for removing these foreground emissions is well known as the component separation [1] as summarized for example in Leach et al. [2008], Planck Collaboration et al. [2018a]. There

---

[1]Popular component separation methods list `https://lambda.gsfc.nasa.gov/toolbox/tb_comp_separation.cfm`.

are two categories of component separation, namely the blind and non-blind methods. In non-blind separation, either frequency scaling have to be modelled of various emissions, e.g., a power law for synchrotron emission intensity and grey-body spectrum for dust emission intensity or emission templates have to be prepared as external information. While in blind separation, e.g., with the analytical-blind-separation (ABS) method proposed recently by Zhang et al. [2019a], no emission template is required but contamination sources are assumed to be independent, or not if the foreground components are excluded from the output-set like the ABS method. The component separation methods so far have been very successful in extracting the CMB background and foreground (including diffuse and point sources) total intensity. While in the next breakthrough of CMB studies for discovering the CMB B-modes which is expected from the inflation theory, we need more precise removal of polarized Galactic emissions. The primordial gravitational waves, if exist, result in a tensor perturbation that can imprint a significant signal in the CMB B-modes. Naturally the B-modes can also be produced from the Galactic synchrotron and dust emissions which in turn contaminate the background signal. According to the closest attempt so far to the detection of CMB B-modes reported by Ade et al. [2015], the uncertainty in the foreground contamination (mainly from the Galactic dust emission) is still too large to provide a decisive conclusion we are waiting for. It was pointed out later by Krachmalnicoff et al. [2016] that the Galactic synchrotron contamination is also non-negligible for measuring the primordial gravitation waves with tensor-to-scalar ratio $r \sim 10^{-2}$ at frequency lower than 100 GHz.

Modelling the Galactic emissions analytically is possible but will sacrifice the precision required for doing detailed studies. For example, the distribution of Galactic magnetic turbulence is considered in average around the same strength as the regular magnetic field or even larger. Then the synchrotron emission will reflect this non-perturbative turbulence since the magnetic field contributes to the synchrotron emissivity and Faraday rotation (which becomes non-negligible at low frequency) non-linearly. What could be more important to CMB foreground removal is the varying of frequency scaling of polarized synchrotron emission from one angular direction to another. This is naturally caused by the fact that the CRE spectral distribution is not in reality a power law with a constant spectral index everywhere in the Galaxy and the Faraday rotation is not constant in line-of-sight (LoS) direction, nor in radial distance. An analytic approach to such a non-linear process can handle only the simple regular Galactic fields, while the turbulent/random fields can only be approximated by their ensemble mean theoretically. With numeric tools we should be able to look into various realizations and use more detailed modellings. Studies about Faraday rotation are facing a similar but more complicated situation, where the rotation of the photon polarization state during its traversing magnetized plasma is independent from its emission. Especially in cold and clumpy clouds or filaments, the rotation effect traces the geometrical structure of not only the thermal medium but also the magnetic field frozen within. The specific local shape of magnetic field near the solar neighbourhood has become a practical topic like the study of Alves et al. [2018] where the authors consider the regular magnetic field stretched with the local bubble shell. In general, we notice that it is the right time to start realistic modellings with numerical methods in calculating observables which could match the high precision in astrophysical measurements where many local and global structures, e.g., the local bubbles, north polar spurs, magnetic spiral arms and the Fermi bubbles,

have been discovered but not extremely well explained.

Beyond implementing and testing realistic modellings, we intend to build a physically consistent pipeline for the Galactic synchrotron emission. The generic design requires a numerical simulator which can produce the Galactic synchrotron emissions precisely and quickly with given field information. The field information may include the regular and turbulent Galactic magnetic field distribution, the thermal electron distribution, the cosmic ray electron/positron distribution in the phase-space domain.

For physically inconsistent studies, which is easier to implement with a certain cost in precision (and influences not only the CMB removal but also our understanding of the ISM), we can either model or construct all these Galactic fields independently. A non-parametric approach can remove the intrinsic inconsistency among the fields but the result depends highly on the quality and quantity of the measurements and is technically very expensive due to the high degrees of freedom in the discretization. While for consistent studies we define successively two studying levels according to the complexity in making non-linear connections between different Galactic components.

At the first level, we require the consistency between the cosmic ray electrons/positrons and the magnetic field distributions, where the Galactic synchrotron emission should match the synchrotron energy loss from the cosmic ray electrons/positrons while they are propagating (and have already reached the steady-state distribution) within the same magnetized ISM. Technically this requires a built-in cosmic ray (electron/positron) propagator inside the simulation workflow of the Galactic synchrotron emission. In addition to the synchrotron emission, if we want to bring dust emission into a joint analysis, we need to know that the dust distribution has certain influence on the CRs. At the first consistency level, dust distribution should be used in calculating the interstellar radiation fields (ISRFs), where the thermal dust grains absorb and polarize the starlight and emit polarized photons while spinning within the magnetic field (known as the polarized dust emission) which then interact with energetic cosmic ray electrons/positrons through the inverse-Compton scattering. The energy loss of cosmic ray electrons/positrons via inverse-Compton scattering is almost as important as its synchrotron energy loss and these two mechanisms dominate the cosmic ray electrons/positrons energy loss at high energy scale ($> 10 \text{GeV}$).

At the second consistency level, we need to fully consider the role of cosmic rays in the Galactic ecology. First of all, the cosmic ray propagation depends on how the energetic particles scatter off the magnetic field turbulence and amplify the field strength until reaching the saturation status where the streaming speed of cosmic rays with respect to the background plasma is thus bounded by a certain value. In this way the shape of the magnetic field turbulence and CRs distribution are both tuned by the non-linear interaction. Besides, the ISM (here we mainly consider dust and thermal electron) is affected by CRs which exert an extra pressure that supports the ISM (along with the ISM thermal and magnetic pressure) against the gravitational attraction. The second level is much more complicated since technically we have to consider the co-evolution of cosmic rays, magnetic field turbulence and thermal ISM with the first level consistency included.

* * *

This dissertation focuses on the first step towards the consistent but ambitious picture we proposed above, which is to build the numerical framework for the major computing tasks: a LoS emission/absorption/rotation integrator, a PDE system solver, and a Bayesian analyzer with specialized likelihood function. In Chap. 1 I will present the theoretical rules and two fast numerical methods in realizing and approximating the Galactic magnetic turbulence with Gaussian random field. To illustrate the observational implication of different features of the random magnetic fields, I will present in Chap. 2 the `hammurabi X` package designed for simulating the Galactic observables. In addition to which we will also discuss the new insights we have gathered from the Galactic synchrotron angular power spectrum with random magnetic fields. Chap. 3 is mainly about our attempt for building the numerical framework, `BIFET`, to solve the cosmic ray electron propagation by the finite element method within a high dimensional domain and adaptively refined mesh. In Chap. 4 I will present the complete design for `IMAGINE`, a novel Bayesian analysis package developed for inferring the Galactic components with various observables.

Chapter 1

Galactic magnetic field

1.1 Overview

The Galactic magnetic field itself can not be directly observed. Indirect measurement is the main obstacle of why we have not reached a detailed description of the Galactic magnetic field configuration. Generally speaking, each indirect Galactic magnetic field observable is related to only a certain property of the magnetic field and related to some extra information from other components in the Galaxy. The unknown aspects of the other physical quantities along with magnetic field in the indirect probes undermines the precision and performance of analyses. For example, in astrophysics the Zeeman splitting can be considered a quite clean observable for inferring the Galactic magnetic field (GMF) component parallel to the LoS direction [DAVIES et al., 1968], but it can only be measured from the neutral hydrogen which is not diffusive enough for inferring GMF coherently in the whole Galaxy [Fish et al., 2003]. To overcome this, we can try to reconstruct the shape and strength of the magnetic field by joint analysis of various astrophysical phenomena or probes. In the following we briefly overview the conventional and new methods in probing the GMF.

The conventional observables include the Zeeman splitting we mentioned above, starlight polarization, Faraday rotation (including the rotation measure synthesis), synchrotron and dust emissions. The deflection of ultra-high-energetic-cosmic-rays (UHECRs) is not considered, which is although promising in tracing the large scale structure of GMF but may not be precise enough due to the lack of knowledge about the source of UHECRs. The starlight polarization and dust emission both originated from the dust grains which tend to be aligned to the magnetic field. The starlight is partly linearly polarized (with extinction) parallel to the magnetic field due to the absorption of dust which also radiate polarized emission. Very recently, a joint analysis of dust emission and starlight absorption by Panopoulou et al. [2019] has pointed out that the polarization ability of dust grains has long been underestimated, suggesting that the future CMB foreground study can further confirm or challenge this. The synchrotron emission from cosmic ray electrons/positrons (CREs) acts as an unique diffuse tracer for both the magnetic field and the cosmic ray spectral shape from the Galactic disk to the halo. At low frequency (< 10 GHz), the synchrotron emission polarization receives a significant correction from the Faraday rotation which

also traces the magnetic field but weighted by the cold/warm ionized interstellar medium (ISM) between the emission source and the observer. The total Faraday depth itself can be a probe of GMF, by using the synthesized map provided in Oppermann et al. [2012], Hutschenreuter et al. [2018] according to extra-galactic point sources of Faraday rotation measurements. Or the Faraday rotation measure can be jointly analyzed with the rotation measure from pulsars in the Galaxy, by doing which a volume averaged estimation of GMF can be derived as discussed by Han et al. [2015]. In order to have a tomographic view of synchrotron emission with Faraday rotation, we could turn to the Faraday rotation measure synthesis [Brentjens and de Bruyn, 2005] which transform observable from the wavelength domain into the Faraday depth domain. By doing so we could distinguish the emission region from the rotation region and to know better the distribution of different phase in the ISM.

In addition to the conventional methods, two new observables for probing the Galactic magnetic field structure have been proposed recently. One is the velocity-space variation of neutral hydrogen orientation by using the Rolling Hough Transform (HI-RHT) introduced by Clark et al. [2014], where the linear structure within the diffuse hydrogen gas has been found with strong connection to the LoS magnetic field tangling. As demonstrated in Clark et al. [2015], Clark [2018] this method has comparable ability in mapping out the local Galactic magnetic field as the dust emission measurements. The other technique is the synchrotron intensity gradient (SIG) introduced by Lazarian et al. [2017] for detecting the emitting zone averaged magnetic field structure without being affected by the Faraday rotation. These two methods are helpful in tomographic studies for the Galactic environment in the future. The cold molecular and neutral gas can be traced by Faraday synthesis, the joint analysis of synchrotron polarization and SIG, Zeeman splitting, HI-RHT, joint analysis of dust emission and starlight polarization. Meanwhile, the synchrotron emission polarization is suitable for tracing the magnetized warm ionized medium.

Although with various tracers and probes for the Galactic magnetic field, we are moving slowly in theoretical modelling or numerical reconstructing its global and local structure. A major issue is that we do not know exactly what the global structure of the GMF should look like, partially due to our particular position in the Galactic disk. It is still an open question how the large scale structure of a galaxy is formed. A good candidate is the galactic (mean-field) dynamo theory [Chamandy et al., 2016], which is in analogy to the dynamo mechanism in planets and stars [Charbonneau, 2014] which has been well studied. There must be other important mechanisms, like the Biermann battery [Khanna, 1998] and Parker instability [Parker, 1966] (especially include cosmic ray transport as discussed by Heintz and Zweibel [2018]). On the other hand, the small scale magnetic field turbulence are better studied as reviewed by Han [2017], especially for the relation between the cold molecular filaments and the local magnetic field frozen within have been observed and explained in Li et al. [2013], Zhang et al. [2019b]. But more detailed understanding is missing, e.g., if the magnetic turbulence can be described by MHD turbulent modes, and the partition ratio of different modes in various ISM phase.

Despite our ignorance in many aspects of the Galactic field, its structure can be modelled phenomenologically at certain level to match a given observable, e.g., the Faraday rotation measure with dispersion measure from pulsars, the synchrotron and dust emissions from CMB measurements. Recent attempts in such modellings include the simplest logarithmic-spiral-arm model by Page et al. [2007], and more com-

plicated spiral structure descriptions like those in Sun et al. [2008], Jaffe et al. [2010, 2013] and Jansson and Farrar [2012a]. Although these models are quite simplified, we have got some basic clues about the regular component of GMF, e.g., the local direction of GMF is roughly pointing to the Galactic longitude 70°. The Galactic halo magnetic field is hard to infer, for which we have seen some efforts from Sun and Reich [2010], Jansson and Farrar [2012a], Ferrière and Terral [2014] and Terral and Ferrière [2017]. the existence of toroidal GMF structure in the Galactic halo but we are not certain whether it contains a dipole or quadruple symmetry mode or both. More up-to-date modellings seek physical motivations instead of pure phenomenological description. Alves et al. [2018] studied the possibility of Local Bubble motivated magnetic field structure near the solar neighbourhood with polarized dust emission. The Galactic dynamo [Shukurov, 2004] inspired modelling has just being brought up by Shukurov et al. [2019] for practical constraints with the IMAGINE consortium [1]. In terms of the turbulent component in GMF, Jansson and Farrar [2012b], Beck et al. [2016] and Vansyngel et al. [2018] have recently tried to get some detailed understandings through the implications of turbulent/random magnetic field. The difficulty of analyzing magnetic turbulent is not only from the requirement of accumulating observational data, but also proper theoretical modelling and numerical simulation. According to recent theoretical discussions made by Caldwell et al. [2016] and Kandel et al. [2017, 2018] where the authors tried to explain the synchrotron and dust B/E ratio with magneto-hydrodynamic turbulent modes, however the results are limited by several approximations for the convenience of analytic calculation.

The regular magnetic field is relatively easier to model and analyze, while the turbulent or random component relies more on numerical implementations where a large uncertainty may raise if we are not careful enough. According to these previous studies, we intend to investigate the properties of Galactic synchrotron emission with different random magnetic field realizations in order to understand the connection and guide future work in more details. But the first step should be introducing correct random magnetic field generators for realizing the Galactic magnetic turbulence in numerical simulation.

1.2   Random Field Realization

1.2.1   Conceptual Discussion

Realization (or in other words, approximation) of turbulent magnetic field is a major module in hammurabi X (which will be discussed in Chap. 2), since the correctness of most simulations relies on physically motivated and accurate description of the turbulent fields in the multi-phase ISM. In this section we present two Gaussian random GMF generators that are by definition divergence-free and capable of realizing field alignment and/or strength modulation on Galactic scales or an anisotropic power spectrum on small scales.

There are several criteria that a random GMF generator should satisfy. That it be divergence-free (or solenoidal) is always the prime feature of any magnetic field. Absolute zero divergence is hard to define under discretisation, but in principle either a vector-field decomposition or a Gram-Schmidt process in the frequency domain is capable of cleaning field divergence. In realistic cases when a large-scale spatial

---

[1] https://www.astro.ru.nl/imagine

domain is expected to be filled with random magnetic fields, the field strength and alignment need to be correlated with the large-scale structures in the Galaxy. This requirement complicates the generating process, because the divergence-free property should also be satisfied simultaneously. It is straightforward to generate a divergence-free Gaussian random field. It is also simple to then re-scale or stretch it as done in Jaffe et al. [2010]. But the latter process destroys the divergence-free property if it is just applied after the former one. A triple Fourier transform scheme is thus proposed mainly to reconcile these two requirements. At Galactic scales, the new scheme allows modification of the Gaussian random realization by a given inhomogeneous spatial profile for the field strength.

Note that aligning the magnetic field to a given direction is easy to implement in the spatial domain, but locally varying anisotropy in the energy power spectra is not feasible by a single fast Fourier transform. In studies of Galactic emission from MHD plasma, the dependency of local structure on a varying direction profile breaks the symmetry required for using the fast Fourier transformation. In order to perform more detailed modelling of the turbulent GMF power spectrum, we provide a local generator ('local' in the sense that the mean field can be approximated in uniform direction) with explicit or implicit vector decomposition.

1.2.2 Magnetic Power Spectrum

Analytic description for a random field usually consists of two components, i.e., its spatial profile and spectral power. The spatial profile is possibly determined by the turbulent source distribution (e.g., supernova explosions) or large-scale structures (e.g., spiral arms or molecular clouds) in the Galaxy. While the spectral power shape reflects more about the intrinsic properties of magnetic field turbulence like its spectral cascading or interaction with charged particles in the ISM.

Consider a magnetic field distribution $\mathbf{B}(\mathbf{x}) = \mathbf{B}_0(\mathbf{x}) + \mathbf{b}(\mathbf{x})$ and its counterpart $\tilde{\mathbf{B}}(\mathbf{k})$ in the frequency domain, where $\mathbf{B}_0$ and $\mathbf{b}$ represent regular and random field respectively. The simplest turbulent power spectrum is represented by the trace of the isotropic spectrum tensor in scalar form, $P(k)$ which if not specified is understood as the trace $\mathrm{Tr}[P_{ij}]$ of a spectrum tensor P_{ij}. A more detailed description may specify each element in P_{ij}, where the underlying Cartesian base can be defined by the wave-vector $\mathbf{k}$ in the frequency domain or a properly designed frame where off-diagonal terms in P_{ij} vanish. The trace representation $\mathrm{Tr}[P_{ij}]$ is widely used as a first approach to turbulent field realization where the spectral shape is important. In general we could parameterize the basic scalar spectrum as

$$
\begin{aligned}
P(k) \quad = \quad & P_0 \Big[(\frac{k_0}{k_1})^{\alpha_1} (\frac{k}{k_1})^6 \mathcal{H}(k_1 - k) \\
& + (\frac{k}{k_0})^{-\alpha_1} \mathcal{H}(k - k_1) \mathcal{H}(k_0 - k) \\
& + (\frac{k}{k_0})^{-\alpha_0} \mathcal{H}(k - k_0) \Big] ,
\end{aligned} \tag{1.1}
$$

where $\mathcal{H}$ represents a Heaviside step function as a convenient modelling for injection scale k_0, $\alpha \simeq 11/3$ if assuming a Kolmogorov spectrum. Note that although not explicitly written, a Nyquist frequency cutoff k_{nq} is inevitable in numeric realizations which can be described by multiplying an extra Heaviside factor $\mathcal{H}(k_{\mathrm{nq}} - k)$ in Eq. 1.1. The last term in Eq. 1.1 represents the forward magnetic cascading of MHD

turbulence from the injection scale k_0 to small scales ($k > k_0$), while the first two terms describes the inverse cascading [Pouquet et al., 1976] in MHD turbulence from k_0 to scale $k_1 \simeq 1/L$ which corresponds to the physical size L of the MHD system. According to the simulation results from Brandenburg et al. [2019], we set $k_1 = 0.1$ kpc^{-1} and $\alpha_1 = 0.0$ by default in this work if not specified.

For more physical parameterization, we are interested in realizing theoretical descriptions of turbulence in compressible plasma introduced and discussed by Cho and Lazarian [2002], Caldwell et al. [2016], Kandel et al. [2017, 2018]. In compressible plasma, turbulence can be decomposed into Alfvén, fast and slow modes. Two critical plasma status parameters are the ratio β and the Alfvén Mach number M_A. The plasma β is the ratio of gas pressure to magnetic pressure, which represents compressibility of the plasma, with $\beta \to \infty$ indicating the in-compressible regime. The Alfvén Mach number is the ratio of the injection velocity to the Alfvén velocity. $M_A > 1.0$ represents the super-Alfvénic regime, while $M_A < 1.0$ means sub-Alfvénic turbulence.

The general form of the compressible MHD magnetic field spectrum tensor trace [Kandel et al., 2018] can be described by decomposing it with the spectral shape function $P_i(k)$, the anisotropic shape function $F_i(M_A, \alpha)$ and $h_i(\beta, \alpha)$. The $P_i(k)$ and $h_i(\beta, \alpha)$ terms are naturally raised from solving the MHD equations as discussed in Cho and Lazarian [2002], while the $F_i(M_A, \alpha)$ term is used for characterizing the power anisotropy. So in general we have

$$P_i(k, \alpha) = P_i(k) F_i(M_A, \alpha) h_i(\beta, \alpha) , \tag{1.2}$$

$$P_i(k) = p_i \Big[\big(\frac{k_0}{k_1}\big)^{\alpha_1} \big(\frac{k}{k_1}\big)^6 \mathcal{H}(k_1 - k) \tag{1.3}$$

$$+ \big(\frac{k}{k_0}\big)^{-\alpha_1} \mathcal{H}(k - k_1) \mathcal{H}(k_0 - k)$$

$$+ \big(\frac{k}{k_0}\big)^{-\delta_i} \mathcal{H}(k - k_0) \Big] ,$$

$$h_A = 1 , \tag{1.4}$$

$$h_f = \frac{2}{D_{++}(1 + \tan^2 \alpha D_{-+}^2 / D_{+-}^2)} , \tag{1.5}$$

$$h_s = \frac{2}{D_{-+}(1 + \tan^2 \alpha D_{++}^2 / D_{--}^2)} , \tag{1.6}$$

$$D_{\pm\pm} = 1 \pm \sqrt{D} \pm 0.5\beta , \tag{1.7}$$

$$D = (1 + 0.5\beta)^2 - 2\beta \cos^2 \alpha , \tag{1.8}$$

$$F_f = 1 , \tag{1.9}$$

$$F_{A,s} = exp\{ -\frac{|\cos \alpha|}{(M_A^2 \sin \alpha)^{2/3}} \} , \tag{1.10}$$

where $i = \{A, f, s\}$ representing Alfvén, fast and slow modes respectively. In `hammurabi X`, compressible MHD is only realized by the local generator and so $\cos(\alpha) = \hat{\mathbf{k}} \cdot \hat{\mathbf{B}_0}$ is adopted with $\mathbf{B}_0$ taken as the regular field at the solar neighbourhood. In the sub-Alfvénic ($M_A < 1$) low-β ($\beta < 1$) regime, the spectral indices in Eq. 1.4 can be approximated as $\delta_A = \delta_s = 11/3$, and $\delta_f = 7/2$ [Cho and Lazarian, 2002]. The Alfvén speed v_a which should appear in $h_i(\alpha)$ is absorbed by the normalization factor p_i for simplicity.

1.2.3   Global Generator

One major task of `hammurabi X` is to generate a random GMF that can cover a specific scale in the spatial domain. However, an inhomogeneous correlation structure is not diagonal in the frequency domain. In this case, we try to impose an energy density and alignment profile in the spatial domain after the random realization is generated in the frequency domain with an isotropic spectrum. Then the field divergence can be cleaned back in frequency domain with the Gram-Schmidt process. The whole procedure of this scheme requires two backward and one forward fast Fourier transforms.

After a Gaussian random magnetic field is realized in the frequency domain, each grid point holds a vector $\mathbf{b}$ drawn from an isotropic field dispersion. The key of the triple transform is the large-scale alignment and energy density modulation process. The alignment direction $\hat{\mathbf{H}}$ at different Galactic positions should be pre-defined like the energy density profile. We introduce the alignment parameter ρ for imposing the alignment profile by

$$\mathbf{b}(\mathbf{x}) \quad \rightarrow \quad \frac{(\mathbf{b}_{\parallel}\rho + \mathbf{b}_{\perp}/\rho)}{\sqrt{\frac{1}{3}\rho^2 + \frac{2}{3}\rho^{-2}}} \;, \tag{1.11}$$

$$\mathbf{b}_{\parallel} \quad = \quad \frac{(\mathbf{b} \cdot \hat{\mathbf{H}})}{|\hat{\mathbf{H}}|^2}\hat{\mathbf{H}} \;, \tag{1.12}$$

$$\mathbf{b}_{\perp} \quad = \quad \frac{\hat{\mathbf{H}} \times (\mathbf{b} \times \hat{\mathbf{H}})}{|\hat{\mathbf{H}}|^2}. \tag{1.13}$$

$\rho = 1.0$ means no preferred alignment direction, while $\rho \rightarrow 0$ ($\rho \rightarrow \infty$) indicates extremely perpendicular (parallel) alignment with respect to $\hat{\mathbf{H}}$. (Previously, the alignment operation in `hammurabi` was carried out by regulating $\mathbf{b}_{\parallel}$ only [Jaffe et al., 2010], which is phenomenological equivalent to our approach presented here.) Note that ρ and $\hat{\mathbf{H}}$ can either be defined as a global constant or as a function of other physical quantities such as the regular magnetic field and the Galactic ISM structure.

For regulating the field energy density, a simple example with exponential scaling profile (which can be customized in future studies) is proposed as

$$S(\mathbf{x}) \quad = \quad \exp\left(\frac{R_{\odot} - r}{h_r}\right)\exp\left(\frac{|z_{\odot}| - |z|}{h_z}\right) \;, \tag{1.14}$$

where (r, z) is the coordinate in the Galactic cylindrical frame, and $(R_{\odot}, z_{\odot})$ represents the solar position in the Galactic cylindrical frame at which for the convenience to have unity scaling. The energy density modulation acts on the vector field amplitude through

$$\mathbf{b}(\mathbf{x}) \rightarrow \mathbf{b}(\mathbf{x})\sqrt{S(\mathbf{x})} \;. \tag{1.15}$$

The above operations of reorienting, stretching and squeezing magnetic field vectors in the spatial domain do not promise a divergence-free result. In order to clean the divergence, we transform the re-profiled field forward into the frequency domain and apply the Gram-Schmidt process

$$\tilde{\mathbf{b}} \rightarrow \sqrt{3}\left(\tilde{\mathbf{b}} - \frac{(\mathbf{k} \cdot \tilde{\mathbf{b}})\mathbf{k}}{|k|^2}\right) \;, \tag{1.16}$$

where $\tilde{\mathbf{b}}$ indicates the frequency-domain complex vector. The coefficient $\sqrt{3}$ is for preserving the spectral power statistically. The second backward Fourier transform is then carried out to provide the final random GMF vector distribution in the spatial domain.
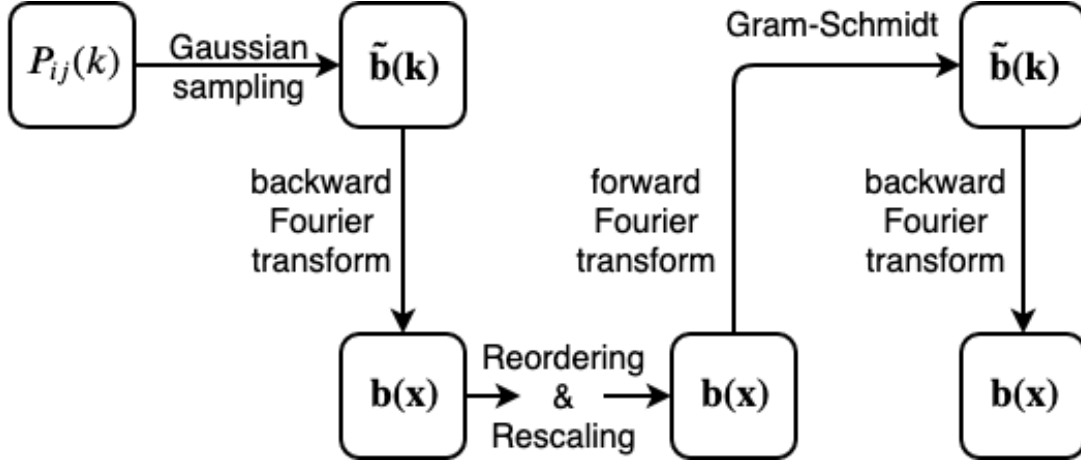
Figure 1.1: Cartoon illustration for the algorithm of the global random GMF generator.

Fig. 1.1 presents a cartoon illustration of the default algorithm proposed above. Note that separating the divergence cleaning process from spatial re-profiling comes with a cost. Strong alignment with $\rho \ll 1$ or $\rho \gg 1$ are not realizable because the Gram-Schmidt process reestablishes some extra spatial isotropy according to Eq. 1.16. Fig. 1.2 presents typical results of the global random generator in form of magnetic field probability density distributions, where we assume a Kolmogorov power spectrum. The distributions of b_y and b_z are expected to be identical with the imposed alignment direction being $\hat{\mathbf{H}} = \hat{\mathbf{x}}$. Note that the global generator is designed for realizing the inhomogeneity and anisotropy in both spatial and frequency domains, which we then have to process with divergence cleaning to provide conceptually acceptable realizations.
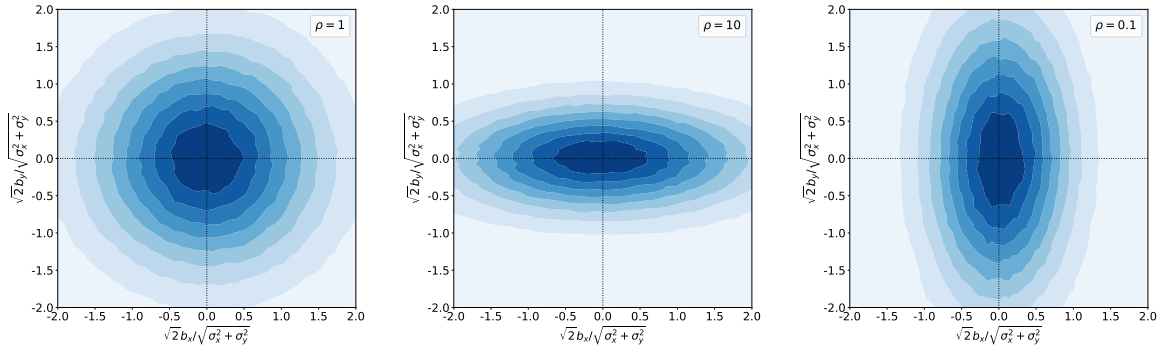
Figure 1.2: Global random GMF probability distribution. $\rho = 1.0$ provides symmetric distribution between $b_x = \mathbf{b} \cdot \hat{\mathbf{x}}$ and $b_y = \mathbf{b} \cdot \hat{\mathbf{y}}$. $\rho = 10$ indicates parallel-aligned case where b_y distribution is suppressed with respect to b_x. $\rho = 0.1$ represents perpendicular-aligned case where b_x distribution is suppressed with respect to b_y. $\sigma_{x,y}$ represents RMS of $b_{x,y}$.

1.2.4 Alternative Global Algorithm

Considering the application of the global generator in simulating Galactic synchrotron emission, the spectral anisotropy can be equally important as the spatial field orientation alignment, as we will demon-

strate in the next chapter that synchrotron B/E ratio is closely related to both features. In the default global generator proposed above, a slight tension between divergence-cleaning and the spatial alignment is technically caused by the Gram-Schmidt process. To improve, we propose an alternative algorithm for generating global Gaussian random GMF with magnetic potential field $\mathbf{A}(\mathbf{x})$. Assuming a random magnetic field $\mathbf{b}(\mathbf{x})$ is defined by its potential $\mathbf{A}(\mathbf{x})$, then in the frequency domain we have

$$\tilde{\mathbf{b}}(\mathbf{k}) \quad = \quad 2\pi i \mathbf{k} \times \tilde{\mathbf{A}}(\mathbf{k}), \tag{1.17}$$

which ensures $\nabla \times \mathbf{b}(\mathbf{x}) = 0$ and so provides an alternative approach towards divergence cleaning without using the Gram-Schmidt process.
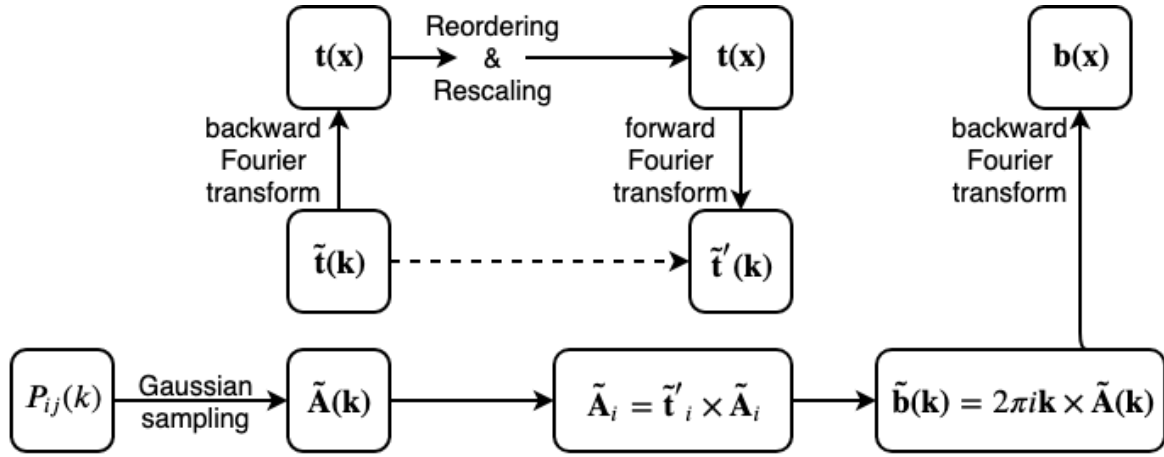

Figure 1.3: Cartoon illustration for the alternative algorithm of the global random GMF generator.

The basic design of this algorithm is illustrated in Fig. 1.3, where the core logic is mapping global profile of spatial domain into spectral domain. Differs from the default algorithm, we start with the sampling of a template magnetic potential $\tilde{\mathbf{t}} = (1.0, 1.0, 1.0)$ in a Cartesian frame, which is modified by spatial profiles and transformed back to the frequency domain. The reason for using a template potential field $\tilde{\mathbf{t}}$ is for fetching the rescaling and re-ordering operation before pushing a non-divergence-free $\tilde{\mathbf{b}}$ realization into the spatial domain. By checking the change from $\tilde{\mathbf{t}}$ to $\tilde{\mathbf{t}}'$ we know how much a homogeneous vector potential realization $\tilde{\mathbf{A}}$ should be modified.

Naively in the spatial domain, we may consider an alignment operation similar to that in the default algorithm

$$\mathbf{t}(\mathbf{x}) \quad \rightarrow \quad \frac{(\mathbf{t}_{\parallel}\rho + \mathbf{t}_{\perp}/\rho)}{\sqrt{\frac{1}{3}\rho^2 + \frac{2}{3}\rho^{-2}}} \,, \tag{1.18}$$

$$\mathbf{t}_{\parallel} \quad = \quad \frac{(\mathbf{t} \cdot \hat{\mathbf{H}})}{|\hat{\mathbf{H}}|^2}\hat{\mathbf{H}} \,, \tag{1.19}$$

$$\mathbf{t}_{\perp} \quad = \quad \frac{\hat{\mathbf{H}} \times (\mathbf{t} \times \hat{\mathbf{H}})}{|\hat{\mathbf{H}}|^2}, \tag{1.20}$$

while for the modulation, we can safely keep the default form

$$\mathbf{t}(\mathbf{x}) \rightarrow \mathbf{t}(\mathbf{x})\sqrt{S(\mathbf{x})} \,, \tag{1.21}$$

but notice that the modulation is now acting on the magnetic field potential instead of the magnetic field itself. By transforming the manipulated template field $\mathbf{t}(\mathbf{x})$ back to the frequency domain, we can copy the change in $\tilde{\mathbf{t}}$ to a realization of the true magnetic potential $\tilde{\mathbf{A}}$. Finally, divergence-free is secured by $\mathbf{k} \times \tilde{\mathbf{A}}$ which is compatible with the desired spatial and spectral profiles. Knowing that in the spatial domain random field vector reads $\mathbf{b}(\mathbf{x}) = \nabla \times \mathbf{A}(\mathbf{x})$, stretching $\mathbf{t}_\parallel$ results in perpendicular alignment in $\mathbf{b}$, while the parallel alignment is not realizable with Eq. 1.18. We notice that an ideal alignment operation should involve manipulating the helicity of the magnetic field potential $\mathbf{A}$ in the spatial domain, instead of stretching or squeezing its amplitude. This alternative algorithm is not complete yet, and the reason of introducing it here is to later verify the correctness of the Gram-Schmidt process in the default global algorithm in Chap. 2.

1.2.5 Local Generator

The local generator is proposed for realizing random GMFs in small scale regions like the solar neighbourhood or part of it according to more exquisite modellings like the Local Bubble motivated structure proposed in Alves et al. [2018], where the regular field can be approximated as homogeneous with a uniform direction, or more precisely speaking, where the random magnetic field 2-point correlation tensor can be approximated to be independent of the spatial position. With this assumption, random fields can be realized with a single fast Fourier transform. Here we describe the vector decomposition method for realizing a Gaussian random magnetic field with a generic anisotropic power spectrum tensor $P_{ij}(\mathbf{k}, \alpha)$, where α represents extra parameters in addition to the wave-vector. By assuming Gaussianity the power spectrum tensor reads

$$P_{ij}(\mathbf{k}, \alpha)\delta^3(\mathbf{k} - \mathbf{k}') \quad = \quad \langle \tilde{b}_i(\mathbf{k})\tilde{b}_j^*(\mathbf{k}') \rangle_{\tilde{\mathbf{b}}} \ , \tag{1.22}$$

where $\tilde{\mathbf{b}}$ represents the complex magnetic field vectors in the frequency domain. Depending on the specific form of the given power spectrum tensor, the vector field decomposition can be either explicit or implicit as illustrated in Fig. 1.4.
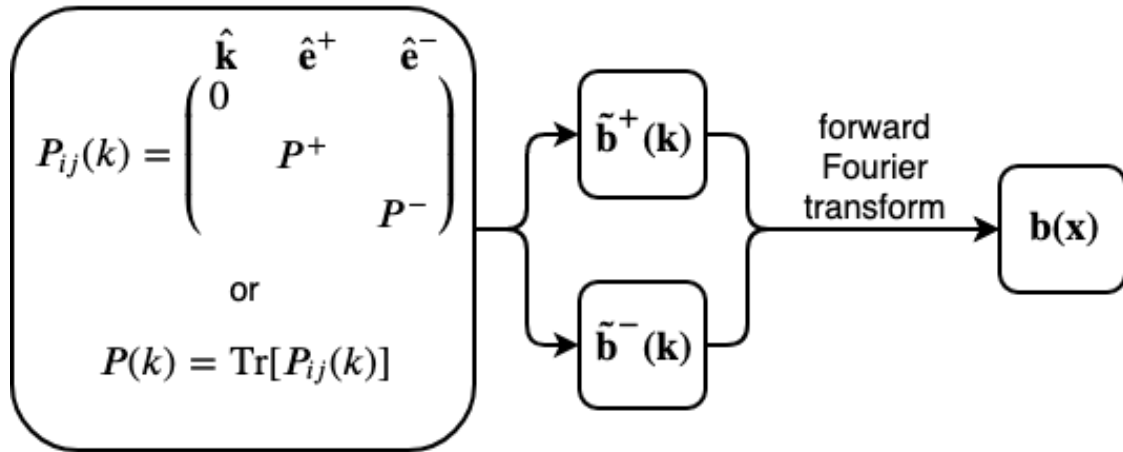

Figure 1.4: Cartoon illustration for the algorithm of the local random GMF generator.

The implicit vector decomposition sets up two modes (vector bases) for a complex Fourier vector $\tilde{\mathbf{b}}$, which means

$$\tilde{\mathbf{b}}^{\pm}(\mathbf{k}) = \tilde{b}^{\pm}(\mathbf{k})\hat{\mathbf{e}}^{\pm} \, , \tag{1.23}$$

$$\hat{\mathbf{e}}^{\pm} = \frac{\hat{\mathbf{e}}_1 \pm i\hat{\mathbf{e}}_2}{\sqrt{2}} \, , \tag{1.24}$$

where the two orthogonal basis vectors $\hat{\mathbf{e}}^{\pm}$ bind with the complex scalar $\tilde{b}^{\pm}$ respectively. The vectors $\{\hat{\mathbf{e}}_1, \hat{\mathbf{e}}_2, \hat{\mathbf{e}}_3\}$ form a Cartesian frame, and to ensure the divergence-free property of the resulting fields we choose $\hat{\mathbf{e}}_3 = \hat{\mathbf{k}}$. During the Fourier transform of $\tilde{\mathbf{b}}(\mathbf{k})$ into the spatial domain we have to consider a orthogonal base aligned with the Cartesian grid of $\mathbf{b}(\mathbf{x})$, and here we adopt one convenient base representation as

$$\hat{\mathbf{k}} = (\frac{k_x}{k}, \frac{k_y}{k}, \frac{k_z}{k}) \, , \tag{1.25}$$

$$\hat{\mathbf{e}}^{-} = (\frac{-k_y}{\sqrt{k_x^2 + k_y^2}}, \frac{k_x}{\sqrt{k_x^2 + k_y^2}}, 0) \, , \tag{1.26}$$

$$\hat{\mathbf{e}}^{+} = (\frac{k_x k_z}{k\sqrt{k_x^2 + k_y^2}}, \frac{k_y k_z}{k\sqrt{k_x^2 + k_y^2}}, \frac{-(k_x^2 + k_y^2)}{k}) \, , \tag{1.27}$$

where $k = \sqrt{k_x^2 + k_y^2 + k_z^2}$. Then we can proceed by projecting the complex field amplitude into this spatial frame

$$\tilde{\mathbf{b}} \cdot \hat{\mathbf{x}} = \tilde{b}^{+}(\hat{\mathbf{e}}^{+} \cdot \hat{\mathbf{x}}) + \tilde{b}^{-}(\hat{\mathbf{e}}^{-} \cdot \hat{\mathbf{x}}) \, , \tag{1.28}$$

where $\hat{\mathbf{x}}$ represents the spatial Cartesian coordinate. Implicit decomposition is irrelevant to the choice of the $\{\mathbf{e}^{+}, \mathbf{e}^{-}\}$ base and useful in the case where only the spectrum trace $\text{Tr}[P_{ij}(\mathbf{k})]$ is given. The amplitude of $\tilde{b}^{\pm}$ can be inferred from

$$\langle \tilde{b}^{+}, \tilde{b}^{+*} \rangle_{\tilde{\mathbf{b}}} + \langle \tilde{b}^{-}, \tilde{b}^{-*} \rangle_{\tilde{\mathbf{b}}} = \text{Tr}[P_{ij}(\mathbf{k})]d^3k \, , \tag{1.29}$$

with d^3k represents the frequency domain discretization resolution. Eq. 1.29 indicates that the field amplitudes $\tilde{b}^{\pm}$ should have a joint power spectrum equal to the trace of the total power spectrum.

The explicit decomposition should be used when the power spectrum tensor is available along with the explicitly defined base $\{\mathbf{e}^{+}, \mathbf{e}^{-}\}$, where

$$\langle \tilde{b}^{\pm}, \tilde{b}^{\pm*} \rangle_{\tilde{\mathbf{b}}} = P^{\pm}(\mathbf{k})d^3k \, . \tag{1.30}$$

A practical example is realizing Alfvén, fast and slow modes of a MHD turbulent magnetic field in a compressible plasma. Given a local regular GMF field $\mathbf{B}_0$, an Alfvén wave propagates along $\hat{\mathbf{B}}_0$ with magnetic turbulence in direction $\mathbf{e}^{+} = \hat{\mathbf{k}} \times \hat{\mathbf{B}}_0$ while slow and fast waves generate magnetic turbulence in direction $\mathbf{e}^{-} = \mathbf{e}^{+} \times \hat{\mathbf{k}}$. Note that when the wave-vector $\mathbf{k}$ is aligned with $\mathbf{B}_0$, the amplitudes of the Alfvén and slow modes vanish and the fast mode realization requires an implicit decomposition as the base $\{\mathbf{e}^{+}, \mathbf{e}^{-}\}$ is undefined.

Fig. 1.5 presents typical examples of the distribution of the random GMF from the local generator. In comparison to the magnetic field distribution from the global generator where the spatial anisotropy
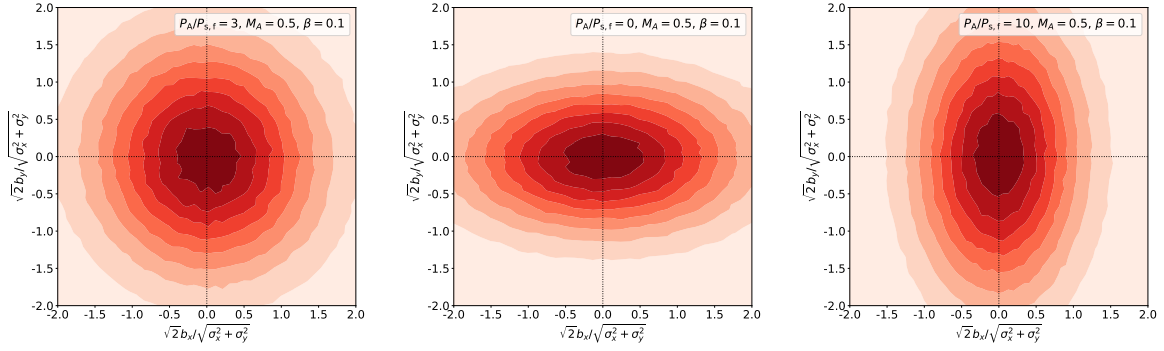
Figure 1.5: Local random field probability distribution with $\hat{\mathbf{B}}_0 = \hat{\mathbf{x}}$, Mach number $M_A = 0.5$, plasma parameter $\beta = 0.1$. P_A represents Alfvén mode power at the injection scale, while for fast and slow modes we set equal power $P_f = P_s$ at the injection scale. $\sigma_{x,y}$ represents RMS of $b_{x,y}$.

is defined by the orientation alignment, the local generator is capable of realizing more subtle field properties, e.g., the spectral anisotropic MHD wave types described earlier in this chapter. At the phenomenological level, the global generator can mimic the random magnetic field orientation alignment of the local realizations as illustrated by Fig. 1.2 and Fig. 1.5, but the spectral anisotropy is uniquely realizable by the local generator.

1.2.6   Remarks

In the random GMF generators described above, we are not using three independent FFTs for 3D vector fields. A straightforward approach to vector field FFT would be carrying out three independent transformation separately. However that is expensive in general where the operations are only limited to transforms between real and complex values. A special speedup design that provides computational efficiency is to compress the three real scalar fields into two complex scalar fields.

Suppose that in the ξ-domain we have two complex scalar fields $c_0(\xi)$ and $c_1(\xi)$, which are compressed from three real scalar fields $b_x(\xi)$, $b_y(\xi)$ and $b_z(\xi)$ by defining

$$c_0(\xi) = b_x(\xi) + ib_y(\xi), \tag{1.31}$$

$$c_1(\xi) = b_y(\xi) + ib_z(\xi), \tag{1.32}$$

Then mathematically, we know their reciprocal-domain counterparts should be

$$\tilde{c}_0(\eta) = \tilde{b}_x(\eta) + i\tilde{b}_y(\eta), \tag{1.33}$$

$$\tilde{c}_1(\eta) = \tilde{b}_y(\eta) + i\tilde{b}_z(\eta). \tag{1.34}$$

Since the transform is done between real and complex fields, complex conjugate symmetry gives a useful property

$$\tilde{c}_0^*(-\eta) = \tilde{b}_x(\eta) - i\tilde{b}_y(\eta), \tag{1.35}$$

$$\tilde{c}_1^*(-\eta) = \tilde{b}_y(\eta) - i\tilde{b}_z(\eta), \tag{1.36}$$

from which we can recover vector fields $\tilde{b}_x(\eta)$, $\tilde{b}_y(\eta)$ and $\tilde{b}_z(\eta)$ in the reciprocal-domain. This method is applied in both the global and local turbulent GMF generators in order to reduce the computational cost.

In the FFTs of both the global and local generators, the numeric field $\mathbf{b}(\mathbf{x})$ is calculated according to its frequency domain counterpart as

$$\mathbf{b}(\mathbf{x}) = \sum_{k_x}\sum_{k_y}\sum_{k_z} \tilde{\mathbf{b}}(\mathbf{k})\exp\{2\pi i\mathbf{k}\mathbf{x}\} \ . \tag{1.37}$$

Dimensional analysis requires the variance of $\tilde{\mathbf{b}}(\mathbf{k})$ in form

$$\langle \tilde{\mathbf{b}}_i(\mathbf{k})\tilde{\mathbf{b}}_j^*(\mathbf{k})\rangle_{\tilde{\mathbf{b}}} = d^3k P_{ij}(\mathbf{k},\theta) \ , \tag{1.38}$$

which in turn satisfies the definition of energy density

$$E(\mathbf{x}) = \frac{\langle \mathbf{b}^2(\mathbf{x})\rangle_{\mathbf{b}}}{8\pi} = \int_0^{k_{\max}} dk \frac{k^2}{2}\mathrm{Tr}[P_{ij}(k)] \ , \tag{1.39}$$

where $k_{\max}$ represents the Nyquist frequency. The precision of the power spectrum as represented on the spatial grid can be visualized by comparing the theoretical and numerical energy densities from field realizations. As illustrated with examples in Fig. 1.6, the convergence towards higher grid resolution demonstrates the correctness of the numeric implementations.
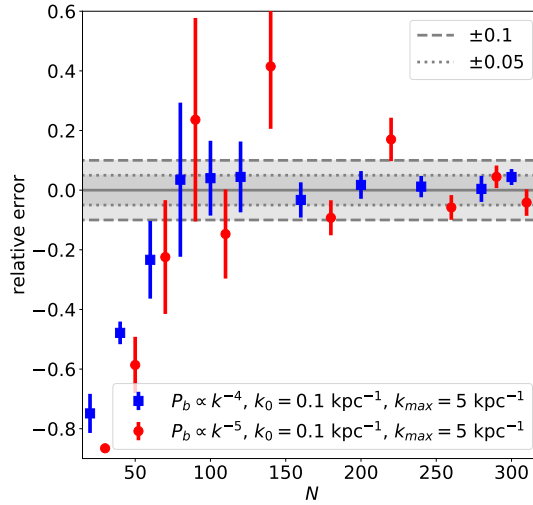
Figure 1.6: Examples of the relative difference between the theoretical and numerical energy densities in random GMF realizations. The numerical energy density of each parameter set is evaluated from an ensemble of field samples. A higher precision is achieved with better spatial resolution represented by N (with the simulation box size $L = N/2k_{\max}$), the number of sample points in each grid dimension.

1.3 Summary

In this chapter we have focused on numerically fast realizations of turbulent Galactic magnetic field with Gaussian randomness. Since the properties of turbulent GMF are defined in both the spatial

and frequency domains, it is not trivial to satisfy all features along with the divergence-free premise. To overcome such an obstacle and preserve important GMF properties, we proposed global and local random GMF generators. The global generator is capable of handling inhomogeneous spatial profiling, while the local one is designed for realizing detailed local GMF description without inhomogeneous manipulation in the spatial domain.

For ensuring the divergence-free property, the global generator adopts the triple fast Fourier transform in order to firstly realize Gaussian random samples in the frequency domain, and then we impose the inhomogeneous spatial profile in the spatial domain. A forward transfer back to the frequency domain is designed to clean the divergence with Gram-Schmidt method. The final result can be finally retrieved by a backward Fourier transform. This default approach has some difficulties in realizing extreme random field alignment, for example, in practice the spatial alignment with $\rho = 10$ differs little from the case with $\rho = 3$ as we would expect. The reason lies in the fact that the Gram-Schmidt method not only clean the divergence but also distort the spatial distribution especially when the alignment is strong. To relieve this problem, we proposed an alternative algorithm for the global generator which takes the same level of complexity in FFT but start with the magnetic vector potential instead of the magnetic field itself in the default algorithm. We emphasize that the alternative algorithm is still under development, since we notice that the spatial alignment feature should be described through the helicity in the magnetic potential, and the performance should be tested in more realistic cases.

The local algorithm, meanwhile, is simpler in theory since we use the standard vector field decomposition method. The technical detail which deserves an extra attention is the definition of explicit and implicit decomposition. At each position in the frequency domain there exists a uniquely defined wave-vector, while the perpendicular direction of this wave-vector can be arbitrarily defined in a plane. Such freedom in choosing the orthogonal basis gives the idea of implicit decomposition. In some cases like the MHD turbulent modes, the magnetic turbulent is defined according to both the wave-vector and the regular magnetic field orientation, and so the perpendicular direction is fixed which is thus understood as the explicit decomposition.

Beyond the new realization methods, we also have implemented efficient Fourier transform procedure with multi-threading support. The realization precision has been examined and ensured. In the next chapter, we will analyse the influence of global and local random GMF realizations on the Galactic synchrotron emission.

Chapter 2

Simulating Galactic Synchrotron Emission

2.1 Overview

Synchrotron emission from the diffuse population of relativistic electrons and positrons in the magnetized interstellar medium (ISM) is the dominant signal in the polarized sky observed at frequencies ranging from MHz to GHz. Galactic synchrotron emission is therefore one of the best friends to scientists who study multi-phase ISM structure and cosmic ray (CR) transport properties. To those who study the cosmic microwave background radiation (CMBR), 21cm cosmology and the early Universe, however, it is one of their worst enemies. Both fields recognize the importance of physical modelling of the mechanisms and environments associated with polarized synchrotron emission, absorption and Faraday rotation, which in the end provide a realistic description of the foreground observables. The fundamental physical principles of the radiative transfer processes have been fully understood for around half a century [Rybicki and Lightman, 1979], however with the growing precision and range of observations, we are challenged by various local structures and non-linear phenomena within the Galaxy. This is slowing down conceptual and theoretical advancements in related research fields since the observables are no longer analytically calculable in a high-resolution and non-perturbative regime. To overcome this, hammurabi [Waelkens et al., 2009] was developed to help us simulate complicated observables with 3D modelling of the physical components of the Galaxy.

For almost a decade we have witnessed a wide scientific applications of hammurabi for example, in estimating and removing Galactic synchrotron foreground contamination [Dolag et al., 2015, Switzer and Liu, 2014], in understanding magnetic fields of astrophysical objects varying from supernova remnants [West et al., 2017] to the Galaxy [Jaffe et al., 2013, Adam et al., 2016] and even to the local Universe [Hutschenreuter et al., 2018]. Despite successful applications of hammurabi, we have noticed that after years of modifications and the accumulation of modules and functions with outdated programming standards, the package might be compromised by numeric issues and the lack of a properly maintained testing suite. Given the trend towards high-resolution and computation-dominated studies, it is the right time

to provide a precision guaranteed high-performance pipeline for simulating polarized synchrotron emission, absorption and Faraday rotation. Thus a thorough upgrading project has been performed, where we mainly focus on redesigning the code structure and work-flow, calibrating the numeric algorithms and methods, improving the user experience and setting up new conventions for future maintenance and development.

In addition to the technical improvements, we also keep up with recent progress in physical modelling of Galactic foreground emission with the turbulent Galactic magnetic field (GMF), e.g. phenomenological research carried out by Beck et al. [2016], analytic estimations calculated by Cho and Lazarian [2002], Caldwell et al. [2016], Kandel et al. [2017, 2018], and heavy simulations analyzed by Akahori et al. [2013], Kritsuk et al. [2018], Brandenburg et al. [2019]. For future work about inferring the GMF configuration from observational data (e.g., Galactic synchrotron and dust emission, dispersion measure and Faraday rotation measure) we need physically motivated and numerically fast magnetic field simulators, instead of setting up trivial random fields or directly adopting expensive magneto-hydrodynamics (MHD) simulators. The balance has to be made between the computational cost and the modelling complexity. Low computational costs are required by any analysis that infers model parameters directly from data in a Bayesian fashion. There, the model has to be evaluated repeatedly while the inference algorithm samples through the often very high dimensional parameter space. Full MHD simulations are currently prohibitively expensive to be used within such algorithms. Thus, fast emulators for the main statistical properties of typical MHD simulations are needed instead.

In the previous chapter, we have proposed two fast (in contrast to MHD simulation) random GMF generators which satisfy certain criteria. A project for studying the GMF configuration with numeric simulation has been proposed [Boulanger et al., 2018] using a computational inference engine. Though the main motivation for `hammurabi X` is the construction of a Bayesian magnetic field inference engine, we herein present an analysis of the angular power spectrum focusing on the synchrotron B/E ratio as a possible guide for future studies.

2.2   hammurabi X

The `hammurabi` code [Waelkens et al., 2009] is an astrophysical simulator based on 3D models of the components of the magnetised ISM such as magnetic fields, thermal electrons, relativistic electrons, and dust grains. It performs an efficient line-of-sight (LoS) integral through the simulated Galaxy model using a `HEALPix` [1]-based [Gorski et al., 2005] nested grid to produce observables such as Faraday rotation measure and diffuse synchrotron and thermal dust emission [2] in full Stokes I, Q and U, while taking into account beam and depth depolarization as well as Faraday effects.

The updated version, `hammurabi X`[3], has been developed in order to achieve higher computing performance and precision. Previously in `hammurabi`, the generation of the anisotropic component of the

---

[1] `https://healpix.jpl.nasa.gov`
[2] This report focuses on the Galactic synchrotron emission, while the technical report and corresponding scientific analysis of simulated thermal dust emission with `hammurabi X` is under preparation.
[3] `hammurabi X` is available in its public repository, `https://bitbucket.org/hammurabicode/hamx`, with detailed documentation.

random field as well as the modulation of the field strength following various parametric forms lead to artificial magnetic field divergence. Now we propose two improved solutions for simulating the random magnetic field. On Galactic scales, a triple Fourier transform scheme is proposed to restore the divergence-free condition via a cleaning process. The new generation process is different from that used in Adam et al. [2016] by imposing the divergence-free property in the random magnetic field, which was discussed in detail in § 1.2.3 with its observational implication to be discovered in this chapter. Alternatively, in a given local region [4], a vector-field decomposition scheme is capable of simulating more detailed random field power-spectra. Recently, `hammurabi X` has already been used to generate extra-galactic Faraday rotation maps from primordial magnetic fields in Hutschenreuter et al. [2018].

2.2.1   Software Design

`hammurabi X` logically consists of three major building blocks, i.e., grid, field and LoS integrator as presented in Fig. 2.1. There is one grid base class, and derived from which there are many derived classes which define the Cartesian grids for Galactic components and `HEALPix` shells for carrying out the LoS integral. The field classes are in charge of all built-in physical modellings, including the random field generators. Numerical descriptions of Galactic fields are handled by the grid modules directly, but requires specifically defined input or output formats. The grid and field modules are connected by interfacing functions which can either write analytic field descriptions into the memory hosted by the corresponding grids, or retrieve numerical information of certain fields from the grid storage. The LoS integrator collects numerical descriptions for all fields and calculate observables in `HEALPix` shells. In the following we briefly discuss some important features which are helpful for users to understand how `hammurabi X` works.

Pipeline

The pipeline class is defined for modularizing the main routines into several task groups as shown by black boxes in Fig. 2.1. The functions in pipeline class are named as assemblers which in deed collect information from the parameter set (except the observable assembler) and initialize what we need for calculating the observables. The grid and field assemblers call the grid and field classes respectively, where it is up to the user whether a specified field will be imported from external files or known analytic models. The external field information goes through the orange lines while the built-in models follow the green path as displayed in Fig. 2.1. Although the integration grid is derived from the base grid class but it is intrinsically different from other grid classes since it hosts the information for storing and preparing the observables. The LoS integrator follows the settings carried by the integration grid and retrieve field distributions either from analytic models directly or by interpolating the field grids. It is worth noticing that the LoS integration process may not be executed only once in a simulation pipeline. In case multi-frequency emission results are required, the LoS integrator can repeat the calculation loop without changing or re-initializing field distributions.

---

[4]The local region means any small-scale spatial domain where the magnetic mean field can be treated or approximated as uniform distribution, which indicates that the local generator cannot be applied to realize large-scale random magnetic field which is typically handled by the global generator. In this chapter we will present and analyze local realizations at the solar neighborhood as an example.
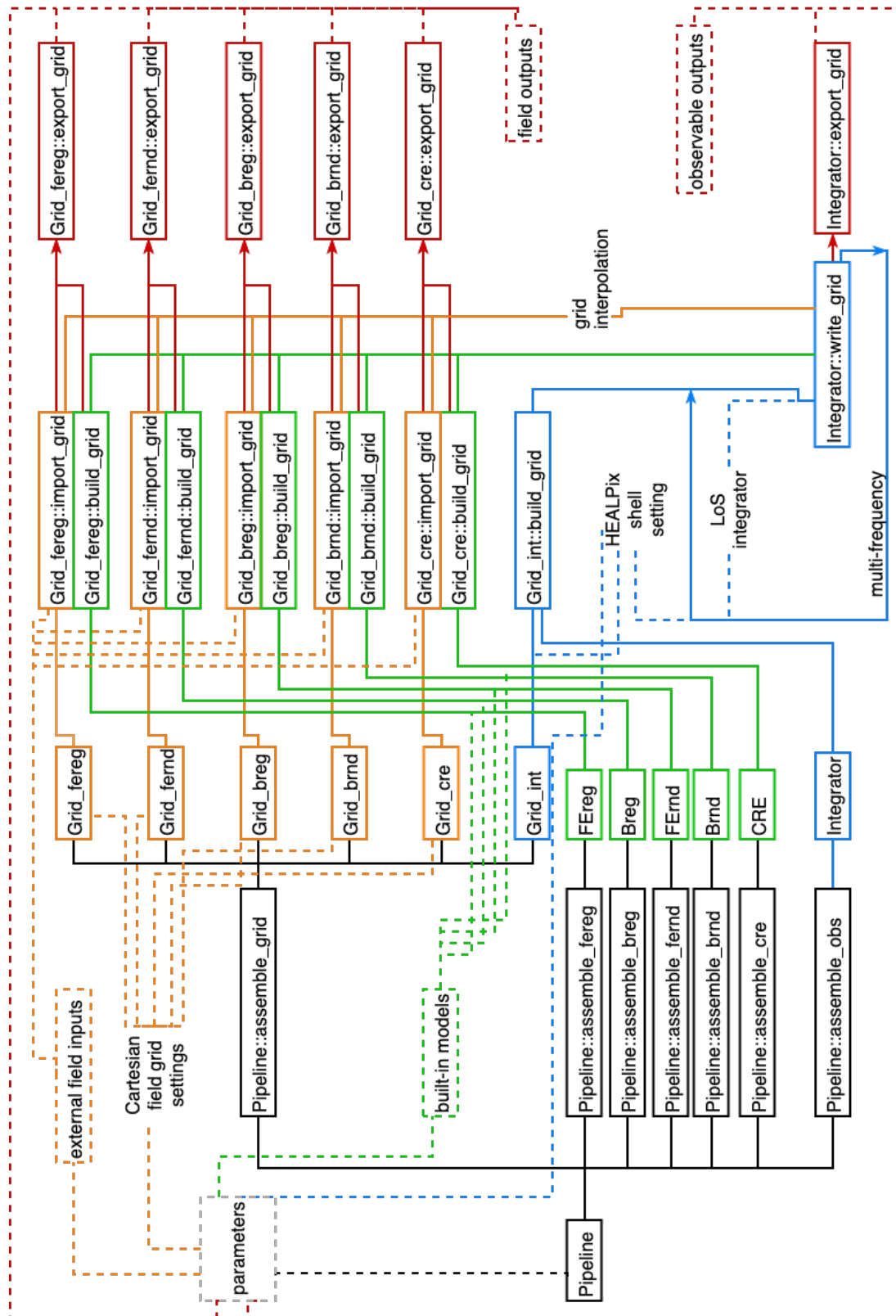
Figure 2.1: `hammurabi X` workflow.

LoS Integration

hammurabi X currently uses the HEALPix library [Gorski et al., 2005] for observable production, where the LoS integral accumulates through several layers of spherical shells with adaptable HEALPix resolutions. We provide two modes of integral shell arrangements. In the auto-shell mode, given R as the maximum simulation radius, the nth shell out of N total shells covers the radial distance from $2^{(n-N-1)}R$ to $2^{(n-N)}R$, except for the first shell which starts at the observer. The nth shell is by default set up with the HEALPix resolution controlling parameter $N_{\text{side}} = 2^{(n-1)}N_{\text{min}}$ [5], where N_{min} represents the lowest simulation resolution at the first shell. Alternatively in the manual-shell mode, shells are defined explicitly by a series of dividing radii and HEALPix N_{side}'s. The radial resolution along the LoS integral is uniformly set by the minimal radial distance for each shell. The auto-shell mode follows the idea that the integral domain is discretized with elemental bins of the same volume, while the manual-shell mode allows users to refine specific regions in order to meet special realization requirements.

The LoS integral is carried out hierarchically, at the top level the integral is divided into multiple shells with given spherical resolution settings, while at the bottom level inside each shell (where the spherical resolution is fixed) the radial integral is carried out with the midpoint rule for each pixel-radial bin. Accumulation of observable information from the inner to outer shells is applied at the top level. We emphasize that in hammurabi X, the simulation spherical resolution for each shell can be independent of that in the outputs, which means that we can simulate with an arbitrary number of shells and assign each shell with a unique N_{side} value. While in the shell accumulating process, we interpolate (with linear interpolation provided by HEALPix library) the recently accomplished bottom level inside-shell integral result into the output resolution. And consequently, such interpolation between different angular resolutions will inevitably create certain level of precision loss.

Fields

Physical fields are implemented as C++ classes. Currently, hammurabi X contains base classes for parameterized description of each type of fields, e.g., regular and random GMF. Specific field models are treated as derived classes with respect to corresponding base classes. This design provides convenience in maintaining and customizing field models. In case users do not have or intend to use analytic models of fields, hammurabi X is also capable of reading and writing numerical field distributions in Cartesian grids. For each type of field we provide controllers for its external in/output. The "write" switch will export physical field grid into an external binary file, while the "read" switch does the opposite operation. The grid size and resolution for each field are separately defined when a grid is required for allocating the memory either by reading/writing external field distribution or assembling a random field. Once the field distribution is allocated to its corresponding grid, the main routine is capable of interpolating it from an arbitrary position within the grid.

---

[5] N_{side} means the number of full sky pixels is $12N_{\text{side}}^2$.

Fourier Transform and Grid Interpolation

Fast Fourier transforms (FFTs) are necessary for translating the power spectra of random fields into discrete magnetic field realizations on 3D spatial grids. Random field generators in `hammurabi X` currently use the `FFTW`[6] library. The detailed implementation was discussed in the previous chapter. In cases where the field is input from an external or internal discrete grid, e.g., a random GMF, the LoS integral at a given position does linear interpolation (in each phase-space dimension) from nearby grid points. The interpolation algorithm has been calibrated, so the high resolution outputs are no longer contaminated by any artificial structure in earlier versions of `hammurabi`. As illustrated in Fig. 2.2, the interpolation process in the earlier version of `hammurabi` made mistakes in calculating the volume of elemental discretization, which results in negative values of simulated dispersion measure (as an illustrative example) and incorrect small scale features in comparison to the corrected method in `hammurabi X`. In this new version, unit tests for linear interpolation can be found in the public repository.
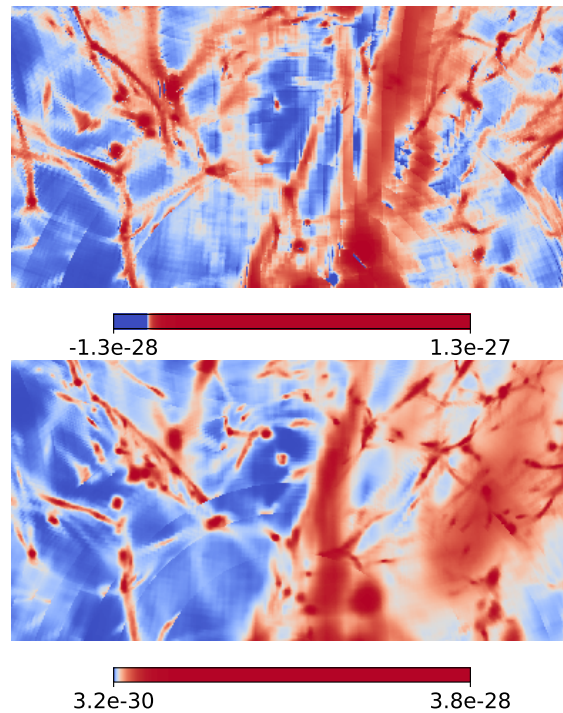
Figure 2.2: Comparison between the output from earlier version `hammurabi` (top) and `hammurabi X` (bottom). The sky patch in this illustration shows the extra-galactic dispersion measure (an observable with non-negative value by definition) simulated and studied by Hutschenreuter et al. [2018].

Generally speaking, the precision of linear interpolation (and the discretization along with it) can be in principle characterized by the goodness of approximation which is explicitly affected by the discretization resolution and arrangement of the sampling/supporting points, and also by the smoothness (second order derivative) of the approximation target. In `hammurabi X` the interpolation affects the precision in realizing the power spectrum of random magnetic field generation. This can be improved by increasing the sampling

---

[6]http://www.fftw.org

resolution. Further more, the linear interpolation does not preserve the divergence, but the precision can be improved either by increasing sampling resolution [7] or matching the elemental discretization volume in LoS integral and that in the field generation (as discussed by Waelkens et al. [2009]).

2.2.2   Underlying Theory

Here we present the basic mathematical formulae in calculating polarized synchrotron emission, absorption and Faraday rotation. The method is defined not only for analytic modelling of the CRE flux, but also for an input grid of dimension $3 + 1$ imported from external binary files, where the spectral dimension is defined by a logarithmic sampling of electron energy. This matches the output convention in CR transport simulators like Galprop [Strong and Moskalenko, 1998] and DRAGON [Evoli et al., 2017].

Radiative Transfer

With the CRE differential flux distribution $\Phi(E, \mathbf{r})$, synchrotron total and polarized emissivities at given observational frequency ν and spatial position $\mathbf{r}$ read

$$j_{\mathrm{tot/pol}}(\nu, \mathbf{r}) \;=\; \frac{1}{4\pi} \int_{E_1}^{E_2} dE \frac{4\pi}{\beta c} \Phi(E, \mathbf{r}) 2\pi P_{\mathrm{tot/pol}}(\omega) \;, \tag{2.1}$$

where $P_{\mathrm{tot/pol}}(\omega)$, which represents the emission power from one electron at frequency $\nu = \omega/2\pi$, is calculated [Rybicki and Lightman, 1979] through synchrotron functions $F(x) = x \int_x^\infty K_{\frac{5}{3}}(\xi) d\xi$ and $G(x) = x K_{\frac{2}{3}}(x)$ (with $K_{\frac{5}{3}}(x)$ and $K_{\frac{2}{3}}(x)$ known as two of the modified Bessel functions of the second kind) as

$$P_{\mathrm{tot}}(\omega) \;=\; \frac{\sqrt{3} e^3 B_{\mathrm{per}}}{2\pi m_e c^2} F(x) \;, \tag{2.2}$$

$$P_{\mathrm{pol}}(\omega) \;=\; \frac{\sqrt{3} e^3 B_{\mathrm{per}}}{2\pi m_e c^2} G(x) \;, \tag{2.3}$$

where e is the electron charge, m_e the electron mass, and B_{per} represents the strength of the magnetic field projected in the direction perpendicular to the LoS direction. Statistically, we assume the synchrotron emission at given position is isotropic, and so an observer only receives $1/4\pi$ of the emission power, which explains the $1/4\pi$ coefficient in the front of the right hand side in Eq. 2.1. In addition, we place an extra 2π before $P_{\mathrm{tot/pol}}(\omega)$ due to the relation $P(\nu) = 2\pi P(\omega)$. The term $\frac{4\pi}{\beta c}\Phi(E, \mathbf{r})$, with β representing the relativistic speed, is actually $N(E, \mathbf{r})$, the CRE differential density.

In practice, the CRE spectral integral can be achieved in two technically different (but with the same theoretical origin) approaches. If given numerical CRE flux information $\Phi(E)$ prepared on a discrete grid, the integral Eq. 2.1 can be directly evaluated by the numerical integral. Alternatively we can start with an analytic differential density distribution $N(\gamma, \mathbf{r}) = 4\pi\Phi(E, \mathbf{r})m_e c/\beta$, and by doing so the Eq. 2.1 reads

$$j_{\mathrm{tot/pol}}(\nu, \mathbf{r}) \;=\; \frac{1}{2} \int_{\gamma_1}^{\gamma_2} d\gamma N(\gamma, \mathbf{r}) P_{\mathrm{tot/pol}}(\omega) \;. \tag{2.4}$$

---

[7] If estimate the divergence by the finite difference in the spatial domain, the precision in divergence follows an exponential improvement as a function of the number of sample points in each direction.

The reason for keeping Eq. 2.4 as an alternative method is to calculate the integral analytically once the CRE spectral index is constant at any given position. The detailed derivation follows the auxiliary definition of

$$\omega_c = \frac{3}{2}\gamma^2 \frac{eB_{\mathrm{per}}}{m_e c} \ , \tag{2.5}$$

$$x = \frac{\omega}{\omega_c} \ . \tag{2.6}$$

Then by assuming $N(\gamma) = N_0 \gamma^{-\alpha}$, Eq. 2.4 ends up in the form as

$$j_{\mathrm{tot}}(\nu, \mathbf{r}) = \frac{\sqrt{3}e^3 B_{\mathrm{per}} N_0}{8\pi m_e c^2} \left(\frac{4\pi\nu m_e c}{3eB_{\mathrm{per}}}\right)^{(1-\alpha)/2} \int dx F(x) x^{(\alpha-3)/2} \ , \tag{2.7}$$

$$j_{\mathrm{pol}}(\nu, \mathbf{r}) = \frac{\sqrt{3}e^3 B_{\mathrm{per}} N_0}{8\pi m_e c^2} \left(\frac{4\pi\nu m_e c}{3eB_{\mathrm{per}}}\right)^{(1-\alpha)/2} \int dx G(x) x^{(\alpha-3)/2} \ , \tag{2.8}$$

$$\tag{2.9}$$

where the spectral integrals can be analytically calculated by using

$$\int dx F(x) x^\mu = \frac{2^{\mu+1}}{\mu+2}\Gamma(\frac{\mu}{2}+\frac{7}{3})\Gamma(\frac{\mu}{2}+\frac{2}{3}) \ , \tag{2.10}$$

$$\int dx G(x) x^\mu = 2^\mu \Gamma(\frac{\mu}{2}+\frac{4}{3})\Gamma(\frac{\mu}{2}+\frac{2}{3}) \ . \tag{2.11}$$

The left panel in Fig. 2.3 illustrates the dependence of the synchrotron total emissivity T_{tot} and polarized emissivity T_{pol} on CRE energy, with varying magnetic field strength, observational frequency and CRE spectral shape. The peaks in emissivities are inherited from $F(x)$ and $G(x)$, where the dimensionless parameter x is the ratio of observational frequency to CRE gyro-frequency.

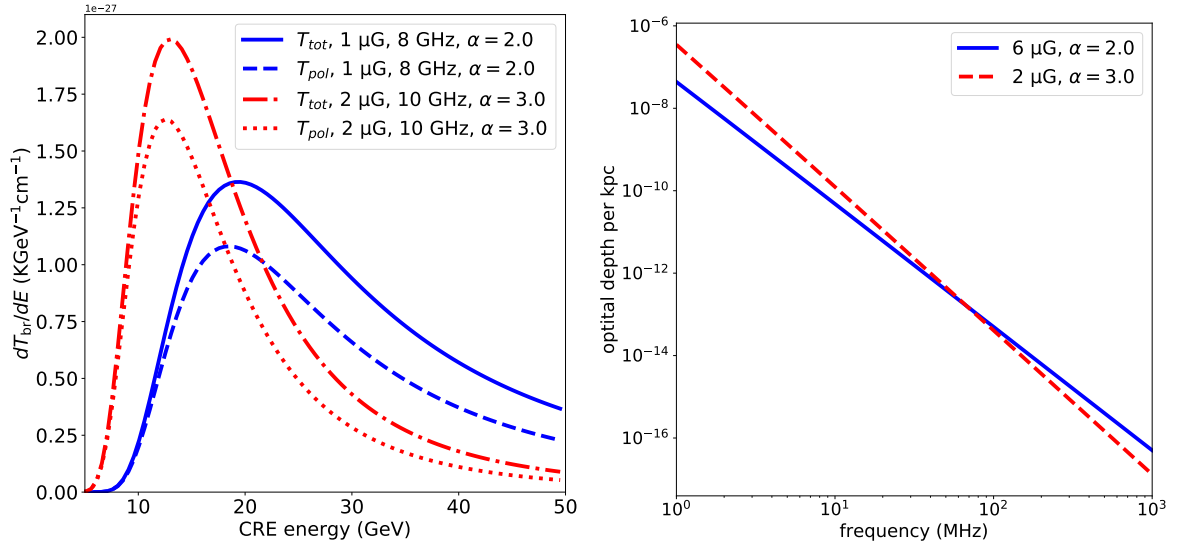Figure 2.3: Left panel: Differential synchrotron total and polarized emissivities (has been converted into brightness temperature) of CRE which follows simple power-law spectrum $\propto \gamma^{-\alpha}$. Right panel: Optical depth of synchrotron self-absorption with constant CRE spectral index α (flux intensity normalized at the solar neighbourhood). Magnetic field strength and observational frequency are given.

Strictly speaking, a complete LoS integral should consider radiative transfer

$$dI_\nu \quad = \quad j_\nu ds - I_\nu \alpha_\nu ds \ , \tag{2.12}$$

where α_ν contains all absorption effects including self-absorption and free-free absorption. In practice, the optical depth can be evaluated according to its absorption coefficient, and the accumulated attenuation factor is then imposed to polarized emission along the LoS integral. It is however not always necessary to consider the absorption effect in the Galaxy. According to previous studies [Schlickeiser, 2002] the Galactic environment is optically thin for synchrotron emission from CRE at frequency above 10 MHz, while below that the synchrotron emission is mainly attenuated by free-free absorption. Synchrotron self-absorption coefficient is defined as

$$\alpha_\nu(\mathbf{r}) \quad = \quad \frac{c^2}{8\pi\nu^2} \int dE [2\pi P(\omega)] E^2 \frac{\partial}{\partial E} \left[\frac{N(E,\mathbf{r})}{E^2} \right] \ , \tag{2.13}$$

where differential density $N(E,\mathbf{r}) = 4\pi\Phi(E,\mathbf{r})/\beta c$. According to the simple illustration presented by the right panel in Fig. 2.3 we can safely ignore the self-absorption effect for synchrotron emission at and beyond MHz level in the Galaxy. The latest release of hammurabi X does not contain absorption module as long as we focus on simulating the Galactic synchrotron emission at GHz level.

Faraday Rotation

Faraday rotation describes the phenomenological manifestation of the refractive index difference in the polarization directions for photons that propagate through a plasma with an external magnetic field. For a linearly polarized photon emitted with wavelength λ and intrinsic polarization angle χ_0, the observed polarization angle after traversing distance s_0 is

$$\chi \quad = \quad \chi_0 + \phi(s_0)\lambda^2 \ , \tag{2.14}$$

where ϕ, the Faraday depth reads

$$\phi(s_0) \quad = \quad \frac{e^3}{2\pi m_e^2 c^4} \int_0^{s_0} ds N_e(s\hat{\mathbf{p}})\mathbf{B}(s\hat{\mathbf{p}}) \cdot \hat{\mathbf{p}} \ , \tag{2.15}$$

where $\hat{\mathbf{p}}$ represents photon propagation direction, N_e represents distribution of thermal electron density. Note that the IAU convention[8] for polarization is adopted in hammurabi X, which means that the intrinsic synchrotron polarization angle is determined by the polarization ellipse semi-major axis perpendicular to magnetic field orientation. Under Faraday rotation at a given observational frequency ν, the observed emission accumulates Stokes parameter dQ and dU over a distance s_0 by

$$dQ + idU \quad = \quad dI_\nu^p \exp\{2i\chi\} \ , \tag{2.16}$$

where dI_ν^p represents polarized intensity in radial bin $[s_0, s_0 + ds]$. Though Faraday rotation brings in extra information about the thermal electron (TE) distribution, a relatively high observational frequency is sometimes preferred for studying synchrotron emission, e.g., 30 GHz in this report, in order to suppress the complicated effects of TE turbulence, which will be addressed in our future studies with hammurabi X.

---

[8]Detailed description for the different IAU and CMB polarization conventions can be found at `https://lambda.gsfc.nasa.gov/product/about/pol_convention.cfm`.

2.2.3 Precision and Performance

Precision

Profiling the numerical precision in producing observables is critical in guiding practical applications. A standard simulation procedure can be decomposed into two major processes. The first part is the numerical implementation of a specific physics phenomenon like synchrotron emission and Faraday rotation, and the second part is the LoS integral that is universal to all observables. In the following integrated precision check, the correctness of both will be verified and profiled together.

A given magnetic field vector $\mathbf{B}$ can be decomposed into directions parallel (horizontal) and perpendicular (vertical/poloidal) to the galactic disk, or to be specific, the $\{\hat{\mathbf{x}}, \hat{\mathbf{y}}\}$ plane (with $\hat{\mathbf{y}}$ pointing towards galactic longitude $l = 90°$) in the `hammurabi X` convention, i.e., $\mathbf{B}_\parallel$ and $\mathbf{B}_\perp$ at a given galactic longitude-latitude position $\{l, b\}$. The LoS direction $\hat{\mathbf{n}}$ from the observer to the target field position reads

$$\hat{\mathbf{n}} \quad = \quad \cos(b)\cos(l)\hat{\mathbf{x}} + \cos(b)\sin(l)\hat{\mathbf{y}} + \sin(b)\hat{\mathbf{z}} \ , \tag{2.17}$$

where $\hat{\mathbf{x}}$ is conventionally pointing from the observer to the Galactic centre. In the same observer-centric Cartesian frame we can explicitly write down two field components as

$$\mathbf{B}_\parallel \quad = \quad B_\parallel(\cos(l_0)\hat{\mathbf{x}} + \sin(l_0)\hat{\mathbf{y}}) \ , \tag{2.18}$$

$$\mathbf{B}_\perp \quad = \quad B_\perp \hat{\mathbf{z}} \ , \tag{2.19}$$

where l_0 represents the projected direction of $\mathbf{B}$ in the $\{\hat{\mathbf{x}}, \hat{\mathbf{y}}\}$ plane. Then it is straight forward to calculate two key quantities needed for the calculation of synchrotron emissivity and Faraday rotation respectively

$$|\mathbf{B} \times \hat{\mathbf{n}}| \quad = \quad \sqrt{B_\parallel^2 + B_\perp^2 - |\mathbf{B} \cdot \hat{\mathbf{n}}|^2} \ , \tag{2.20}$$

$$\mathbf{B} \cdot \hat{\mathbf{n}} \quad = \quad B_\parallel \cos(b)\cos(l - l_0) + B_\perp \sin(b) \ , \tag{2.21}$$

It is obvious that Faraday rotation is more sensitive to $\mathbf{B}_\parallel$ at low Galactic latitudes, and to $\mathbf{B}_\perp$ at high latitudes. On the contrary, synchrotron emissivity, which is proportional to some power of $|\mathbf{B} \times \hat{\mathbf{n}}|$, is more sensitive to $\mathbf{B}_\perp$ at low Galactic latitudes and to $\mathbf{B}_\parallel$ at high latitudes.

Precision checks require a baseline model for each field, from which analytic descriptions of the observables can be explicitly derived. Here we assume spatially homogeneous distributions for the cosmic-ray electrons (CREs), thermal electrons (TEs) and the GMF within a given radial distance to observer. The spectral index of the CRE energy distribution is assumed to be a constant, and consequently CRE density $N(\gamma)$ is described by

$$N(\gamma) \quad = \quad N_0 \gamma^{-\alpha} \ , \tag{2.22}$$

where γ represents CRE Lorentz factor, α represents the constant spectral index of CRE. With the assumed homogeneity in all fields, we can calculate intrinsic synchrotron total intensity I_0 and polarization Stokes parameter Q_0 and U_0 (in the IAU convention[9]) before applying the Faraday rotation [Rybicki and

---

[9]Detailed description for IAU and CMB polarization conventions can be found at `https://lambda.gsfc.nasa.gov/product/about/pol_convention.cfm`.

Figure 2.4: Cartoon illustration of the projection of magnetic field $\mathbf{B}$ to the LoS direction $\hat{\mathbf{n}}$. The definition of synchrotron intrinsic polarization angle (with north-to-east as the positive angle direction) is presented on the top left LoS plan, with red arrow presenting the magnetic field projected to the plane of sight.

Lightman, 1979]

$$I_0 = J_i R_0 \; , \tag{2.23}$$

$$Q_0 = J_{\mathrm{pi}} R_0 \cos(2\chi_0) \; , \tag{2.24}$$

$$U_0 = J_{\mathrm{pi}} R_0 \sin(2\chi_0) \; , \tag{2.25}$$

$$J_i = \frac{\sqrt{3}e^3 |\mathbf{B} \times \hat{\mathbf{n}}| N_0}{4\pi m_e c^2 (\alpha + 1)} \left(\frac{2\pi\nu m_e c}{3e|\mathbf{B} \times \hat{\mathbf{n}}|}\right)^{\frac{1-\alpha}{2}} \tag{2.26}$$

$$\times \Gamma(\frac{\alpha}{4} + \frac{19}{12})\Gamma(\frac{\alpha}{4} - \frac{1}{12}) \; ,$$

$$J_{pi} = \frac{\sqrt{3}e^3 |\mathbf{B} \times \hat{\mathbf{n}}| N_0}{16\pi m_e c^2} \left(\frac{2\pi\nu m_e c}{3e|\mathbf{B} \times \hat{\mathbf{n}}|}\right)^{\frac{1-\alpha}{2}} \tag{2.27}$$

$$\times \Gamma(\frac{\alpha}{4} + \frac{7}{12})\Gamma(\frac{\alpha}{4} - \frac{1}{12}) \; ,$$

where e is the electron charge, and m_e is the electron mass, R_0 is the spherical LoS integral depth, and ν is the observational frequency. The intrinsic polarization angle χ_0 can be derived from

$$\tan(\chi_0) = \frac{B_\perp \cos(b) - B_\parallel \sin(b) \cos(l - l_0)}{B_\parallel \sin(l - l_0)} \; , \tag{2.28}$$

as illustrated in Fig. 2.4. With the same modelling, Faraday depth ϕ can be described by

$$\phi(l, b) = \phi_0 R_0 \; , \tag{2.29}$$

$$\phi_0 = -N_e (\mathbf{B} \cdot \hat{\mathbf{n}}) \left(\frac{e^3}{2\pi m_e^2 c^4}\right) \; , \tag{2.30}$$

where N_e represents constant homogeneous TE density assumed within spherical radius R_0. In the end, the observed synchrotron polarization Stokes parameters Q and U reflect the Faraday rotation as

$$Q + iU = (Q_0 + iU_0) \int_0^{R_0} \frac{e^{2i\phi_0 \lambda^2 r}}{R_0} dr \; , \tag{2.31}$$
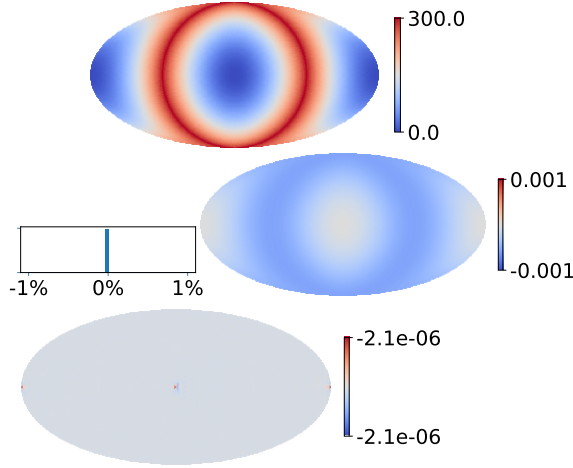
Figure 2.5: Synchrotron Stokes I (top) at 2.4 GHz. Absolute error (middle) and relative error (bottom) are presented according to the analytic reference with $B_\perp = 0$ and $l_0 = 0$. The histogram (middle left) presents relative error distribution. The single shell LoS integral is carried out with radial resolution set as 1% of the total radius.

which also indicates that the polarized intensity receive a correction factor $|\sin(\phi\lambda^2)/(\phi\lambda^2)|$ consequently which is also known as the Faraday depolarization. The formulae above are derived for providing analytically calculable results as the references in verifying the numerical outputs, while in real application the magnetic field and CRE spectral index are not constant, the methods used by `hammurabi X` for calculating synchrotron emissivity and Faraday rotation can be more generic as presented above.

Fig. 2.5 presents the absolute and relative numeric error distribution of synchrotron total intensity from a single LoS integral shell. For an observable X, the absolute error is defined as the difference between simulated output X_{sim} and the analytic reference X_{ref} as $(X_{\mathrm{sim}} - X_{\mathrm{ref}})$, while the relative error is defined by $2(X_{\mathrm{sim}} - X_{\mathrm{ref}})/(X_{\mathrm{sim}} + X_{\mathrm{ref}})$. The Faraday depth calculator shares a similar error distribution as the calculator of synchrotron total intensity. Meanwhile, Fig. 2.6 presents the absolute and relative numeric error distributions of synchrotron Stokes Q also from a single LoS integral shell, which serves as an example for illustrating the numeric precision in calculating tensor fields. With constant models in testing, the numeric errors are mainly induced by the integration and interpolation methods and therefore independent of the LoS resolution. Even with simple field settings, we can observe a few percent relative error appearing in Fig. 2.6. Considering the future usage of `hammurabi X` in inferring Galactic component structures with astrophysical measurements, if the magnitude of such numerical errors are larger than the observational uncertainties, a Bayesian analysis with `hammurabi X` will consequently suffer from higher uncertainties in parameter estimation but not biased, because the distribution of relative numerical errors is quite symmetric with respect to zero as illustrated in Fig. 2.6.

In terms of the multi-shell arrangement in real application, the output precision is affected by the spherical surface interpolation provided by the `HEALPix` library. The motivation of allowing different resolution settings along with the divided LoS integral shells is to save computing resources as mentioned in Adam et al. [2016]. It is worth noticing that in the simulation, the pixel values are calculated along
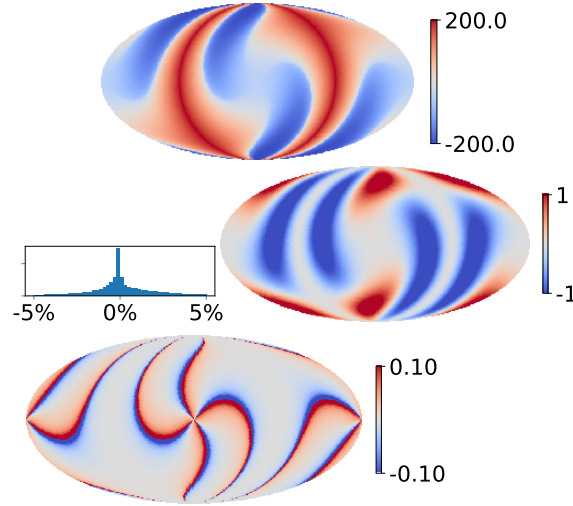
Figure 2.6: Synchrotron Stokes Q (top) at 2.4 GHz where the influence of Faraday rotation is clearly imprinted. Absolute error (middle) and relative error (bottom) are presented according to the analytic reference with $B_\perp = 0$ and $l_0 = 0$. The histogram (middle left) presents relative error distribution. The single shell LoS integral is carried out with radial resolution set as 1% of the total radius.

their central spherical coordinates. This is different from the actual astrophysical measurements where each pixel value is estimated based on many observational hits. And thus when comparing low resolution simulation results with high resolution data, we recommend interpolating data with respect to the simulation LoS directions instead of downgrading data by averaging over high resolution pixels [10].

The testing cases displayed above are prepared by assuming constant magnetic field and thermal electron field distributions. It is inevitable that the numerical errors would grow larger when the input Galactic components have small scale features near or below the discretization resolution. This issue can be handled efficiently by the adaptively refined mesh/pixelization in the future.

Performance

The major computationally heavy process in `hammurabi X` are LoS integration for `HEALPix` map pixels, random field generation with fast Fourier transforms, and tri-linear interpolation for fields prepared in grids (e.g., internal random fields and other external fields). Massive observable production, `HEALPix` map distribution and recycling of physical fields require MPI[11] parallelization are beyond our scope in this report. Technically, we are mainly limited by the `HEALPix` library which has no high-performance support. In the future update we expect to develop a built-in but small high-performance pixelization support based on `HEALPix`. In this work, multi-threading is always useful at the bottom level of paral-

---

[10]An extremely serious simulation should mimic the true observation beam hits, which is computational heavy unless we focus on a small patch of the sky. `hammurabi X` currently implements a computational light method which picks only one sample for each pixel, and so in comparing with astrophysical data we expect the observational resolution is much higher than that of the simulation. Otherwise with low resolution difference, a bias in model constraints may rise in comparing small sky patches since the number of samples may not be large enough to overcome the insufficiency of sample picking in simulation.

[11]Message Passing Interface (MPI) is a standardized and portable message-passing standard designed by a group of researchers from academia and industry to function on a wide variety of parallel computing architectures.

lelism. Fig. 2.7 presents the strong scaling[12] in observable production with various GMF and TE field combinations. The strong speedup with either computationally heavy (with random field generation) or light (without random field generation) pipelines follows Amdahl law [Amdahl, 1967] with around 2% serial remnants. Note that the speedup properties are not very sensitive to the resolution setting in various simulation routines, due to the fact that the workload of pure numerical operations is proportional to the discretization resolution.
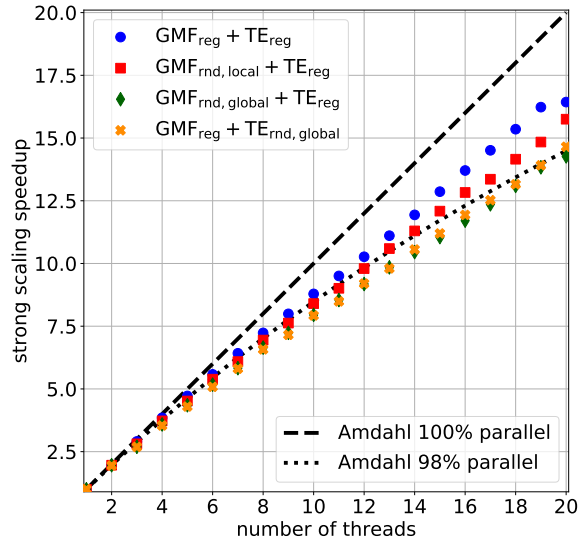

Figure 2.7: `hammurabi X` strong scaling speedup in various tasks, where the subscript "reg" stands for regular fields while "rnd" stands for random fields. No bottle neck from memory access has been observed. The simulation routines are set by default as calculating synchrotron emission with Faraday rotation.

2.3   Synchrotron B/E Ratio

In order to demonstrate the usefulness of `hammurabi X` we investigate the properties of simulated synchrotron emission at high Galactic latitudes according to different random magnetic field configurations. By focusing on the high latitude sky we concentrate on the properties of physical fields near the solar neighborhood where both global and local random generators can be applied.

Alves et al. [2016] reported a synchrotron B/E ratio [13] around 0.35 at spherical modes $l \in (30, 300)$, which a successful modelling of GMF should be able to explain. In addition, a low polarization fraction at high Galactic latitudes is observed [Planck Collaboration et al., 2015]. According to a recent theoretical work by Kandel et al. [2018], it seems possible to achieve synchrotron B/E ratio lower than 1.0 at high Galactic latitudes with compressible MHD turbulence, especially with slow and/or Alfvén mode at low Mach number $M_{\mathrm{A}} < 0.5$. An analytic calculation of the angular power spectrum observed in polarized synchrotron emission is not a trivial task. As presented in theoretical estimations carried out by Caldwell

---

[12]Strong scaling is defined as how the solution time varies with the number of processors for a fixed total problem size.
[13]The ratio between the B-mode and the E-mode of synchrotron angular power spectrum, i.e., $C_\ell^{\mathrm{BB}}/C_\ell^{\mathrm{EE}}$.

et al. [2016], Kandel et al. [2017] and Kandel et al. [2018], it is impossible to avoid a certain level of simplification. Now with the help of `hammurabi X` we can approach this topic numerically.

In order to avoid distractions from other Galactic components or local structure models, in the following simulations we assume uniform distribution for the regular GMF parallel to the Galactic disk and a CRE density with a fixed spectral index. No spatial re-scaling of the field strength is performed, but the global random GMF generator keeps its freedom in field alignment.

2.3.1 High Galactic Latitude Synchrotron Emission

With the improved precision in `hammurabi X`, we present high resolution Galactic synchrotron emission simulations with analytic models as described above. Presented in Fig. 2.8 are the examples of synchrotron polarization at high Galactic latitudes predicted by a uniform regular GMF parallel to the Galactic disk and a random components from the global generator with a Kolmogorov power spectrum. The corresponding maps of synchrotron polarization from the same regular GMF but the local generator using a compressible MHD model are presented in Fig. 2.9. Since we are presenting only illustrative models, the absolute strength of regular and random GMF are not essential here.
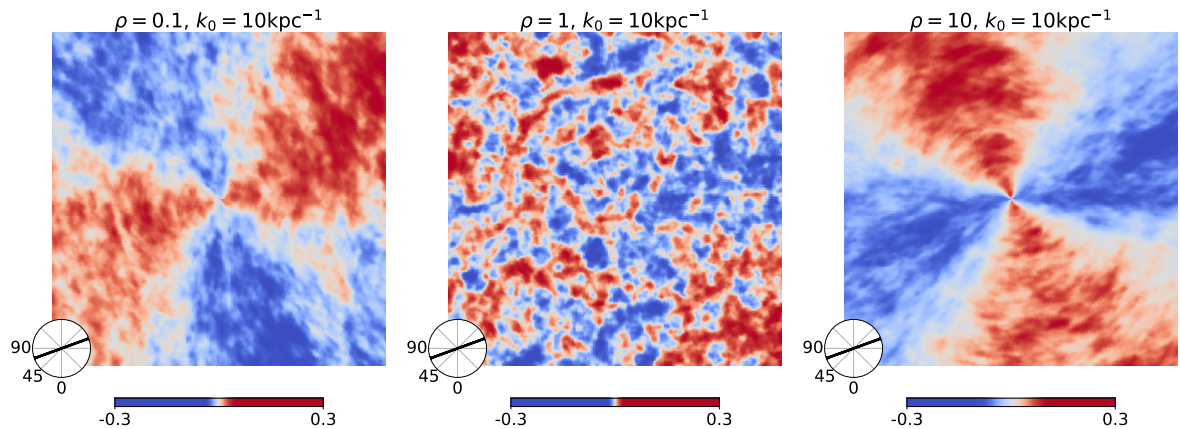

Figure 2.8: 30 GHz synchrotron Stokes Q at the Galactic north pole in a 40 degree patch. The GMF simulation consists of a uniform regular (with orientation displayed on the bottom-left corner of each panel) and global random component with injection scale $k_0 = 10$ kpc^{-1} but different alignment parameter $\rho = 10$ (right), $\rho = 1$ (middle) and $\rho = 0.1$ (left). The strength ratio between the random and regular GMF is $b/B_0 = 3.0$.

The most prominent feature in high latitude synchrotron foreground is the quadrupolar structure that results from the GMF orientation at the solar neighbourhood. As the examples displayed in Fig. 2.8, the quadrupole direction is largely determined by the regular field, but on top of which, we can observe a flip in the polarization between the regimes when $\rho > 1.0$ versus $\rho < 1.0$. When the random GMF has no preferred alignment, i.e., the $\rho = 1.0$ case, the quadrupole pattern is undermined by the spatially isotropic random field contribution. This is visually clear because of the fact that the random field strength dominates. In Fig. 2.9 the quadruple pattern is well preserved with MHD turbulence injection scale $k_0 = 10$ kpc^{-1}, and also a flip in the polarization can be observed with the pure Alfvén mode when

the random field dominates. When the spatial distribution or random GMF is close to spatially isotropic with $P_A/P_{f,s} = 3.0$ (and Alfvén Mach number $M_A = 0.5$, plasma parameter $\beta = 0.1$) as displayed by the middle panel in Fig. 1.5, we observe a similar trend of weakening the quadrupole pattern as demonstrated by Fig. 2.9.
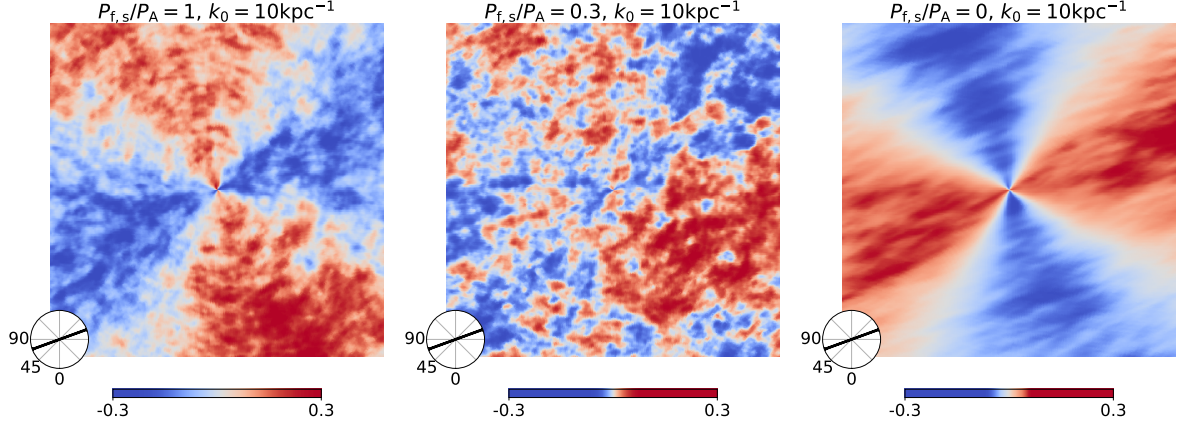

Figure 2.9: 30 GHz synchrotron Stokes Q at the Galactic north pole in a 40 degree patch. The GMF simulation consists of a uniform regular (with orientation displayed on the bottom-left corner of each panel) and a local random component with total spectral power $k_0 P_0/B_0^2 = 75.0$ at injection scale $k_0 = 10$ kpc^{-1}. The Alfvén Mach number $M_A = 0.5$ and plasma parameter $\beta = 0.1$ are set to match the parameterization in Fig. 1.5.

The synchrotron polarization fraction (or the degree of linear polarization) is mainly determined by the CRE spectral shape when a uniformly distributed regular GMF dominates. Assuming a reasonable constant CRE spectral index $\alpha = 3.0$, the synchrotron polarization fraction $\Pi = (3\alpha + 3)/(3\alpha + 7)$ is much higher than that observed from Planck data [Adam et al., 2016]. Fig. 2.10 demonstrates that the synchrotron polarization fraction can be suppressed by a Gaussian random field as long as the random field is not strongly anisotropic in the spatial domain. The suppression in polarization fraction grows with the increasing of random field strength but depends on the specific field modelling. Recall that the addition of a random component to the magnetic field direction functions as a random walk in the polarization plane, which means that even for a purely turbulent field, the polarized intensity continues to increase with the number of turbulent cells added along the LoS. In principle, the increase goes as the square-root of the number of cells, while the total intensity increases linearly, so the fraction should decrease accordingly. In practice, the precise trend is complicated by the effect of the observational beam and the locally varying anisotropy. The shape of the polarization fraction for the $\rho = 0.5$ model in Fig. 2.10, for example, is due to the anisotropic random field canceling with the regular field before beginning to dominate. An inhomogeneous distribution (by field strength regulation) of the random field can change the efficiency of suppression differently depending on the field alignment, but the common features described above are preserved.

The implication of the above analyses is that interpreting the synchrotron polarization toward the poles as due to the local field direction neglects the possible effects of anisotropic turbulence, which can
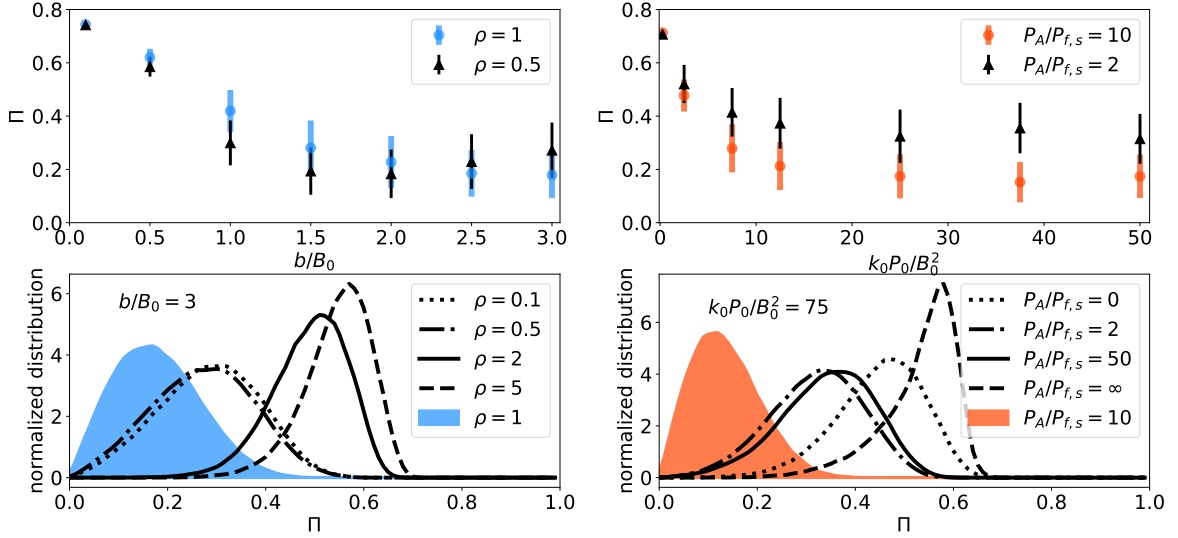
Figure 2.10: Left: Distribution (16th to 68th percentile) of synchrotron polarization fraction Π at high Galactic latitudes produced by a uniform regular and global random GMF. In the top panel is the distribution characterized by mean and standard deviation as a function of random field strength, where the alignment ratio is fixed. In the bottom panel, we show a histogram of polarization fraction where $b/B_0 = 3.0$ and the alignment ratio ρ varies.

Right: Distribution (16th to 68th percentile) of synchrotron polarization fraction Π at high Galactic latitudes produced by uniform regular and local random GMF. In the top panel is the distribution characterized by mean and standard deviation as a function of random field strength, where the anisotropy ratio $P_A/P_{f,s}$ is fixed at the injection scale $k_0 = 10 \text{ kpc}^{-1}$ while the ratio between the total spectral power $P_0 = P_f + P_s + P_A$ at the injection scale and the regular field energy P_0/B_0^2 varies. In the bottom panel, $k_0 P_0/B_0^2 = 75.0$ while the anisotropy ratio $P_A/P_{f,s}$ varies.

mimic or flip the morphology. Though the physical process is different, the geometry of the field and its effect on the observables is the same for polarized dust emission. This work illustrates the opportunity for retrieving useful information of local magnetic turbulence structure with high latitude Galactic polarized emissions, and also shows the challenge from the degeneracy between random and regular magnetic field orientations when using emission data alone. It suggests that we need to be careful about realizing the local GMF structure in order to avoid misleading conclusions. For example it has been proposed recently by Alves et al. [2018] that according to observational evidences, the regular magnetic field structure may play a dominant role in Galactic dust emission near the solar neighbourhood. We also emphasize that the Galactic synchrotron emission is also affected by the warm ISM in the Galactic thick disk and even the halo. The random field generators in `hammurabi X` can be used to bridge the gap between simple large-scale field models and computationally intensive MHD simulations, and boost more realistic analyses and modellings beyond previous methods.

2.3.2   Angular Power Spectrum

The large angular scale Galactic synchrotron polarization pattern driven mainly by the GMF orientation at the solar neighbourhood is quite evident as illustrated in Figures 2.8 and 2.9. However, the small angular structures can be analyzed with the angular power spectrum, which can be decomposed by rotation invariant components, i.e., the T, E and B modes. With the two random field generators proposed in this work, we intend to figure out which properties of the random GMF are imprinted on the synchrotron B/E ratio. Specifically, we are interested in verifying whether MHD turbulence modes are capable of producing B/E < 1.0 in both the perturbative and the non-perturbative regimes. Since we are focusing on high latitude polarization, pixels at Galactic latitude within $\pm 60°$ are masked out. We also set a lower limit to the radius in the LoS integral according to the random field grid resolution and the spherical mode range. Technical details of the precision checks for the pseudo-C_ℓ estimation will be discussed later in this chapter.

We present in Fig. 2.11 the B/E ratio distribution (by collecting results from an ensemble of realizations with each given parameter set) for varying random field strengths and alignments of the global random GMF. Fig. 2.11 implies that to reproduce B/E < 1.0 we either need random GMF in the non-perturbative regime ($b/B_0 > 1.0$) or parallel alignment ($\rho > 1.0$). We also note that the divergence cleaning step is what leads to B/E $\neq$ 1.0. As illustrated in the same figure, all realizations end up with B/E = 1.0 regardless of random field alignment, when the Gram-Schmidt process is switched off. This is acceptable that a simple Gaussian random field should have $E = B$ on average, whereas a magnetic field must be divergence-free and therefore the difference between the naive random vector field and the magnetic field, which has been ignored in many previous researches, is crucial in studying Galactic emissions. Now we conclude that the divergence-free random magnetic field can provide synchrotron B/E $\neq$ 1.0. The Gram-Schmidt cleaning method is computationally useful and correct for reproducing the divergence-free random magnetic field (which in the simplest case can alternatively be obtained from a Gaussian random vector potential as shown in the right panel of Fig. 2.11 where synchrotron $B/E < 1$ arises naturally out of either method in the non-perturbative regime.) and has the added benefit that we can spatially modulate its strength and orientation.

By contrast, the pseudo-C_ℓs estimated from the local MHD realizations have a clear analytic representation. To look for the low B/E ratio according to Kandel et al. [2018], we keep the random GMF strength at the perturbative level and tune the MHD Mach number $M_A = 0.2$ and plasma parameter $\beta = 0.1$. As illustrated in Fig. 2.12, we find clear evidence that a Gaussian realization of MHD turbulence can provide a synchrotron B/E ratio smaller than 1.0, in both perturbative and non-perturbative regimes. The fast mode in a sub-Alfvénic low-β plasma has a unique power spectrum shape and is less affected by the anisotropy function $h(\alpha)$ than the slow mode. By assuming equal power in the turbulence modes at the injection scale, the observed angular power spectra are mainly influenced by the fast mode and so the B/E ratio has a different behavior with respect to the case where slow and Alfvén modes dominate. With the given MHD Mach number and plasma parameter, slow mode turbulence results in a much lower B/E ratio than that from the Alfvén mode, while fast mode prefers B/E $\simeq$ 0.8 in perturbative regime. These features are conceptually consistent with analytic predictions by Kandel et al. [2018] as demonstrated
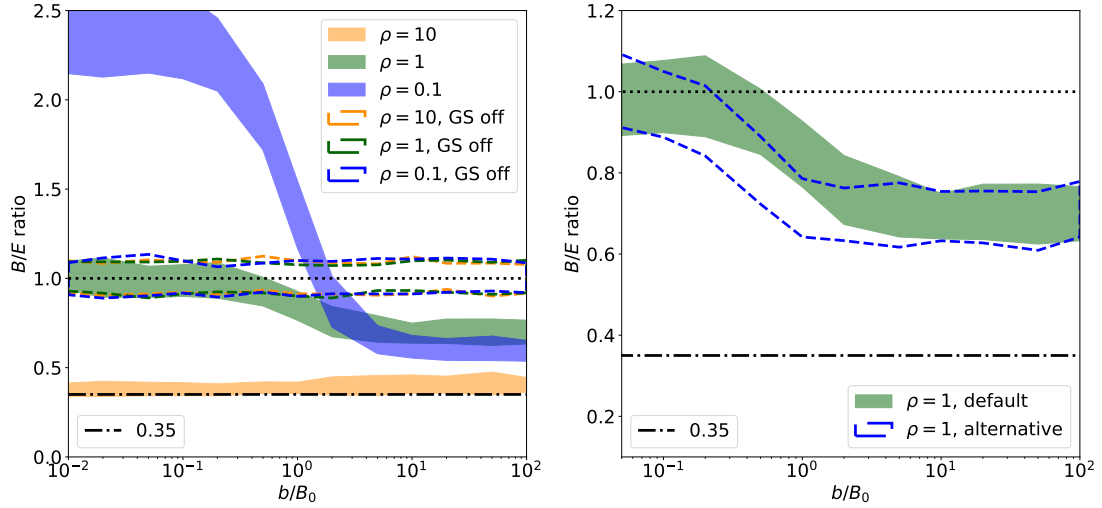
Figure 2.11: Left: Distribution (16th to 68th percentile) of 30 GHz synchrotron emission B/E ratio for $\ell > 100$ according to global random GMF with various field strength and alignment. The results marked by "GS off" come from random GMF without divergence cleaning.

Right: Distribution (16th to 68th percentile) of the 30 GHz synchrotron emission B/E ratio for $\ell > 100$ according to global random GMF with various random field strength. The results marked by "default" come from the default algorithm discussed in § 1.2.3, while "alternative" indicates random GMF generated from the magnetic potential field realizations. The contribution to the angular power spectrum from the regular GMF has been subtracted, which would otherwise dominate the B/E ratio in the perturbative regime ($b \ll B_0$).

in the right panel of Fig. 2.12, where the differences between two estimations are likely because of the simplification in analytic derivation, e.g., the Limber and flat-sky approximations. Beyond the perturbative regime, we observe the B/E ratio evolves with the growth of random field strength and suggests an upper limit for the random field strength in order to achieve the observed B/E ratio with solely MHD turbulence.

According to the observational implications in the Galactic synchrotron emission from above two types of random field realizations, we believe divergence-free and MHD turbulent nature are both important for providing synchrotron B/E < 1.0, besides the divergence-free is the physically indispensable requirement of magnetic field realization. It is possible to use directly the angular power spectra estimated in the way presented here for studying Galactic components like the work by Vansyngel et al. [2018], but we should be aware of the numeric uncertainty if the simulation resolution is lower than that of astrophysical measurements, in addition to the fundamental difference between simulation and observation mentioned earlier.
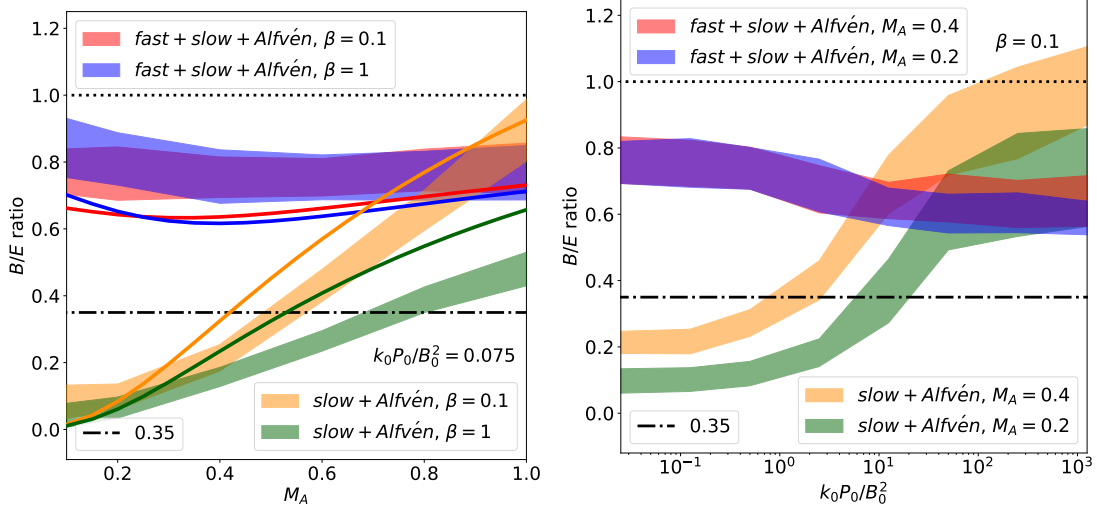
Figure 2.12: Distribution (16th to 68th percentile) of the 30 GHz synchrotron emission B/E ratio for $\ell > 100$ according to the local GMF realizations with various field strengths, Alfvén Mach numbers, and plasma parameters. Solid lines in the left panel are predictions from Kandel et al. [2018]. The fast+slow+Alfvén case sets equal magnetic field power at injection scale for the three modes (i.e., $P_{\mathrm{A}}/P_{\mathrm{f,s}} = 1.0$), while the fast mode is excluded from the slow+Alfvén case (i.e., $P_{\mathrm{f}} = P_{\mathrm{s}}$). The contribution to the angular power spectrum from the regular GMF has been subtracted, which would otherwise dominate the B/E ratio in the perturbative regime ($k_0 P_0 \ll B_0^2$).

2.3.3   Precision of Angular Power Spectrum

In this work, the pseudo-C_ℓs are estimated from an ensemble of simulations with the `NaMaster` [14] toolkit [Alonso et al., 2019]. The left panel of Fig. 2.13 presents a proof of the pseudo-C_ℓ estimation pipeline, where a fiducial spectrum is used to generate multiple realizations of the signal map from which pseudo-C_ℓs are re-estimated with the same mask mentioned in above. To analyze partial-sky observables with the mask described above, we choose band-power binning width $\Delta\ell = 16$. In practice we also select pseudo-C_ℓ with angular mode $l > 100$ after subtracting (in the pixel domain) the contribution of the regular magnetic field to the simulated outputs as mentioned in the captions of Figures 2.11, 2.12 and 2.14. We illustrate the pseudo-C_ℓ estimated from an ensemble of simulated samples with different magnetic field settings in the right panel of Fig. 2.13. From where we notice that the pseudo-C_ℓ estimation with pure regular magnetic field is not correct. This is reasonable since the large angular scale anisotropic pattern created by the regular magnetic field can hardly be estimated from around 13% sky fraction in this work. Fortunately, in the illustrative examples the regular fields are homogeneously defined and so it is feasible and safe to subtract the contribution of regular magnetic field in the pixel domain. We emphasize that this subtraction can not be applied to other general regular field settings, and in our illustrative examples it is critical for the results corresponding to perturbative random magnetic field settings, as we can find out in the right panel of Fig. 2.13. The $\ell > 100$ selection is proposed to avoid any

---
[14] https://github.com/LSSTDESC/NaMaster

potential of un-cleaned spectrum power originated from the non-linear correlation between random and regular fields.
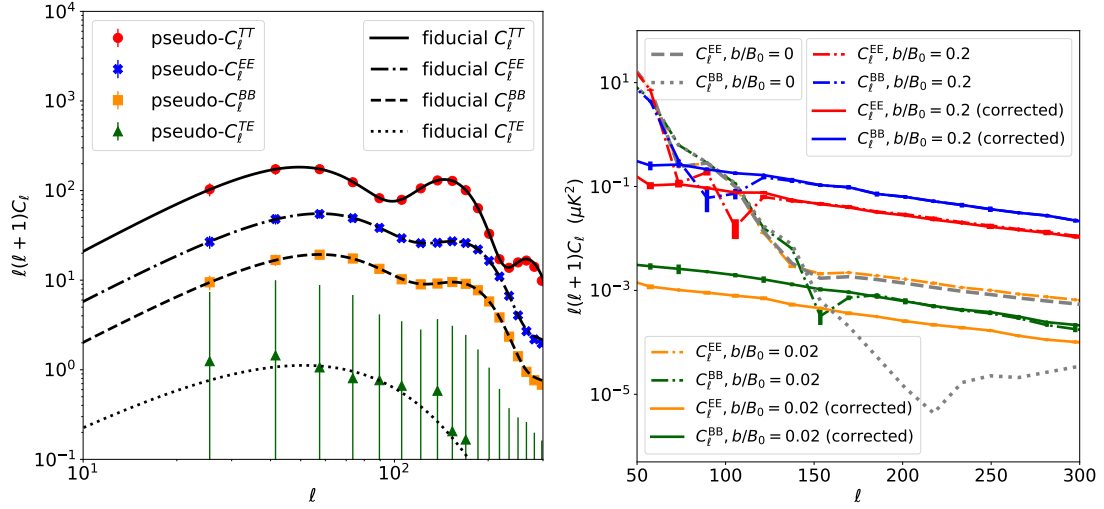

Figure 2.13: Left: Comparison between fiducial angular power spectrum and re-estimated pseudo-C_ℓs with `NaMaster` with multiple observable realizations. T, E and B modes are correctly recovered, while the TE cross-correlation estimation suffers from a large uncertainty. Right: Pseudo-C_ℓs estimated according to global random magnetic fields with $\rho = 10.0$ but different strength. The grey spectra correspond to the uniform regular magnetic field as defined earlier. The dashed color spectra are estimated directly from simulated outputs, while solid colored spectra are estimated after the regular field contribution being subtracted in the pixel domain.

We have presented the precision in calculating the synchrotron polarization in this chapter, the random field realization in § 1, and the pseudo-C_ℓs in Fig. 2.13. To further confirm the correctness of the simulated results obtained above, a conceptual verification is necessary. An analytic approach towards generating the angular power spectrum of tensor fields is not easy and is also beyond our scope. Alternatively, the shape of the Faraday depth angular power spectrum can be inferred from simplified settings of the fields, which serves as a proper check of the random field realization and the angular modes accumulation in the LoS integral.

To begin with, we adopt the total angular momentum method introduced by Hu and White [1997], Hu [2000]. Synchrotron polarization $P(r, \hat{\mathbf{n}}) = Q \pm iU$ from a given geocentric position $\mathbf{r} = -r\hat{\mathbf{n}}$ can be expanded in a polarization basis as

$$P = \int \frac{d^3k}{(a\pi)^3} \sum_\ell \sum_{m=-2}^{2} [E_\ell^{(m)} \pm B_\ell^{(m)}] \times {}_{\pm 2}G_\ell^m(\mathbf{k}, r, \hat{\mathbf{n}}) , \tag{2.32}$$

where for the spin-2 tensor field the basis reads

$$\begin{aligned} {}_{\pm 2}G_2^m &= (-i)^\ell \sqrt{\frac{4\pi}{2\ell+1}} {}_{\pm 2}Y_2^m(\hat{\mathbf{n}})e^{i\mathbf{k}\mathbf{r}} \\ &= \sum_\ell (-i)^\ell \sqrt{4\pi(2\ell+1)}[\epsilon_\ell^{(m)}(kr) \pm i\beta_\ell^{(m)}(kr)] \end{aligned} \tag{2.33}$$

$$\times_{\pm 2}Y_\ell^m(\hat{\mathbf{n}}) \ ,$$

where $_sY_\ell^m(\hat{\mathbf{n}})$ is the spherical harmonic function for a spin-s field. The standard path towards the angular power spectrum E mode C_ℓ^{EE} and B mode C_ℓ^{BB} starts from interpreting the LoS integral of a target foreground observable with base $_{\pm 2}G_\ell^m$ and leads to evaluating

$$C_\ell^{XX} \ = \ \frac{4\pi}{(2\ell+1)^2} \int \frac{d^3k d^3q}{(2\pi)^6} e^{i(\mathbf{q}-\mathbf{k})\mathbf{x}} \tag{2.34}$$
$$\times \sum_m \langle X_\ell^{(m)*}(\mathbf{k}) X_\ell^{(m)}(\mathbf{q})\rangle \ .$$

In the simplest case, we consider only emission sources while ignoring absorption and Faraday rotation, i.e., for a synchrotron polarization tensor $P_\nu(r, \hat{\mathbf{n}})$ at observational frequency ν,

$$-\frac{dP_\nu}{dr} \ = \ \mathcal{S} = j_{pol}e^{2i\chi_0} \ , \tag{2.35}$$

where the basic formulae for polarized emissivity j_{pol} and intrinsic polarization angle χ_0 have been discussed earlier in this chapter. We would thus expect the integral solution to become

$$\frac{E_\ell^{(m)}(\mathbf{k})}{2\ell+1} \ = \ \int dr \frac{_{+2}\mathcal{S}_2^{(m)} + _{-2}\mathcal{S}_2^{(m)}}{2} \epsilon_\ell^{(m)} \ , \tag{2.36}$$

$$\frac{B_\ell^{(m)}(\mathbf{k})}{2\ell+1} \ = \ \int dr \frac{_{+2}\mathcal{S}_2^{(m)} + _{-2}\mathcal{S}_2^{(m)}}{2} \beta_\ell^{(m)} \ , \tag{2.37}$$

where the source terms are determined by

$$\mathcal{S} \ = \ \int \frac{d^3k}{(2\pi)^3} \sum_m \sum_s (_s\mathcal{S}_2^{(m)} {}_sG_2^m) \ . \tag{2.38}$$

It is however not trivial (and thus is commonly avoided without further simplification) to analytically bridge the random GMF and its contribution to synchrotron emissivity expanded in a spherical harmonic basis. Fortunately, Faraday depth is a different story, since the LoS projection of a divergence-free vector field $\mathbf{b}(\mathbf{k})$ can be represented as

$$\mathbf{b}(\mathbf{k})\cdot\hat{\mathbf{n}} = i\sqrt{\frac{4\pi}{3}} \sum_m b^{(m)} \times {}_0Y_1^m(\hat{\mathbf{n}}) \ , \tag{2.39}$$

where the wave-vector $\mathbf{k}$ differs from that in random field realization by a factor of 2π. (Instead of using the total angular momentum method, a similar approximation to the rotation measure structure function has been carried out by Xu and Zhang [2016], which leads to the same conclusion.) The procedure we take for Faraday depth follows the same method for the Doppler effect handled by Hu [2000], where the linear perturbation and Limber approximations [LoVerde and Afshordi, 2008] are key assumptions. By assuming a uniformly distributed TE field, we isolate the perturbation source of Faraday depth in the vector mode ($m = \pm 1$) which results in angular power spectrum

$$C_\ell^{FF} \propto \ell(\ell+1) \int k^2 dk P_b(k) [\int dr \frac{j_l(kr)}{kr}]^2 \ , \tag{2.40}$$

where P_b is power spectrum of random GMF. By applying Limber approximation (which assumes the typical scale of LoS variation of a perturbed field is much larger than that in the angular direction) we have

$$C_\ell^{FF} \propto \int dr P_b(\frac{\ell}{r}) \frac{1}{r^2} \ , \tag{2.41}$$
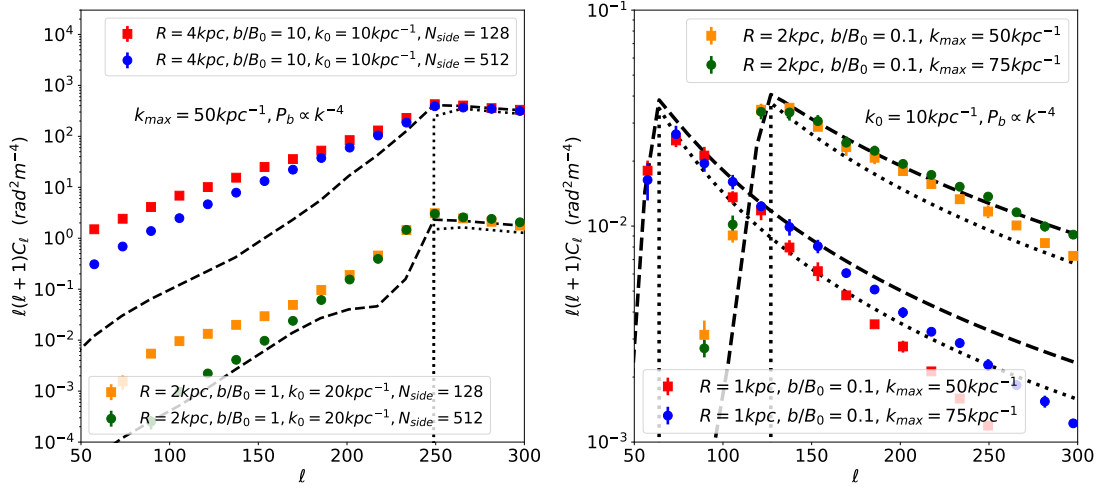
Figure 2.14: Angular power spectra of Faraday depth estimated on thin shells with central radial distance R and width $\Delta R = 0.1$ kpc. Dotted lines represent estimations made with Limber approximation (Eq. 2.41) while dashed lines represent predictions according to numeric integral of spherical Bessel function (Eq. 2.40). Angular power contributed by regular fields has been subtracted.

which suggests the shape of C_ℓ^{FF} is mainly determined by P_b.

Fig. 2.14 present a comparison of the simulation precision with respect to the analytic prediction. For the highest spherical mode $\ell_{\max}$ in analysis and for a random field grid bin of length h, the lower radial limit is roughly set as $R_{\min} \geq h\ell_{\max}/\pi$. Regions closer than $R_{\min}$ or modes above $\ell_{\max}$ are greatly affected by the grid interpolation and may affect the pseudo-C_ℓ estimation. The upper radial limit is defined by the simulation size L within which the random GMF is generated, and $R_{\max} \leq L\ell_{\min}/\pi$ should be satisfied. The LoS radius limits discussed here have no influence in the final conclusions about the B/E ratio but only affecting the precision in estimating pseudo-C_ℓ. To achieve the highest precision without being distracted by multi-shell arrangement, the simulations are done with single shell integrals. The default simulation and output resolutions are identically set as $N_{\text{sice}} = 128$ unless specified. The random field grid by default is built large enough to host radial integral with LoS depth $R_{\max} \simeq 4$ kpc from the observer with field sampling resolution $h \simeq 3$ pc (which means $k_{\max} \simeq 300$ kpc^{-1}) and radial resolution $r \simeq 5$ pc, except that in this appendix we use thin shells with 0.1 kpc thickness and much lower sampling resolution ($k_{\max} < 100$ kpc^{-1}). With a sharp cutoff at an injection scale k_0 in the random GMF models (by ignoring the inverse cascading), we expect a corresponding break in angular power spectrum at $\ell_c \sim 2\pi R_{\max}k_0$. The break position is well recovered independent of the simulation resolution on each thin LoS shell. The power in angular modes below and above the break ℓ_c is affected differently by the spherical and sampling resolution. For $\ell < \ell_c$, the angular resolution (characterized by HEALPix N_{side}) has a dominant influence, suggesting that a larger angular resolution is necessary for more distant shells to suppress the angular power excess. While for $\ell > \ell_c$, the missing angular power (particularly for shells closer to the observer) results from insufficient sampling resolution (characterized by the Nyquist frequency $k_{\max}$) in the random field realization, especially near the observer. Although the illustrations are prepared

with the global random GMF generator, the resolution effects discussed above are generic. Insufficient angular or Galactic component sampling resolution will result in missing power of angular power spectra from simulation outputs. This issue can be handled in a hard way by using inhomogeneous grid or adaptively refined mesh with non-equispaced fast Fourier transform [Keiner et al., 2009] for sampling Galactic components (especially the turbulent fields), and also adaptively refined spherical pixelization. An alternative solution can be nesting sampling grids with different resolution, but the precision loss on the boundary should be carefully estimated and controlled. Now with our theoretically verified Faraday depth anisotropy, we can conclude that our numeric realizations of Gaussian random fields are accurate, and thus that the results regarding the B/E ratio obtained from synchrotron emission simulations should be free from numeric defects.

2.4 Summary

In this chapter we have presented `hammurabi X`, the improved version of `hammurabi`. We have re-designed the package properly with calibrated precision and multi-threading support. This report focuses on the implementation of the synchrotron emission simulation in `hammurabi X` and its relation to the random magnetic field realization. The technical features and profiles in `hammurabi` associated with Galactic synchrotron emission have been, for the first time, reported in detail.

Two fast methods for generating divergence-free Gaussian random magnetic fields covering either Galactic scales or a local region have been proposed in Chap. 1. This is a crucial improvement (in computing accuracy and the capability of realizing physical features) over not only the previous versions of `hammurabi` but also previous fast methods of simulating the GMF and the resulting diffuse Galactic polarized emission from the ISM. It is increasingly clear that simplistic treatments of the turbulent component of the ISM do not produce simulated observables of sufficient complexity to be useful in comparison to the data. Though full MHD turbulence realizations are computationally too expensive for the usage in large-scale GMF model fitting, using the statistical properties of these MHD simulations is an important intermediate step pursued here. The new `hammurabi X` provides the ability for the first time to generate Gaussian simulations that capture some of the properties of fast, slow, and Alvén modes of MHD turbulence in a computationally efficient approximation. Using these more realistic numerical methods for simulating the magnetized ISM will lead to results that can be more directly linked to physical theory.

We have further demonstrated the importance of these improvements by studying two properties of the GMF that have been discussed in the literature. Firstly, we have shown the importance of including a treatment of the anisotropic turbulence in the local ISM when attempting to interpret high-latitude synchrotron polarization as an indication of the local magnetic field direction. Any such modeling of the local field can use `hammurabi X` to quantify how much this affects the results, particularly with the addition of Faraday depth to break the degeneracy of using only polarized diffuse emission. Secondly, using our new numerical methods, we have found that a Gaussian random realization with either the global field orientation alignment or the local MHD parameterization can produce B/E $\simeq 0.35$ in synchrotron emission at high Galactic latitudes. Comparing the B/E ratio predicted by the global random GMF

realizations with and without invoking the Gram-Schmidt process, we have realized that the divergence-free property is essential for such detailed statistical studies of GMFs. Our results conceptually confirm the prediction made by Kandel et al. [2018] for Galactic synchrotron emission, which says the MHD magnetic turbulence has the ability to predict $B/E < 1.0$, while the prediction for dust emission B/E ratio has been conceptually confirmed by Kritsuk et al. [2018]. We have also succeeded in demonstrating the computing power that `hammurabi X` can provide to go beyond analytic studies of Galactic foreground observables with non-perturbative random GMF realizations.

Chapter 3

Cosmic Ray Electron Propagation

3.1 Overview

In many previous studies about the Galactic synchrotron emission, it was considered convenient to model the cosmic-ray electron [1] (CRE) distribution independently from the structure of the Galactic magnetic field (GMF). This approach is theoretically inconsistent, as we know that the CRE distribution is not physically independent from the magnetic field distribution/configuration. Following the quasi-linear test particle approach [Schlickeiser, 2002] in describing the CR propagation through the highly conductive magnetized plasma, the anisotropic spatial and spectral diffusion coefficients are dictated by the specific shape of magnetic turbulence. Although it can be argued that for the independent modelling we focus only on the phenomenological description. With given sufficient astrophysical measurements and appropriate analysis it is always possible to achieve a proper understanding within which the CRE and magnetic field distribution are consistent. Nevertheless, we need to point out that the phenomenological modelling is eventually not helping us in understanding more detailed physical mechanisms. For example, the Galactic synchrotron emission at 10 GHz level mainly [2] results from the CRE with energy roughly around 5 GeV to 30 GeV given the magnetic field strength not stronger than 10 μG and not weaker than 2 μG. Comparing the energy loss time scale to the typical diffusion time scale, one finds that the bulk of the electrons which are contributing to the 10 GHz level synchrotron emissivity in the observer's neighbourhood is mainly from sources (e.g., supernova remnants, pulsars) near the neighbourhood, instead of from faraway sources. Thus it becomes interesting that by analyzing the Galactic synchrotron emission at various frequency and LoS direction we should be able to study the properties of the CR sources, propagation patterns and the magnetic field configurations. This can only be accomplished by including a CRE propagation simulation inside the pipeline of generating synchrotron emission maps, where the synchrotron emissivity we observe

---

[1] By mentioning cosmic-ray electron (CRE) in this dissertation, we actually intend to include both electron and positron, knowing that the energetic positron to electron ratio is less than 0.25 in the Galaxy. The Galactic positrons are largely secondary, which means that they are not directly accelerated/ejected from astrophysical sources but from the interactions between primary CR particles with the ISM. But this "chemical" difference is ignored since we focus more on their kinematics in the magnetized ISM.

[2] According to the Fig. 2.3, the CRE emissivity peaks at certain energy scale corresponds to the specific observational frequency and the ambient magnetic field strength. Softer CRE spectral or higher observational frequency pushes the peaking position to higher energy, while on the contrary, stronger magnetic field strength tends to pull the peak to lower energy.

is calculated with exactly the same magnetic field as estimating the energy loss of CRE propagation. And so instead of starting with an independent parametric description of CRE phase-space distribution, the consistent approach requires physical modellings of the interaction between the energetic CRs and the thermal component in the ISM (e.g., ionizing the neutral atoms, scattering with charged particles and low energy photons) and the magnetic turbulence (e.g., being scattered off by magnetic turbulence, amplifying magnetic turbulence through streaming instability).

The necessity of this consistent picture for CR studies was recently pointed out by Blasi et al. [2012] and Evoli et al. [2018], where they studied the phenomenon of CR being scattered off by magnetic turbulence which in turn is amplified by the CR streaming (in the perturbative regime) before reaching a saturation. The results of their studies pointed out that the interactive picture can explain not only the observed spectral break but also the vertical scale of the CR diffusion region. And such consistent approach is also required in studies which focus on the Galactic ISM, where the CR streaming [Pfrommer et al., 2017] is important for launching of galactic winds [Ruszkowski et al., 2016, Farber et al., 2017], the Parker instability [Heintz and Zweibel, 2018] and the multi-phase medium [Wiener et al., 2016]. Since our research scope is narrowed only to the relativistic electron/positron distribution which has dominant contribution to the synchrotron energy loss (since the protons have a synchrotron lifetime of $(m_{\mathrm{p}}/m_{\mathrm{e}})^4$ times longer than electron and they may lose their energy via other mechanisms without emitting much synchrotron radiation [Rees, 1968]), we do not have to fully resolve the interactive system that is mainly related to CR protons, nor we need to consider the combination of test-particle and test-wave (which describes how the magnetic turbulence responds to the CR flow) approaches. The minimal consistency required for simulating the Galactic synchrotron emission only has to ensure the synchrotron emission we observe is exactly from the synchrotron energy loss during CRE propagation.

To achieve the minimal consistency, we need to numerically solve the CRE transport equation. Numerical packages for simulating CR (not only for electron/positron) propagation have been developed since two decades ago, among which the most popular one is `Galprop` by Strong and Moskalenko [1998] where the CR transport equation is solved with the finite-difference method. More recently Evoli et al. [2017] released the `DRAGON` package with a similar solver as `Galprop` but support for 3D anisotropic modelling of the CR spatial diffusion. We have also witnessed other numerical attempts with finite-volume method or modified finite-difference method, but unfortunately no open access has been provided to their numerical work [Kissmann, 2014].

It is well known that for solving a partial differential equation (PDE) or a set of PDEs, there are generally three categories of numerical approaches: finite difference, finite volume and finite element methods. Each method has its particular advantages and disadvantages, while with appropriate numerical techniques they are all suitable for simulating CR propagation with similar precision. Practically, physicists need well developed numerical libraries with minimal programming requirements in modifying the back-end functions for various simulation tasks. Particularly for simulating the CR propagation, we haven't seen any open-source numerical work with the finite-element method in the community mainly because of the complexity in implementing this method from scratch. Besides, there is no package that can provide us a proper discretization beyond 3D with adaptively refined mesh. With such motivations

we introduce `BIFET`, the toolkit for solving PDEs in a domain with up-to six dimensions (not including the time coordinate) based on the `deal.II` library (an open source finite element library designed to provide well-documented tools to build finite element codes for a broad variety of PDEs). This numerical tool can help us efficiently resolve an isotropic phase-space distribution defined within a very generic domain.

3.2 BIFET

It is known that physical processes and phenomena are conventionally described in the phase-space domain built by time, space and momentum. Depending on the level of detail we focus on, the dimension in which a physical problem lives can be reduced either by integrating over less important coordinates or by assuming certain symmetries. For numerical simulations of cosmic ray (CR) propagation (here we treat CRs as continuous fluids), it is always better to pursue high-dimensional descriptions if not limited by computational methods or resources. Previously without a convenient high-dimensional partial-differential-equation (PDE) solver, we are usually limited to an isotropic CR distribution in the momentum sub-domain and either spherical or cylindrical symmetry in the spatial sub-domain. This has become less favoured as the observation precision has been improved dramatically, and thus simplified modellings are not sufficient for the frontier studies any more.

To cope with the growing requirements in precision and resolution of CR propagation simulation, it is inevitable to consider using mathematically certified libraries to help physicists build numerical simulators properly and efficiently and so to free them from the swamp of mathematics and programming. Here we propose `BIFET`, the bi-domain finite element toolkit, which is a `deal.II` based package that provides convenient functions for solving high-dimensional[3] PDEs. Driven by such motivations, `BIFET` is designed to decompose high-dimensional problems into two sub-domains, e.g., expressing a phase-space distribution with spatial and momentum coordinates separately. The triangulation[4] in each sub-domain can thus be carried out independently, and as well for other mathematical quantities like the finite-element and sparsity pattern. The back-end methods introduced here for assembling high-dimension linear algebra from two sub-domains root deeply in the `deal.II` library.

3.2.1 Underlying Theory

Cosmic Ray Electron Transport

Cosmic rays are referring to the relativistic, generally with energy larger than 1 MeV, charged particles of various species. The Galactic cosmic rays are mainly categorized by a primary component, including proton, electron, helium, carbon, etc., which can be synthesized in the stars, and the secondary [5] component including antiprotons, borons, etc., that are mainly produced during the CR traversing though the Galactic ISM.

---

[3] By high-dimension we mean dimension higher than three.
[4] In geometry, a triangulation is a subdivision of a planar object into triangles, and by extension the subdivision of a higher-dimension geometric object into simplices.
[5] Note that there exists a different primary and secondary definition which distinct cosmic rays observed above and below the earth's atmosphere.

It is known that CRs have frequent interactions with the magnetic turbulence, interstellar photons and thermal particles, and because of which the averaged life time for a CR particle staying the the Galaxy is roughly around 10^6 years. The motion of a single charged particle can be well predicted if the ambient magnetic environment is known. Some numerical simulators, e.g., CRPropa [Batista et al., 2016], follow this idea of calculation, which is precise and convenient for studying static magnetic field structure or tracing the properties of the CR motion within a specifically designed field. Another approach (known as the test particle approach) is to treat the CRs as either an uniform or composite fluid, and in turn the motion of each single particle is not traceable anymore. In this way we approximate the collective behavior of CRs by the Fokker-Planck equations, which take ensemble average of linearly perturbed description of the system consists of the electromagnetic field and charged plasma. The quasi-linear approximation was proved to be acceptable even the magnetic perturbation is four times larger than the regular field strength [Schlickeiser, 2002], which we consider is enough for studying the Galaxy. In the following we will use the test particle approach and build the numerical solving routine.

The up-to-date understandings towards the observed features of CRs are well reviewed recently by Strong et al. [2007], Grenier et al. [2015], Tanabashi et al. [2018] and the references there in. The general trend of the frontier studies of CRs has been pushed forward to the detailed interaction between CRs and other Galactic components like the ionized gas and magnetic field and thus to the consistent description of the Galactic ecology. The non-linear interactive picture which is meant to be simulated is our final aim, and as the first step we have to focus on building the efficient numerical framework with its performance well profiled for the near future studies of the minimal consistent scenario discussed above.

In describing the CRE propagation, we commonly start with the phase-space distribution $u_e(\mathbf{x}, \mathbf{q}, t)$ of energetic electrons[6] and approximate their propagation with a single transport equation mainly with physical terms like spatial and spectral diffusion (scattering off magnetic turbulence), advection (streaming with the bulk motion), spectral advection (re-acceleration and energy loss)

$$\partial_t u_e - \nabla_{\mathbf{x}} \cdot (\mathcal{D}_{\mathbf{xx}}(\nabla_{\mathbf{x}} u_e)) - \nabla_{\mathbf{E}} \cdot (\mathcal{D}_{\mathbf{EE}}(\nabla_{\mathbf{E}} u_e)) \tag{3.1}$$
$$+ \nabla_{\mathbf{x}} \cdot (\mathbf{V} u_e) + \nabla_{\mathbf{E}} \cdot (\mathbf{b} u_e - \frac{1}{3}(\nabla_{\mathbf{x}} \cdot \mathbf{V}) u_e) = Q \ ,$$

where $\mathcal{D}_{\mathbf{xx/EE}}$ represents the spatial/spectral diffusion tensor, $\mathbf{V}$ represents the bulk motion of the CRs, $\mathbf{b}$ indicates continuous energy loss due to several mechanisms like synchrotron emission, inverse-Compton scattering, Coulomb scattering and ionizing ISM, thermal bremsstrahlung. The right-hand-side Q terms stands for astrophysical sources of energetic electrons/positrons.

In the energy loss, here we specify the mechanisms for electrons/positrons, which are slightly different from protons. The inverse Compton scattering describes how energetic electrons/positrons heat ISM photons and kick them to higher frequencies, where the ISM photon field is also known as the interstellar radiation fields (ISRFs, with "fields" for specifying the different components) which consists of various components like CMB photons, star light (covering ultra-violet and optical-inferred bands) and dust emission (mainly covering the inferred bands). Note that the ISRFs are not known purely from observations,

---

[6]According to recent local measurements up to a few years ago and the standard energy loss of secondary positrons [Mauro et al., 2014], the positron excess problem can very likely due to the primary component from nearby pulsars, and so in the following we treat positrons as primaries.

but through modelling the radiative transfer [Popescu et al., 2017] of emission and absorption processes in the ISM and tuned to match certain observables, where the dust density and temperature distribution is modelled. Although the Galactic dust emission is not studied in our current work, the future consistent analysis with polarized synchrotron and dust emission should be aware that the dust distribution is not independent from CRE.

In the simplest case we consider electrons and positrons as a single fluid, by doing so we ignore the secondary production of positrons like the decay of protons and heavier nuclei. A better treatment should involve at least protons/positrons and consequently the interaction between CRs and magnetic turbulence. The spatial and spectral diffusion coefficients $\mathcal{D}_{\mathbf{xx}}$ and $\mathcal{D}_{\mathbf{EE}}$ are often defined phenomenologically because of their complexity. The basic features of $\mathcal{D}_{\mathbf{xx/EE}}$ includes that they depend on the regular magnetic field orientation and turbulent amplitude and shape (according to the quasi-linear theory of CR transport). In the quasi-linear theory the diffusion coefficients can be analytically derived as the Fokker-Planck coefficients by solving the radiation-magneto-hydrodynamic (RMHD) system [Schlickeiser, 2002]. However the reality is more complicated, with theoretical and recent numerical studies [Kulsrud and Cesarsky, 1971, Farber et al., 2017] the CR streaming velocity is not always confined to the Alfvén speed, but the decoupling of CRs to the cold ISM where the magnetic turbulence is damped can be modelled by increasing the spatial diffusion rate along the regular magnetic field orientation.

Although the (already simplified) CRE transport equation sounds complicated from the physical side of view, it can be understood conceptually no more than a non-linear advection-diffusion problem (it is still very non-trivial in practically solving such problem from the numerical side of view).

Finite Element Method

Here we intend to give a simple description of some important concepts in numerical analysis and especially which are involved in solving the CR transport equation with the finite element method. The basic concept is that the finite element method describes a continuous problem in its weak formulation (applying the Galerkin methods) and approximate solution in a finite functional space. For example consider a linear mapping $A : V \rightarrow V$ in a Hilbert space V, a problem is defined as $Au = f$ where u is the solution. Instead of solving $Au = f$ directly, the weak formulation seeks the solution with a test function $v \in V$ and convert the problem into

$$\langle Au, v \rangle = \langle f, v \rangle \ , \tag{3.2}$$

where $\langle \cdot, \cdot \rangle$ represents a bi-linear form (which in the applications here it indicates a domain integral). Then with a set of basis functions $\{\phi_i\} \subset V$ we try to describe $u = \sum_i \mathcal{U}_i \phi_i$ and consequently the weak formulation reads

$$\sum_j \mathcal{U}_j \langle A\phi_j, \phi_i \rangle = \langle f, \phi_i \rangle \ , \tag{3.3}$$

and the solution finding eventually becomes solving the linear algebra that represents the weak form above. Note that the above formulas are defined in the continuous domain. While for the discrete domain where

the functional base is described with quadrature points, we use notation u_h for representing the discrete solution.

By the decomposition in the finite functional space in the discrete domain, the solution precision is largely determined by how we choose the functional basis and quadrature points, which are in principle independent from the finite element method itself. For example we can take the Gaussian quadrature which means with arbitrary n points $\{x_i\}$ and weights $\{w_i\}$ in one-dimensional domain $[a, b]$, an integral of function $g(x)$ can be approximated as

$$\int_a^b g(x)dx \quad = \quad \sum_i \epsilon_i g(x_i) \ , \tag{3.4}$$

$$\epsilon_i \quad = \quad \int_a^b \prod_{j \neq i} \frac{x - x_j}{x_i - x_j} dx \ , \tag{3.5}$$

which has a degree of precision at most $2n - 1$. By applying the quadrature rule to the weak formulation we can further write Eq. 3.3 as

$$\sum_j \mathcal{U}_j \sum_k \epsilon_k^2 A(x_k)\phi_j(x_k)\phi_i(x_k) = \sum_k \epsilon_k f(x_k)\phi_i(x_k) \ , \tag{3.6}$$

where the continuous integrals have been approximated by discrete summation, and consequently the solution u is approximated by its discrete counterpart $u_h(x_k) = \sum_i \mathcal{U}\phi_i(x_k)$.

The left hand side integral in Eq. 3.6 is not trivial as it appears. Here we illustrate a more realistic derivation with a one-dimensional diffusion problem, which reads

$$-\partial_x(\alpha\partial_x u) = f(x) \ . \tag{3.7}$$

For its weak formulation we define the functional base $\{\phi_i\}$ and the discrete solution u_h follows from:

$$-\sum_j \mathcal{U}_j \langle \phi_i, \partial_x(\alpha\partial_x \phi_j) \rangle_\Omega = \langle f, \phi_i \rangle_\Omega \ , \tag{3.8}$$

where the problem is defined within the domain Ω with boundary surface $\partial\Omega$. Integrating the left-hand-side by part, we arrive at

$$\sum_j \mathcal{U}_j \left[\langle \partial_x \phi_i, \alpha\partial_x \phi_j \rangle_\Omega - (\alpha\phi_i, \partial_x \phi_j \cdot \hat{n})_{\partial\Omega} \right] = \langle f, \phi_i \rangle_\Omega \ , \tag{3.9}$$

with $\hat{n}$ represents the direction of the boundary surface. In practice the partial derivation of base functions $\partial_x \phi_i$ are pre-defined as the functional base itself. It is also apparent that Eq. 3.9 is in principle a set of linear equations

$$\sum_j \mathcal{M}_{i,j}\mathcal{U}_j = \mathcal{R}_i \ , \tag{3.10}$$

where $\mathcal{M}$ is known as the left-hand-side system matrix, while $\mathcal{R}$ is the right-hand-side system vector. The boundary conditions we have not included in defining the strong formulation usually applies to the boundary integral presented above, where a strong boundary condition requires specific shape of ϕ_i or $\partial_x \phi_i$ at the boundary surface, whereas a nature boundary condition can simplify the integral with vanishing terms. Take the diffusion problem above for example, a strong boundary condition can be

$u(x) = g$ for $x \in \partial\Omega$ and consequently the surface integral in Eq. 3.9 should be moved to the right-hand-side by replacing ϕ_i with g. While with a weak boundary condition we can ask $\partial_x u(x) = 0$ for $x \in \partial\Omega$, in which case the surface integral vanishes since $\partial_x \phi_j = 0$ and note that this requirement will not show up explicitly in solving the linear equations.

For some particular problems, e.g., the advection problem (or hyperbolic partial differential equation), we need extra caution with the discretization scheme. In practice for advection problems we use the upwind discontinuous Galerkin method, where the discontinuous means the functional basis is defined independently for each triangulated cell and so the solution u_h do not have to be continuous at the internal boundaries between two neighbouring cells. Assuming a simple one-dimensional advection problem

$$\partial_x(\beta u) = f(x) \ , \tag{3.11}$$

and the plain weak formulation in functional base ϕ_m reads

$$-(\phi_m, u_h \beta \cdot \hat{n})_{\partial\Omega} + \sum_i \langle u_h, \beta \cdot \partial_x \phi_m \rangle_{T_i} = \sum_i \langle \phi_m, f \rangle_{T_i} \ , \tag{3.12}$$

where $\partial\Omega$ represents the external boundary surface, $T_i \in \mathbb{T}$ represents the volume for each triangulation cell i, the notation $(\cdot, \cdot)$ indicates surface integral while $\langle \cdot, \cdot \rangle$ for volume integral. Then on top which we apply the upwind scheme, which introduces extra internal surface integrals $+\sum_j (u_h^-, \beta \cdot [\phi_m \hat{n}])_{F_j}$ on the left-hand-side, where $F_j \in \mathbb{F}$ represents the internal surface j. $[\phi_m \hat{n}]$ is defined by $[\phi_m \hat{n}] = \phi_m^+ \hat{n}^+ + \phi_m^- \hat{n}^-$ where the notation $+$ indicates the quantity in the upwind cell while $-$ for the downwind cell. Note that in the discrete Galerkin method, the functional basis is defined independently for each cell.

Domain Separation

The `deal.II` library provides triangulation methods for a domain with number of dimensions no higher than three, which is a common setting of a finite element method library, and so for problems defined within higher dimensions (e.g., a CR propagation problem with three spatial dimension and one spectral dimension) we cannot build the mathematical framework directly with its original library functions. To overcome this, we separate the full domain into a spatial sub-domain (denoting the spatial space $\mathbf{x}$) and a spectral sub-domain (denoting the energy/momentum space $\mathbf{q}$). By default the spatial and spectral sub-domains are constructed as hyper-rectangles. The notation $\mathbb{R}^{a+b}$ is defined for distinguishing different dimension settings, where "a" represents the number of dimensions in the spatial sub-domain while "b" represents that in the spectral sub-domain. For example $\mathbb{R}^{1+1}$ setting is built by $\{x_1, q_1\}$, while $\mathbb{R}^{2+1}$ setting is built by $\{x_1, x_2, q_1\}$.

Without any loss of generality, we assume an unspecified time-dependent problem in the form of

$$\partial_t u + \hat{\mathcal{O}} u = f, \tag{3.13}$$

in an arbitrary R^{a+b} dimension setting. The discretization in time can be approached by a sequence of time steps with solutions $u^n(\mathbf{x}, \mathbf{q})$ marked by time step index n, i.e., the finite difference approach for the time discretization. In the Rothe's scheme we can rephrase the time-dependent problem as

$$\frac{u^n - u^{n-1}}{t_n - t_{n-1}} + ((1-\theta)\hat{\mathcal{O}}_{n-1} u^{n-1} + \theta \hat{\mathcal{O}}_n u^n) = (1-\theta)f_{n-1} + \theta f_n \ , \tag{3.14}$$

where θ varies within $[0, 1]$. $\theta = 1$ and 0 represents implicit and explicit Euler method respectively, while $\theta = 0.5$ is the alleged Crank-Nicolson method. For a time-independent problem, a steady state solution can be found technically by a single solving step within the θ-scheme we described above.

Intuitively, we express solution u^n inside the cross product Φ of two functional spaces as

$$
\begin{aligned}
u^n(\mathbf{x}, \mathbf{q}) &= \sum_i \sum_\alpha \mathcal{U}^{\alpha i} v_i(\mathbf{x}) w_\alpha(\mathbf{q}) \\
&= \sum_{\alpha, i} \mathcal{U}^{\alpha i} \phi_{\alpha i}(\mathbf{x}, \mathbf{q}) \ ,
\end{aligned}
\tag{3.15}
$$

where the base function spaces are mathematically defined by

$$
\mathcal{V} \quad := \quad span\{v_i \in H^1(\mathbb{R}^a)\} \ , \tag{3.16}
$$

$$
\mathcal{W} \quad := \quad span\{w_\alpha \in H^1(\mathbb{R}^b)\} \ , \tag{3.17}
$$

$$
\Phi \quad := \quad span\{\phi_{\alpha i} \in \mathcal{V} \otimes \mathcal{W}\} \ . \tag{3.18}
$$

Discretizing a PDE problem over quadrature points yields the weak formulation, where generally we can represent the left-hand-side operator $\hat{\mathcal{O}}$ by a sparse matrix $\mathcal{M}_{\mathbf{xq}}$. Whereas the right-hand-side terms can be assembled into a matrix representative $\mathcal{R}_{\mathbf{xq}}$, and in this way the generic weak formulation has the form

$$
\mathcal{M}_{\mathbf{xq}} \cdot vec(\mathcal{U}) = vec(\mathcal{R}_{\mathbf{xq}}) \ . \tag{3.19}
$$

The reason for vectorizing (with *vec* denoting the matrix vectorization operation) the solution matrix $\mathcal{U}$ and the right-hand-side matrix $\mathcal{R}$ can be understood via a simplified example. Suppose upon the solution representative $\mathcal{U}$ we apply two independent operations $\hat{\mathcal{O}}_{\mathbf{x}}$ and $\hat{\mathcal{O}}_{\mathbf{q}}$ which live separately in two sub-domains (to be specific, $\hat{\mathcal{O}}_{\mathbf{x}} \equiv \hat{\mathcal{O}}_{\mathbf{x}}(\mathbf{x})$ and $\hat{\mathcal{O}}_{\mathbf{q}} \equiv \hat{\mathcal{O}}_{\mathbf{q}}(\mathbf{q})$). It is thus straight forward to assemble matrix representatives $\mathcal{M}_{\mathbf{x}}$ and $\mathcal{M}_{\mathbf{q}}$ respectively, namely the mapping from the strong formulation to the weak formulation, which reads

$$
\hat{\mathcal{O}}_{\mathbf{x}} \hat{\mathcal{O}}_{\mathbf{q}} u \rightarrow \mathcal{M}_{\mathbf{x}} \mathcal{U} \mathcal{M}_{\mathbf{q}}^T \ , \tag{3.20}
$$

where $(\cdot)^T$ stands for matrix transpose. By default we associate the row indices to quadrature points in the spatial sub-domain. It is obvious at this point that solving a Sylvester-like equation requires a vectorization and consequently the final left-hand-side matrix reads $\mathcal{M}_{\mathbf{xq}} = \mathcal{M}_{\mathbf{q}} \otimes \mathcal{M}_{\mathbf{x}}$. And through this vectorization, we could also assemble $\mathcal{M}_{\mathbf{xq}}$ for even the most generic $\hat{\mathcal{O}}(\mathbf{x}, \mathbf{q})$ with a quadrature-point-wise Kronecker product (represented by the symbol $\otimes$).

For physicists who are not very familiar with the finite element method (FEM), we feel obliged to illustrate explicitly the methodology behind assembling the $\mathcal{M}_{\mathbf{xq}}$ (the very same idea goes to assembling the $\mathcal{R}_{\mathbf{xq}}$). A typical example can be a pure spatial diffusion problem, where a strong formulation of the diffusion term (on the left-hand-side of a PDE) can be

$$
- \nabla_{\mathbf{x}} \cdot (\mathcal{D}_{\mathbf{xx}} \nabla_{\mathbf{x}} u(\mathbf{x}, \mathbf{q})) \ , \tag{3.21}
$$

where $\mathcal{D}_{\mathbf{xx}} \equiv \mathcal{D}_{\mathbf{xx}}(\mathbf{x}, \mathbf{q})$ represents the spatial diffusion tensor. The standard approach is to perform a integral (over the phase-space domain) on both hand sides of the strong formulation of the problem with

appropriate base functions $\{\phi_{\alpha i} = w_\alpha v_i\}$, which reads

$$- \int_{\Omega_{\mathbf{xq}}} \phi_{\alpha i} \nabla_{\mathbf{x}} \cdot (\mathcal{D}_{\mathbf{xx}} \nabla_{\mathbf{x}} u) \ . \tag{3.22}$$

The continuous Galerkin method, taken as a convenient example for discretizing a pure diffusion problem, instructs $u(\mathbf{x}, \mathbf{q}) = \sum_{\beta,j} \mathcal{U}^{\beta j} \phi_{\beta j}$, and through a integration by part we can express the above term as

$$\sum_{\beta,j} \mathcal{U}^{\beta j} \int_\Omega (\nabla_{\mathbf{x}} \phi_{\alpha i}) \mathcal{D}_{\mathbf{xx}} \nabla_{\mathbf{x}} \phi_{\beta j} \ , \tag{3.23}$$

where $\Omega \equiv \Omega_x \otimes \Omega_q$ represents the volume integral in two sub-domains, with the integrand explicitly reads

$$(\nabla_{\mathbf{x}} v_j)^T \cdot (\mathcal{D}(\mathbf{x}, p) \nabla_{\mathbf{x}} v_i) \cdot (w_\alpha w_\beta) \ . \tag{3.24}$$

Note that `deal.II` can handle the discrete integral with continuous or discontinuous base functions in a cell-by-cell manner (based on continuous or discontinuous Galerkin method), so that a common CR propagation problem with diffusion and advection terms can be properly defined. Logically in `BIFET` what we do is to first iterate over active cell-pairs living in the two sub-domains, and then iterates through quadrature points are conducted where the accumulations of $\mathcal{M}_{\mathbf{xq}}$ and $\mathcal{R}_{\mathbf{xq}}$ are done as discrete integrals. Notice that a integral over two sub-domains is required, so we end up with four levels of nested iterations. Although the strong formula was defined in one-dimensional domain or sub-domains, the algorithms are dimension free.

3.2.2 Software Design

As mentioned earlier that the main feature we implement in `BIFET` is assembling the linear algebra structure with triangulation performed in two domains independently. In the following we present the technical details related to building the numerical system for solving a high-dimensional PDE. An illustrative `BIFET` workflow chart is presented by Fig. 3.1, where the whole routine mainly consists of two processes, one is shown on the left side of the workflow corresponds to initializing/refining and storing the linear algebra system of the PDEs, while the right side of the workflow displays the operations related to solving the PDE system and interacting with the conditions.
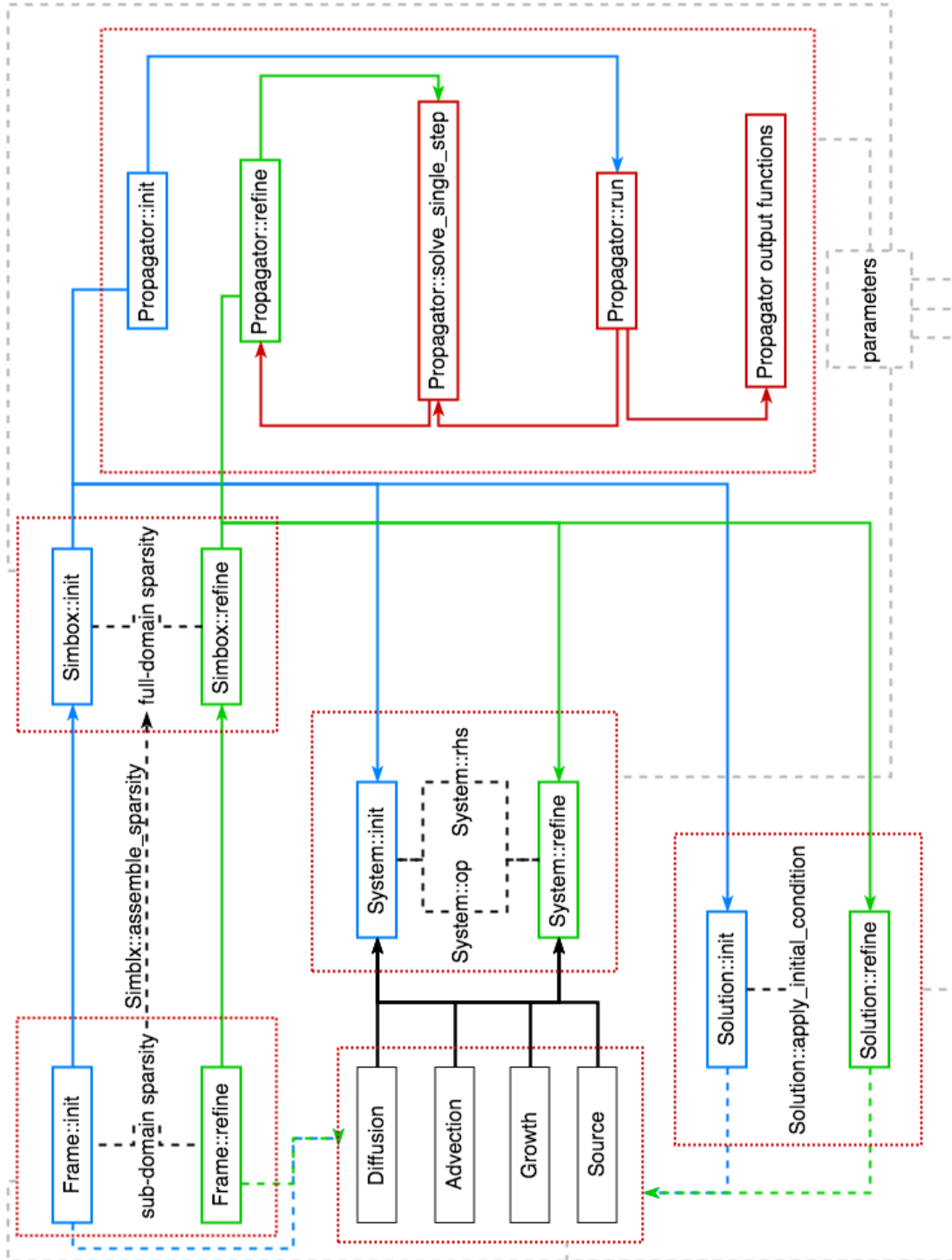
Figure 3.1: `BIFET` workflow.

Domains

While physically we distinguish between spatial and spectral domains, which are not different from the numerical point of view. Technically we distinguish domain discretization with continuous Galerkin method from that with the discontinuous Galerkin. In the *Frame* class we define the basic quantities for describing a domain, which include mesh/grid geometry and size, finite element degrees of freedom, dynamic sparsity pattern, strong boundary condition and hanging node constraints. The process of initializing a single domain setting starts with the given mesh/grid shape, size and discretization, from where the triangulation can be done automatically with built-in method of `deal.II` library. After which, with given finite element method, we can estimate the degrees of freedom and dynamic sparsity pattern according to the initial discretization, where the degrees of freedom represents how many independent unknown variables in the final solution, while the sparsity pattern describes the basic shape of the linear system left-hand-side matrix. Hanging node constraints are important only for continuous Galerkin method, where the solution is required to be continuous at the boundary of two neighbouring cells. Note that these constraints should not be used for the discontinuous Galerkin method. Here we present the implementation of the initializing process in *Frame* class.

```cpp
template <int dim> void Frame<dim>::init() {
  // triangulate simulation box
  dealii::GridGenerator::subdivided_hyper_rectangle(
                         *(this->triangulation),
                         this->block_nums, this->pivot_min,
                         this->pivot_max, true);
  // if min_refine_lv is 0, no refinement operation will be taken
  this->triangulation->refine_global(this->min_refine_lv);
  // enumerate dof
  this->dof_handler->distribute_dofs(*(this->fe));
  // apply dof to constraints
  this->constraints->clear();
  dealii::DoFTools::make_hanging_node_constraints(
                         *(this->dof_handler),
                         *(this->constraints));
  // apply strong boundary
  this->bfmap_init();
  dealii::VectorTools::interpolate_boundary_values(
                         *(this->dof_handler),
                         *(this->bfmap),
                         *(this->constraints));
  this->constraints->close();
  // initialize dynamic sparsity
```

```
24    this->dsp->reinit(this->dof_handler->n_dofs(),
25                                this->dof_handler->n_dofs());
26    dealii::DoFTools::make_sparsity_pattern(
27                                *(this->dof_handler),
28                                *(this->dsp),
29                                *(this->constraints),
30                                /*keep_constrained_dofs=*/false);
31    this->sparsity->copy_from(*(this->dsp));
32  }
```

Sparsity Pattern

The sparsity pattern (as introduced above) for a single sub-domain, i.e., $\mathcal{S}_{\mathbf{x}}$ for the spatial domain and $\mathcal{S}_{\mathbf{q}}$ for the spectral domain, is built during initializing the *Frame* instance. For the system left-hand-side matrix which absorbs the system matrices from two sub-domains, the corresponding sparsity pattern is calculated as

$$\mathcal{S}_{\mathbf{xq}} = \mathcal{S}_{\mathbf{q}} \otimes \mathcal{S}_{\mathbf{x}} \,, \tag{3.25}$$

which is generic and independent of the specific expression of the system matrix itself. In the following we present the implementation of the Kronecker product described in Eq. 3.25. This function is defined in the *Simbox* class along with functions for refining sub-domains.

```
1   template <int spa_dim, int spe_dim>
2   void Simbox<spa_dim, spe_dim>::Kronecker_product() {
3     // reallocate result DSP
4     this->dsp->reinit(
5         this->spectral_frame->dsp->n_rows() * this->spatial_frame->dsp->n_rows(),
6         this->spectral_frame->dsp->n_cols() * this->spatial_frame->dsp->n_cols());
7     // loop through non-zero entries in left DSP
8     auto it_left = this->spectral_frame->dsp->begin();
9     auto end_left = this->spectral_frame->dsp->end();
10    for (; it_left != end_left; ++it_left) {
11      auto alpha = it_left->row();
12      auto beta = it_left->column();
13      // loop through non-zero entries in right DSP
14      auto it_right = this->spatial_frame->dsp->begin();
15      auto end_right = this->spatial_frame->dsp->end();
16      for (; it_right != end_right; ++it_right) {
17        // get global indeces
```

```
18        auto I = alpha * this->spatial_frame->dsp->n_rows() + it_right->row();

19        auto J = beta * this->spatial_frame->dsp->n_cols() + it_right->column();

20        this->dsp->add(I, J);

21      }

22    }

23  }
```

System Assembling

The sparsity pattern for the full domain is useful in assembling and storing the system left-hand-side matrix. The basic idea of assembling a system matrix is similar to the standard way defined in `deal.II` library, where local matrices are assembled in a cell-wise manner and then distributed into the global matrix. Since we are independently handling two sub-domains, the iteration at cell level is nested, which means a local matrix is not associated to a single cell but to a couple of cells from two sub-domains. The assembling method of local matrices in each domain is still valid, while distributing local matrices to the global matrix requires the same method in `deal.II` and the Kronecker product which merge the global sub-domain system matrices into the global full domain matrix. Note that the Kronecker product in merging two global matrices is not relevant to whether the left-hand-side operators can be decomposed into two sub-domains, since during the cell-wise assembling of the local matrices we naturally use the specific expression (with nested iterations of quadrature points in both sub-domains) of the left-hand-side operators. The snippet below presents the system initialization function for a pure spatial diffusion problem, where the diffusion tensor is defined within *System* class (which applies to the definition of advection vector and source distribution).

```
1   template <int spa_dim, int spe_dim>

2   void System_tmp<spa_dim, spe_dim>::Operator::init(

3                           System<spa_dim, spe_dim> *system,

4                           const Simbox<spa_dim, spe_dim> *simbox,

5                           const double &step_time) {

6     // step 1, preparation

7     // instantiate quadrature rules in two sub-domains

8     auto spatial_quadrature_formula =

9     std::make_unique<dealii::QGauss<spa_dim>>(

10                          simbox->spatial_frame->fe->degree + 1);

11    auto spectral_quadrature_formula =

12    std::make_unique<dealii::QGauss<spe_dim>>(

13                          simbox->spectral_frame->fe->degree + 1);

14    // prepare finite element base function values in spatial domain

15    auto spatial_fev = std::make_unique<dealii::FEValues<spa_dim>>(
```

```
16                                  *(simbox->spatial_frame->fe),
17                                  *spatial_quadrature_formula,
18                                  dealii::update_gradients |
19                                  dealii::update_quadrature_points |
20                                  dealii::update_JxW_values);
21    // prepare finite element base function values in spatial domain
22    auto spectral_fev = std::make_unique<dealii::FEValues<spe_dim>>(
23                                  *(simbox->spectral_frame->fe),
24                                  *spectral_quadrature_formula,
25                                  dealii::update_values |
26                                  dealii::update_quadrature_points |
27                                  dealii::update_JxW_values);
28    // degrees of freedom per cell (DPC) in two sub-domains
29    const unsigned int spatial_dpc = spatial_fev->dofs_per_cell;
30    const unsigned int spectral_dpc = spectral_fev->dofs_per_cell;
31    // number of quadrature points per cell in two sub-domains
32    const unsigned int spatial_q_points =
33    spatial_quadrature_formula->size();
34    const unsigned int spectral_q_points =
35    spectral_quadrature_formula->size();
36    // local to global matrix indices translater
37    auto spatial_l2g =
38    std::make_unique<std::vector<dealii::types::global_dof_index>>(
39                                  spatial_dpc);
40    auto spectral_l2g =
41    std::make_unique<std::vector<dealii::types::global_dof_index>>(
42                                  spectral_dpc);
43    // temporary local (per-cell) matrix caches
44    auto cell_Mx =
45    std::make_unique<dealii::FullMatrix<double>>(spatial_dpc,
46                                                  spatial_dpc);
47    auto cell_Mq =
48    std::make_unique<dealii::FullMatrix<double>>(spectral_dpc,
49                                                  spectral_dpc);
50    // system matrix allocation
51    system->Mxq->reinit(*(simbox->sparsity));
52
53    // step 2, fill system matrix
54    // apply integral with base functions over sub-domains
```

```cpp
55      // iterate over sub-domain cells (spatial domain)
56  #ifdef _OPENMP
57    system->omp_cell_distribute(simbox);
58    for (auto spatial_cell = system->it_start;
59         spatial_cell != system->it_end;
60         ++spatial_cell)
61  #else
62      for (const auto& spatial_cell :
63      simbox->spatial_frame->dof_handler->active_cell_iterators())
64  #endif
65      {
66        // initialize finite element values at given cell
67        spatial_fev->reinit(spatial_cell);
68        // translate local indices to global indices
69        spatial_cell->get_dof_indices(*spatial_l2g);
70        // iterate over sub-domain cells (spectral domain)
71        for (const auto& spectral_cell :
72        simbox->spectral_frame->dof_handler->active_cell_iterators())
73        {
74          spectral_fev->reinit(spectral_cell);
75          // translate local indices to global indices
76          spectral_cell->get_dof_indices(*spectral_l2g);
77          // apply quadrature rule in spectral domain
78          for (unsigned int spectral_qid = 0;
79               spectral_qid < spectral_q_points;
80               ++spectral_qid) {
81            // spectral domain local full matrix
82            for (dealii::types::global_dof_index alpha = 0;
83                 alpha < spectral_dpc;
84                 ++alpha) {
85              for (dealii::types::global_dof_index beta = 0;
86                   beta < spectral_dpc;
87                   ++beta) {
88                cell_Mq->set(alpha, beta,
89                             spectral_fev->shape_value(alpha,
90                                                          spectral_qid) *
91                             spectral_fev->shape_value(beta,
92                                                          spectral_qid) *
93                             spectral_fev->JxW(spectral_qid));
```

```
94              } // beta
95            }   // alpha
96         // (clean cache)
97         system->Mq->reinit(*(simbox->spectral_frame->sparsity));
98         // (push local full matrix to global sparse matrix cache)
99         simbox->spectral_frame->constraints
100                          ->distribute_local_to_global(
101                                  *cell_Mq,
102                                  *spectral_l2g,
103                                  *(system->Mq));
104         // apply quadrature rule in spatial domain
105         for (unsigned int spatial_qid = 0;
106              spatial_qid < spatial_q_points;
107              ++spatial_qid) {
108           // get spatial diffusion tensor at given quadrature point
109           const dealii::Tensor<2, spa_dim, double> coefficient{
110             system->diffusion->Dxx(
111                     spatial_fev->quadrature_point(spatial_qid),
112                     spectral_fev->quadrature_point(spectral_qid),
113                     step_time)};
114           // spatial domain local full matrix
115           for (dealii::types::global_dof_index i = 0;
116                i < spatial_dpc;
117                ++i) {
118             for (dealii::types::global_dof_index j = 0;
119                  j < spatial_dpc;
120                  ++j) {
121               cell_Mx->set(i, j,
122                   dealii::scalar_product(
123                   spatial_fev->shape_grad(i, spatial_qid),
124                   coefficient *
125                   spatial_fev->shape_grad(j, spatial_qid)) *
126                   spatial_fev->JxW(spatial_qid));
127             } // j
128           }   // i
129         // (clean cache)
130         system->Mx->reinit(*(simbox->spatial_frame->sparsity));
131         // (push local full matrix to global sparse matrix cache)
132         simbox->spatial_frame->constraints
```

```
133                              ->distribute_local_to_global(
134                                   *cell_Mx,
135                                   *spatial_l2g,
136                                   *(system->Mx));
137             // accumulate to global matrix cache
138             system->Operator_Kronecker_accumulate(simbox);
139           } // spatial quadrature point
140         }    // spectral quadrature point
141       }      // spectral cell
142     }        // spatial cell
143 }
```

multi-threading support

In the first version of `BIFET` we apply multi-threading parallelism mainly to the system assembling process, which has already been illustrated by the snippet above. We will see later in the profiling that by allocate the cell iterations into multiply thread is efficient until the bottleneck from memory accessing is reached. This bottleneck is purely due to the fact that we have to allocate and compute all the non-zero elements of system matrix. To over come which, it is essential in the future to implement MPI support with a matrix-free scheme in system matrix calculation, where the system matrix do not have to be pre-calculated and in turn reduces greatly the computing memory consumption and makes the process easy to be paralleled.

3.2.3   Precision and Performance

Performance

The common routines associated to building and solving PDE system in `BIFET` are data-intensive. The largest memory consumption comes from assembling PDE operator matrices. Each operator matrix size is defined together by the domain resolution (namely, the number of cells), the base function polynomial order (which determines the degrees of freedom per cell) and the problem dimension. The main idea for computational parallelism is to distribute the workload related to accessing these matrices since the operator matrices always stay in the RAM (random-access memory). At the lowest optimizing level we apply a multi-threading with `OpenMP`[7], which is easy to be implemented and nested inside other packages, i.e., the `IMAGINE` pipeline with multi-node parallelism.

A standard simulation routine of `BIFET` is mainly built by iterations with three major processes: the system initialization, system solver and (non-)adaptive refinement. Fig. 3.2 illustrates the CPU time consumption for handling simple time-independent diffusion and advection problems with $\mathbb{R}^{1+1}$ dimension setting by serial routines in `BIFET`. The CPU time cost of system initialization and refinement are roughly proportional to the square of degrees of freedom, but actually faster thanks to the sparsity in the system

---
[7]https://www.openmp.org/

matrix. This is expected since the system matrices have their sizes proportional to the square of the total degrees of freedom. For the diffusion problem, we use an iterative solver so that the scaling index is close to 2.0. While for the advection problem, a direct solver is adopted and so the solving time scales almost linearly with respect to the system total degrees of freedom. We also observe that the system initialization and adaptive refinement are computationally at least one magnitude more expensive than the solver, for a problem more complicated than the pure diffusion or advection the difference is larger.
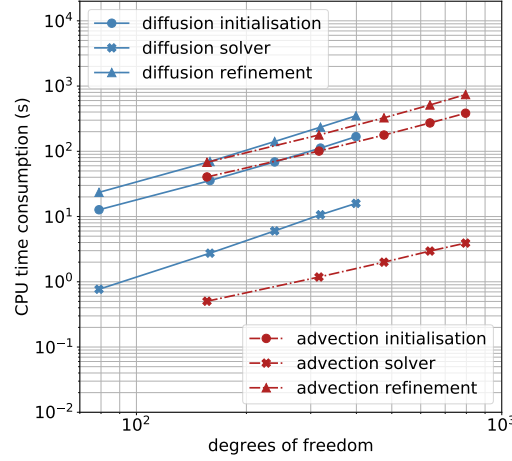
Figure 3.2: CPU time consumption of typical standard `BIFET` routines in serial mode. Iterative solver in diffusion problem results in quadratic scaling, while direct solver in advection problem gives linear scaling. The scaling indices are presented in Tab. 3.1

problem\process	initialization	refinement	solver
diffusion	1.59	1.67	1.88
advection	1.38	1.46	1.26

Table 3.1: The scaling index of CPU time consumption as a power-law function of the degrees of freedom in the discretized problems by FEM displayed in Fig. 3.2.

According to the serial profiling, initialization and adaptive refinement processes are the major optimization targets. With further profiling which is not presented here, we find the most time consuming part in both initialization and refinement processes is the assembling system matrix $\mathcal{M}_{\mathbf{xq}}$ with sufficiently high degrees of freedom. By using `OpenMP`, it is possible to fork the *System* objects among the available CPU working threads, where each thread assembles a certain fraction of $\mathcal{M}_{\mathbf{xq}}$ and $\mathcal{R}_{\mathbf{xq}}$. In addition to distributing *System* access among the threads, the refinement process defined within the *Solution* class is optimized by following the very same idea. By increasing the number of threads, the non-optimized and memory-access-related operations gradually dominate over the paralleled part in the CPU time consumption when the workload for a problem (e.g., calculating the diffusion or advection coefficient at each supporting point) is not heavy enough, in which cases the strong scaling speedups hit the rooftops as illustrated in Fig. 3.3.
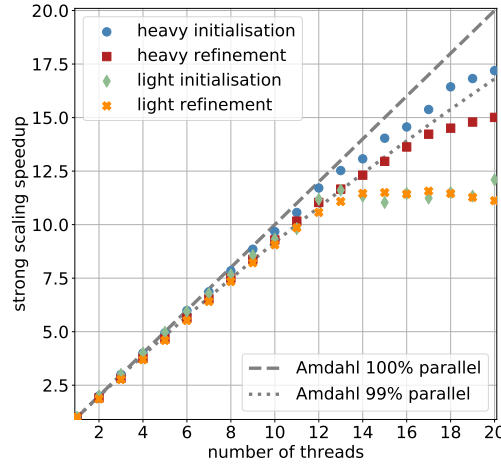
Figure 3.3: Strong scaling speedups of initialization and refinement processes in computationally light and heavy problems. As a benchmark we present Amdahl's law of fully paralleled or 99% paralleled. Rooftops occur in computationally light cases before exploiting the available threads.

Precision

The capability and precision of `BIFET` pipelines in confronting common physical scenarios in CR propagation are illustrated by a series of integrated tests in the following. With an analytically solvable problem, we can compare the numerical solution u_h to the corresponding analytic one u by estimating the L^2 errors at any given testing position $(\mathbf{x}, \mathbf{q})$ in the simulation domain

$$\epsilon_{\mathrm{L}^2,\mathbf{q}} \quad = \quad \sqrt{\int_{\Omega_{\mathbf{x}}} [u(\mathbf{q}) - u_h(\mathbf{q})]^2} \; , \tag{3.26}$$

$$\epsilon_{\mathrm{L}^2,\mathbf{x}} \quad = \quad \sqrt{\int_{\Omega_{\mathbf{q}}} [u(\mathbf{x}) - u_h(\mathbf{x})]^2} \; , \tag{3.27}$$

where for simplicity with built-in library functions provided by `deal.II`, error estimations are calculated in a single sub-domain, e.g., $\epsilon_{L^2,\mathbf{q}}$ is defined as the spatial sub-domain error by interpolating the solution u_h at the given spectral position $\mathbf{q}$.

A pure diffusion or mathematically speaking a parabolic problem, is the simplest testing case we can start with. We prepare a typical strong formulation for the diffusion problem as

$$\partial_t u(\mathbf{x}, \mathbf{q}, t) - \nabla_{\mathbf{x}} \cdot (\mathcal{D}_{\mathbf{xx}} \nabla_{\mathbf{x}} u(\mathbf{x}, \mathbf{q}, t)) = f(\mathbf{x}, \mathbf{q}, t) \; , \tag{3.28}$$

$$u(\mathbf{x}, \mathbf{q}, t) = 0 \; , \quad \mathbf{x} \in \partial\Omega_x \; , \tag{3.29}$$

where a homogeneous strong condition is defined on all boundaries. For the testing purpose, a simple steady-state solution $u(\mathbf{x}, \mathbf{q})$ which satisfies the Dirichlet boundary condition can be pre-defined as

$$u(\mathbf{x}, \mathbf{q}) = S(z)S(x)S(y) \; , \tag{3.30}$$

where for abbreviation $C(i)$ represents $\cos(\frac{(i-i_{min})\pi}{L_i})$ and $S(i)$ for $\sin(\frac{(i-i_{min})\pi}{L_i})$ with $L_i = i_{max} - i_{min}$ defined as the simulation box length in the spatial coordinate $i \in \{x, y, z\}$. Inspired by the testing cases

designed by Kissmann [2014], we set a similar anisotropic spatial diffusion tensor

$$
\mathcal{D}_{\mathbf{xx}} = \begin{pmatrix} \alpha z^2 & 0 & 0 \\ 0 & \beta x^2 & \beta xy \\ 0 & \beta xy & \beta y^2 \end{pmatrix} , \tag{3.31}
$$

where we set $\alpha \neq \beta$ for anisotropy. The weak formulation of this problem has been presented as an example of domain separation earlier. In the $\mathbb{R}^{1+m}$ setting, the right-hand-side source term which can provide uniquely the pre-defined solution reads

$$
f(z) \;\; = \;\; \frac{\pi^2 \alpha z^2}{L_z^2} S(z) - \frac{2\pi \alpha z}{L_z} C(z) \; , \tag{3.32}
$$

while in the $\mathbb{R}^{2+m}$ dimension setting, its expression should be

$$
\begin{aligned}
f(z,x) \;\; = \;\; & f(z)S(x) \\
& + \frac{\pi^2 \beta x^2}{L_x^2} S(z)S(x) - \frac{2\pi \beta x}{L_x} S(z)C(x) \; ,
\end{aligned} \tag{3.33}
$$

and finally in the $\mathbb{R}^{3+m}$ setting, the source term is

$$
\begin{aligned}
f(z,x,y) \;\; = \;\; & f(z,x)S(y) \\
& - \frac{2\pi^2 \beta xy}{L_x L_y} S(z)C(x)C(y) \\
& - \frac{\pi \beta x}{L_x} S(z)C(x)S(y) - \frac{\pi \beta y}{L_y} S(z)S(x)C(y) \\
& + \frac{\pi^2 \beta y^2}{L_y^2} S(z)S(x)S(y) - \frac{2\pi \beta y}{L_y} S(z)S(x)C(y) \; .
\end{aligned} \tag{3.34}
$$

A direct and efficient approach to this problem is to use a time-independent solver with continuous Galerkin method in BIFET. Fig. 3.4 displays the spatial sub-domain L^2 errors estimated with different dimension and refinement settings, where in practice the total volume of the spatial sub-domain is fixed by setting $L_x = L_y = L_z = L$. For a numerical solution u_h found with (dis)continuous Galerkin base functions up to polynomial order p, the corresponding L^2 errors should follow h^{p+1} scaling where h represents the homogeneous numerical cell length in each spatial direction. This means at each global refinement level, the total number of elemental cells is L/h in each spatial direction. On the other hand, solutions found with adaptive refinement scheme do not respect the h^{p+1} scaling law since the elemental cells are refined inhomogeneously. Nevertheless, we still managed to find a roughly linear (but slightly steeper) scaling of L^2 errors in the adaptively refined cases with respect to the minimal (but not all) cell length h.

For testing the time-dependent solving routines, we intend to recover the steady-state solutions by a time-dependent solver with the Crank-Nicolson method. The left panel in Fig. 3.5 illustrates the evolving property of the time-dependent solver with fixed time-step difference d while increasing the total evolving step T/d until the minimal error found by the time-dependent solver is reached asymptotically. Note that the minimal evolving steps required for reaching the steady-state solution depends on the specific dimension and resolution settings of a problem. The convergence property of the time-dependent solver is presented by the right panel, where the total evolving time T is fixed. With different spatial resolution defined by L/h, we marked the saturation point beyond which further time discretization becomes redundant.
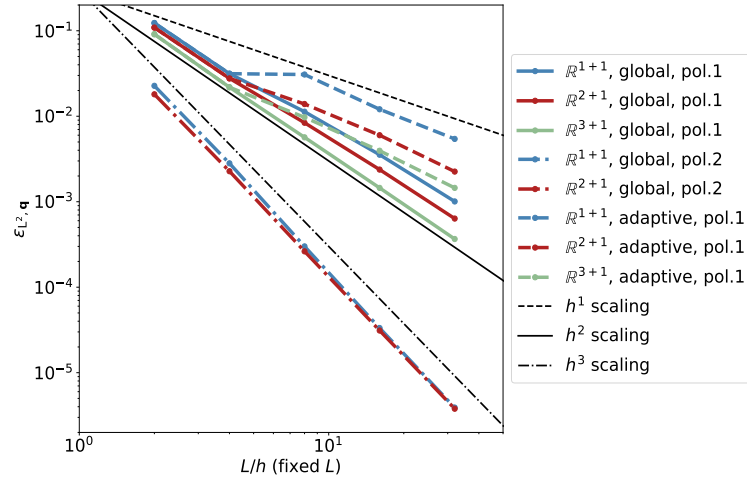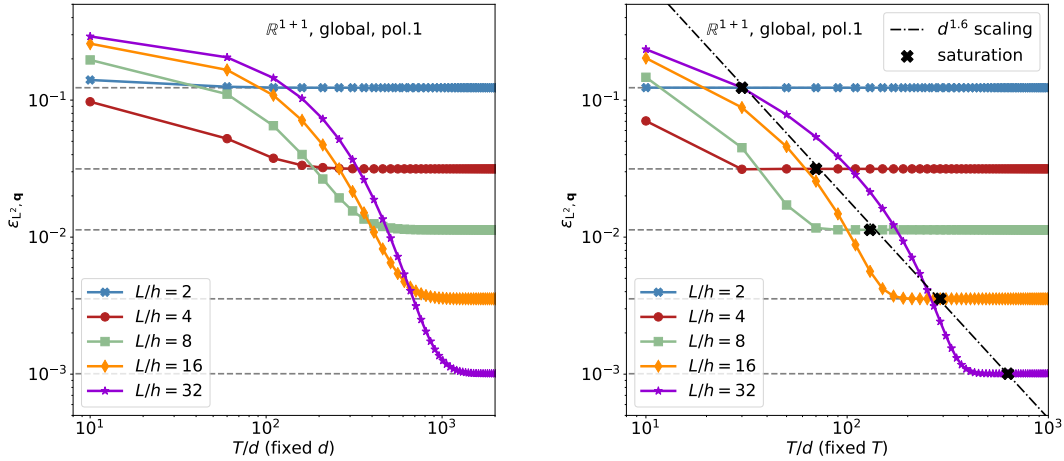
Figure 3.4: Spatial sub-domain L^2 errors measured in solving the spatial diffusion problem with a time-independent solver. "adaptive" indicates the adaptive refinement scheme while "global" indicates the homogeneous global refinement scheme. "pol.ξ" indicates up to the ξ-th order of polynomials are adopted as finite element base functions. Errors estimated with adaptive refinement (adaptive refinement ratio is set as 50%) are plotted according to the same refinement level compared to the globally refined counterparts.

Figure 3.5: Spatial sub-domain L^2 errors measured in solving the spatial diffusion problem with a time-dependent solver. The problem is defined in $\mathbb{R}^{1+1}$ with homogeneously refined mesh and base functions at polynomial order 1. The minimum L^2 errors corresponds to the steady-state solutions are displayed in dashed lines. The saturation positions in the right panel are chosen at where the relative difference between time-dependent and time-independent solutions is below 10^{-6}.

The continuous energy loss (spectral advection) is a typical and important scenario in CR propagation where we can experiment the discontinuous Galerkin method in the spectral sub-domain while keeping the spatial sub-domain safely discretized by the continuous Galerkin method if no spatial advection phenomena shows up. The strong formulation of a simple spectral advection problem is defined as

$$\partial_t u(\mathbf{x}, \mathbf{q}, t) + \nabla_{\mathbf{E}} \cdot (\mathcal{A}_{\mathbf{qq}} u(\mathbf{x}, \mathbf{q}, t)) = f(\mathbf{x}, \mathbf{q}, t) \ , \tag{3.35}$$

$$u(\mathbf{x}, \mathbf{q}, t) = 0 \ , \quad \mathbf{q} \in \partial\Omega_{\mathbf{q}}^+ \ , \tag{3.36}$$

where $\partial_{E_i} = \exp(-q_i)\partial_{q_i}$ since the spectral sub-domain can be built in logarithmic scale. Similar to the previous diffusion problem, the spectral sub-domain coordinates are represented by $\{q_x, q_y, q_z\}$. An anisotropic spectral advection vector $\mathcal{A}$ is assumed to be

$$\mathcal{A}_{\mathbf{qq}} \quad = \quad \begin{pmatrix} \eta_z \exp\left(n_z(q_z - q_{z,min})\right) \\ \eta_x \exp\left(n_x(q_x - q_{x,min})\right) \\ \eta_y \exp\left(n_y(q_y - q_{y,min})\right) \end{pmatrix} \ . \tag{3.37}$$

In the $\mathbb{R}^{m+1}$ setting, with a simple right-hand-side source term $f(q_z) = \exp\left(s_z(q_z - q_{z,min})\right)$, the analytic solution which satisfies the homogeneous strong boundary condition reads

$$\begin{aligned} u(z) \quad &= \quad \frac{\exp\left((n_z - s_z)q_{z,min}\right)}{(1 + s_z)\eta_z} \exp\left(q_z(1 + s_z - n_z)\right) \\ &\quad - \frac{\exp\left((n_z + 1)q_{z,min} + (1 + s_z)L_{q_z}\right)}{(1 + s_z)\eta_z} \exp\left(-n_z q_z\right) \ . \end{aligned} \tag{3.38}$$

For the testing purpose we require $u(\mathbf{x}, \mathbf{q}, t) = u(q_z)u(q_x)u(q_y)$, then in analogy to the $\mathbb{R}^{m+1}$ case the source term for the $\mathbb{R}^{m+3}$ setting reads

$$\begin{aligned} f(q_z, q_x, q_y) \quad &= \quad f(q_z)u(q_x)u(q_y) \\ &\quad + u(q_z)f(q_x)u(q_y) + u(q_z)u(q_x)f(q_y) \ . \end{aligned} \tag{3.39}$$

Note that shifting from the energy coordinate $\mathbf{E}$ derivation to its corresponding logarithmic coordinate $\mathbf{q} = \log(\mathbf{E})$ derivation introduces a diagonal tensor

$$\mathcal{T}_{\mathbf{q}} = \begin{pmatrix} \exp(-q_z) & 0 & 0 \\ 0 & \exp(-q_x) & 0 \\ 0 & 0 & \exp(-q_y) \end{pmatrix} \ , \tag{3.40}$$

which consequently brings itself and $\nabla_{\mathbf{q}}\mathcal{T}_{\mathbf{q}}$ into the weak formulation. Before applying the upwind method and boundary condition, the weak formulation for the advection term reads

$$\begin{aligned} \nabla_{\mathbf{E}} \cdot (\mathcal{A}_{\mathbf{qq}}u) \quad &\to \quad \sum_k \sum_{\beta,j} \mathcal{U}_k^{\beta j} \int_{\Omega_{\mathbf{x}}} \int_{\Omega_{\mathbf{q}}^k} \phi_{\alpha i}^k \mathcal{T}_{\mathbf{q}} \nabla_{\mathbf{q}} \cdot (\mathcal{A}_{\mathbf{qq}} \phi_{\beta j}^k) \\ &= \quad \sum_k \sum_{\beta,j} \mathcal{U}_k^{\beta j} \left[\int_{\Omega_{\mathbf{x}}} \oint_{\partial\Omega_{\mathbf{q}}^k} \phi_{\alpha i}^k \mathcal{T}_{\mathbf{q}} \mathcal{A}_{\mathbf{qq}} \hat{n}_{\mathbf{q}}^k \phi_{\beta j}^k \right. \\ &\quad - \int_{\Omega_{\mathbf{x}}} \int_{\Omega_{\mathbf{q}}^k} (\nabla_{\mathbf{q}} \phi_{\alpha i}^k) \mathcal{T}_{\mathbf{q}} \mathcal{A}_{\mathbf{qq}} \phi_{\beta j}^k \\ &\quad \left. - \int_{\Omega_{\mathbf{x}}} \int_{\Omega_{\mathbf{q}}^k} \phi_{\alpha i}^k (\nabla_{\mathbf{q}} \mathcal{T}_{\mathbf{q}}) \mathcal{A}_{\mathbf{qq}} \phi_{\beta j}^k \right] \ , \end{aligned} \tag{3.41}$$

where base functions are independently defined in each spectral cell $\Omega_{\mathbf{q}}^k$. With the upwind method applied in order to ease the oscillation in the solution of an advection problem, each spectral internal surface integral reads

$$\sum_{\beta,j} \int_{\Omega_{\mathbf{x}}} \oint_{\partial\Omega_{\mathbf{q}}^k} \phi_{\beta j}^- \mathcal{T}_{\mathbf{q}} \mathcal{A}_{\mathbf{qq}} (\phi_{\alpha i}^+ \hat{n}_{\mathbf{q}}^+ + \phi_{\alpha i}^- \hat{n}_{\mathbf{q}}^-) \ , \tag{3.42}$$

with the wind direction (pointing from downwind cell marked by $-$ to upwind cell marked by $+$) defined by $\mathcal{T}_{\mathbf{q}} \mathcal{A}_{\mathbf{qq}}$.

Spectral L^2 error scaling properties of time-independent solver with various dimension and refinement settings are illustrated by Fig. 3.6. The performance of applying a time-dependent solver to the same problem is illustrated in Fig. 3.7.
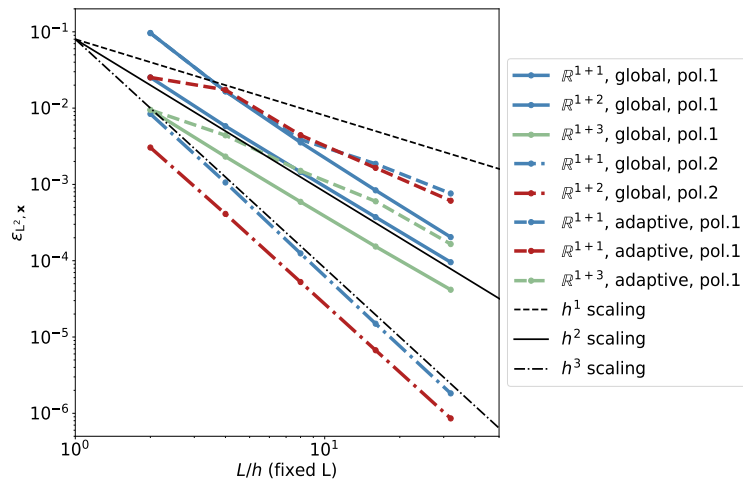
Figure 3.6: Spectral sub-domain L^2 errors measured in solving the spectral advection problem. "adaptive" indicates adaptive refinement scheme while "global" indicates global refinement scheme. "pol.ξ" indicates up to ξ-th order of polynomials are adopted as finite element base functions. Solutions found with adaptive refinement (adaptive refinement ratio is set as 50%) are plotted according to refinement level compared to globally refined counterparts.
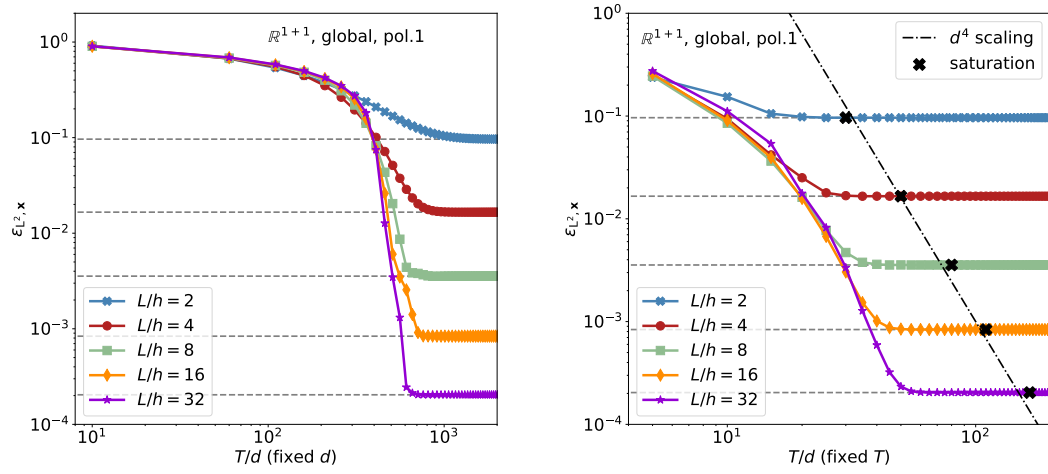
Figure 3.7: Spectral sub-domain L^2 errors measured in solving the spectral advection problem with a time-dependent solver. The problem is defined in $\mathbb{R}^{1+1}$ with homogeneously refined mesh and base functions at polynomial order 1. The minimum L^2 errors corresponds to the steady-state solutions are displayed in dashed lines. The saturation positions in the right panel are chosen at where the relative difference between time-dependent and time-independent solutions is below 10^{-6}.

In the above two testing cases, we have seen the diffusion and advection problems separately. A more realistic problem usually involves both diffusion and advection which need to be solved simultaneously either defined in the same sub-domain or in two sub-domains separately. Here we set up an advection-diffusion problem (with diffusion and advection in the same sub-domain) and approach unconventionally with the continuous Galerkin method as in the pure diffusion problem case and then observe the performance. Despite the fact that discontinuous Galerkin is the standard method for solving an advection-diffusion problem, a continuous Galerkin method however is computationally lighter and easier to be implemented and also interesting to be tested as an alternative approach. The strong formulation of a simple advection-diffusion problem is defined as

$$\partial_t u(\mathbf{x}, \mathbf{q}, t) + \nabla_\mathbf{x} \cdot (\mathcal{A}_{\mathbf{xx}} u(\mathbf{x}, \mathbf{q}, t)) - \nabla_\mathbf{x} \cdot (\mathcal{D}_{\mathbf{xx}} \nabla_\mathbf{x} u(\mathbf{x}, \mathbf{q}, t)) = f(\mathbf{x}, \mathbf{q}, t) \ , \tag{3.43}$$

$$u(\mathbf{x}, \mathbf{q}, t) = 0 \ , \quad \mathbf{x} \in \partial\Omega_\mathbf{x}^+ \ , \tag{3.44}$$

$$\hat{\mathbf{n}}_\mathbf{x} \cdot (\mathcal{A}_{\mathbf{xx}} - \mathcal{D}_{\mathbf{xx}} \nabla_\mathbf{x}) u(\mathbf{x}, \mathbf{q}, t) = 0 \ , \quad \mathbf{x} \in \partial\Omega_\mathbf{x}^- \ , \tag{3.45}$$

where $\partial\Omega^+$ and $\partial\Omega^-$ represent the upper and lower surface bounds respectively. We do not intend to complicate advection or diffusion tensors, and so they are set with constant values

$$\mathcal{A}_{\mathbf{xx}} = \begin{pmatrix} \eta_z \\ \eta_x \\ \eta_y \end{pmatrix} \ , \quad \mathcal{D}_{\mathbf{xx}} = \begin{pmatrix} \alpha & 0 & 0 \\ 0 & \beta & 0 \\ 0 & 0 & \beta \end{pmatrix} \ . \tag{3.46}$$

In the $\mathbb{R}^{1+m}$ setting, with simple time-independent source $f(\mathbf{x}, \mathbf{q}, t) = \exp(z_{min} - z)$ an analytic solution that satisfies our boundary conditions can be derived as

$$u(z) = \left(\frac{\exp(z_{min} - z)}{(\alpha + \eta_z)} - \frac{1}{\eta_z} \right) \exp\left(-\frac{\eta_z(z - z_{max})}{\alpha} \right) - \frac{\exp(z_{min} - z)}{(\alpha + \eta_z)} + \frac{1}{\eta_z} \ . \tag{3.47}$$

In the $\mathbb{R}^{2+m}$ and $\mathbb{R}^{3+m}$ settings we require $u(\mathbf{x}, \mathbf{q}) = u(z)u(x)u(y)$ so that the corresponding source functions reads

$$f(z, x) = f(z)u(x) + u(z)f(x) \ , \tag{3.48}$$

$$f(z, x, y) = f(z, x)u(y) + u(z)u(x)f(y) \ . \tag{3.49}$$

The left-hand-side of the time-independent weak formulation reads

$$\sum_{\beta, j} \mathcal{U}^{\beta j} \int_\Omega (\mathcal{D}_{\mathbf{xx}} \nabla_\mathbf{x} \phi_{\beta j} - \mathcal{A}_{\mathbf{xx}} \phi_{\beta j}) \cdot \nabla_\mathbf{x} \phi_{\alpha i} \ , \tag{3.50}$$

in which the surface integral terms vanish due to the boundary conditions.

Fig. 3.8 illustrates the precision of the time-independent solver in two different cases. In the first case we set diffusion coefficient as the same magnitude as the advection coefficient, while in the second case the diffusion term is significantly weaker than the advection. It is known that continuous Galerkin method is not appropriate for solving a pure advection problem, and so by mixing a diffusion term into the advection problem to suppress artificial oscillation in the solution the continuous Galerkin may become feasible. We should expect that smaller diffusive partition in the advection-diffusion problem requires higher mesh refinement to reach the ideal error scaling law. This is observed in the upper panel of Fig. 3.8 where the

ideal error scaling is only achieved with highly refined grid, while in the lower panel of Fig. 3.8 the ideal error scaling is well followed sicne the diffusion term is significant enough at the given mesh resolution. The performance of applying a time-dependent solver to the advection-diffusion problem is illustrated in Fig. 3.9.
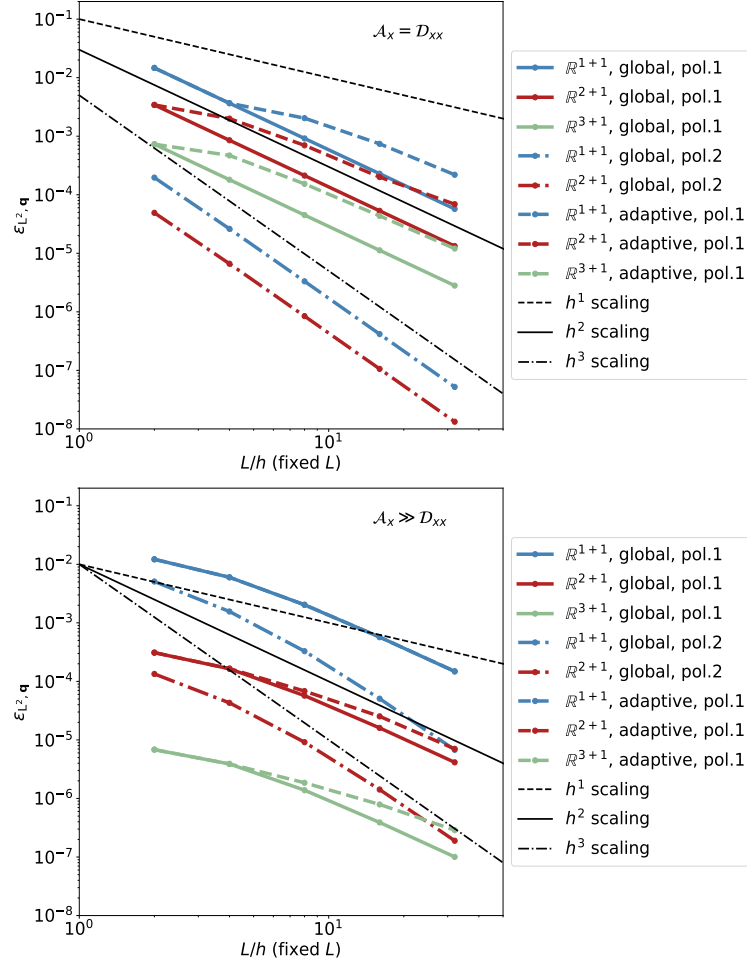

Figure 3.8: Spatial sub-domain L^2 errors measured in solving the advection-diffusion problem. "adaptive" indicates adaptive refinement scheme while "global" indicates global refinement scheme. "pol.ξ" indicates up to ξ-th order of polynomials are adopted as finite element base functions. Solutions found with adaptive refinement (adaptive refinement ratio is set as 50%) are plotted according to refinement level compared to globally refined counterparts.
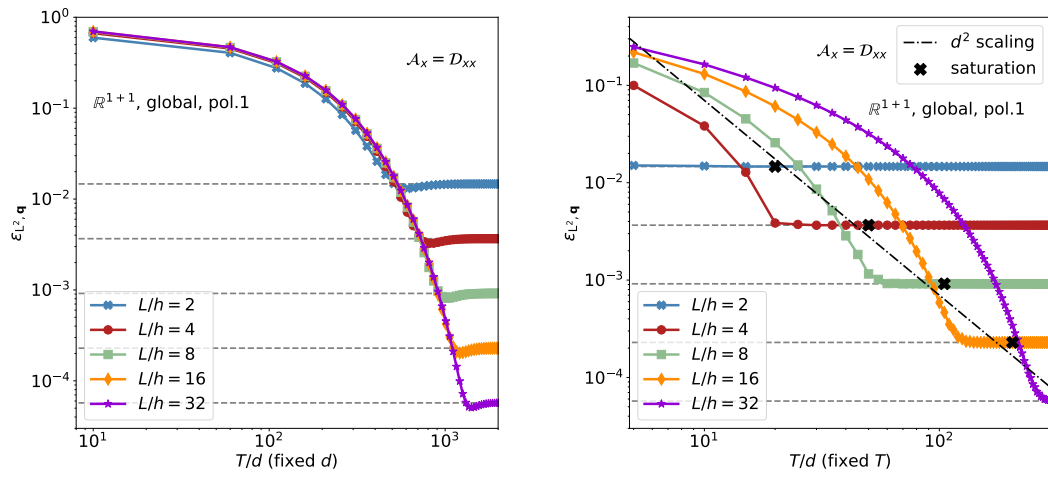
Figure 3.9: Spectral sub-domain L^2 errors measured in solving the advection-diffusion problem with a time-dependent solver. The problem is defined in $\mathbb{R}^{1+1}$ with homogeneously refined mesh and base functions at polynomial order 1. The minimum L^2 errors corresponds to the steady-state solutions are displayed in dashed lines. The saturation positions in the right panel are chosen at where the relative difference between time-dependent and time-independent solutions is below 10^{-6}.

The above tests all focus on problems non-trivially defined in a single sub-domain, from which we have collected some practical experience for more realistic problems which span across the whole domain[8]. Here we define a simple problem with constant and isotropic spatial diffusion and spectral advection as

$$\partial_t u - \nabla_{\mathbf{x}} \cdot (\mathcal{D}_{\mathbf{xx}} \nabla_{\mathbf{x}} u) + \nabla_{\mathbf{E}} \cdot (\mathcal{A}_{\mathbf{qq}} u) = f \ , \tag{3.51}$$

$$u(\mathbf{x}, \mathbf{q}, t) = 0 \ , \quad \mathbf{q} \in \partial\Omega_{\mathbf{q}}^{+} \ , \tag{3.52}$$

$$u(\mathbf{x}, \mathbf{q}, t) = 0 \ , \quad \mathbf{x} \in \partial\Omega_{\mathbf{x}} \ , \tag{3.53}$$

$$\mathcal{A}_{\mathbf{qq}} = \begin{pmatrix} \eta \\ \eta \\ \eta \end{pmatrix} \ , \quad \mathcal{D}_{\mathbf{xx}} = \begin{pmatrix} \alpha & 0 & 0 \\ 0 & \alpha & 0 \\ 0 & 0 & \alpha \end{pmatrix} \ . \tag{3.54}$$

Since the operators (diffusion and advection) are independent, we are able to formulate the solution as $u(\mathbf{x}, \mathbf{q}, t) = u(\mathbf{x}, t)u(\mathbf{q}, t)$ and consequently the right-hand-side source as $f(\mathbf{x}, \mathbf{q}, t) = f_x(\mathbf{x}, t)u_q(\mathbf{q}, t) + f_q(\mathbf{q}, t)u_x(\mathbf{x}, t)$. By learning from the simple forms of solutions in previous tests we fill the system with

$$u_x(\xi) = \sin\left(\frac{(\xi - \xi_{min})\pi}{L_\xi}\right) \ , \tag{3.55}$$

$$u_x(\mathbf{x}) = \prod_\xi u(\xi) \ , \tag{3.56}$$

$$u_q(q_\xi) = \frac{\exp(q_{\xi,\min})}{\eta(1 + s)}\left[\exp\left((1 + s)(q_\xi - q_{\xi,\min})\right) - \exp\left((1 + s)L_{q_\xi}\right) \right] \ , \tag{3.57}$$

$$u_q(\mathbf{q}) = \prod_{q_\xi} u(q_\xi) \ . \tag{3.58}$$

The weak formulation consists of the spatial component from the weak formulation of the spatial diffusion problem and the spectral component from the weak formulation of the spectral advection problem, and so the discontinuous Galerkin method is used only in the spectral domain where the advection is defined. Before applying the upwind method, the time-independent left-hand-side is represented by

$$\sum_k \sum_{\beta,j} \mathcal{U}_k^{\beta j} \int_{\Omega_{\mathbf{x}}} (\nabla_{\mathbf{x}} v_i \mathcal{D}_{\mathbf{xx}} \nabla_{\mathbf{x}} v_j)$$

$$\times \left[\oint_{\partial\Omega_{\mathbf{q}}^k} w_\alpha^k \mathcal{T}_{\mathbf{q}} \mathcal{A}_{\mathbf{qq}} \hat{n}_{\mathbf{q}}^k w_\beta^k - \int_{\Omega_{\mathbf{q}}^k} (\nabla_{\mathbf{q}} w_\alpha^k) \mathcal{T}_{\mathbf{q}} \mathcal{A}_{\mathbf{qq}} w_\beta^k - \int_{\Omega_{\mathbf{q}}^k} w_\alpha^k (\nabla_{\mathbf{q}} \mathcal{T}_{\mathbf{q}}) \mathcal{A}_{\mathbf{qq}} w_\beta^k \right] \ . \tag{3.59}$$

Fig. 3.10 displays the measured spatial and spectral L^2 errors with respect to the simulation mesh resolution. By applying a time-dependent solver, the asymptotic error convergence with fixed time-difference and fixed total evolving time are displayed respectively in Fig. 3.11 (for spatial L^2 errors) and Fig. 3.12 (for spectral L^2 errors).

3.3   application example

Convinced by integrated tests of various typical problems, we move on to illustrate the capacity of `BIFET` in realistic simulations. The examples are designed as one of the commonly adopted simulation settings in previous studies carried out with other simulators like `Galprop` [Strong and Moskalenko, 1998]

---

[8]We emphasize that all problems are defined on the full domain, but when no operation is defined in a sub-domain the corresponding weak formulation is usually a trivial mass matrix.
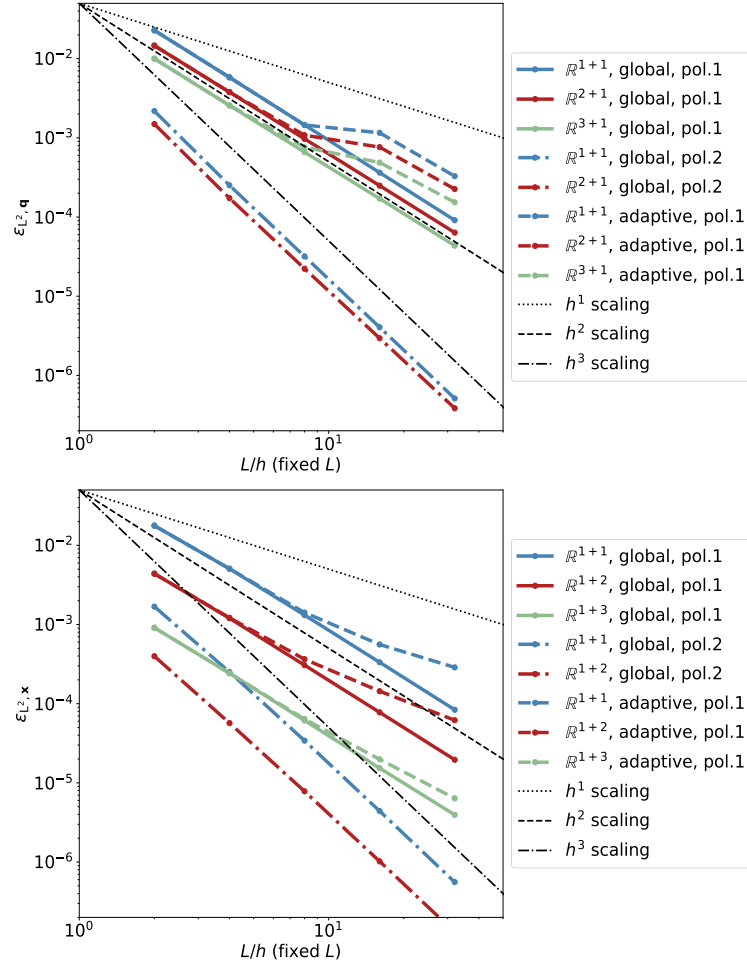
Figure 3.10: Spatial and spectral domain L^2 errors measured in the spatial diffusion with spectral advection problem. "adaptive" indicates adaptive refinement scheme while "global" indicates global refinement scheme. "pol.x" means up to x-th order of polynomials are adopted as finite element base functions. L/h means the number of cells along each spatial dimension. Solutions found with adaptive refinement are placed according to refinement level in comparison with globally refined counterparts. In this illustration we set adaptive refinement ratio as 50%.

and `DRAGON` [Evoli et al., 2017] where GMF is pre-defined and fixed. We consider a CRE propagation problem with time-independent spatial diffusion plus spectral advection in the $\mathbb{R}^{1+1}$ dimension setting. Homogeneously distributed Galactic magnetic field is assumed without requiring CR feedback, which means no CR streaming instability in the magnetic turbulence. In the $\mathbb{R}^{3+3}$ dimension setting, the simplified CRE propagation is defined as

$$\partial_t \tilde{N} - \nabla_{\mathbf{x}} \cdot (\mathcal{D} \nabla_{\mathbf{x}} \tilde{N}) + \nabla_{\mathbf{E}} \cdot (\mathbf{b} \tilde{N}) = Q \ , \tag{3.60}$$

$$\tilde{N}(\mathbf{x}, \mathbf{q}, t) = 0 \ , \quad \mathbf{q} \in \partial \Omega_{\mathbf{q}}^+ \ , \tag{3.61}$$

$$\tilde{N}(\mathbf{x}, \mathbf{q}, t) = 0 \ , \quad \mathbf{x} \in \partial \Omega_{\mathbf{x}} \ , \tag{3.62}$$

where $\tilde{N}(E, r)$ represents spherical symmetric CRE differential density. This toy modelling of CRE propagation can be applied to either point source modelled as some exponential profile in a homogeneous
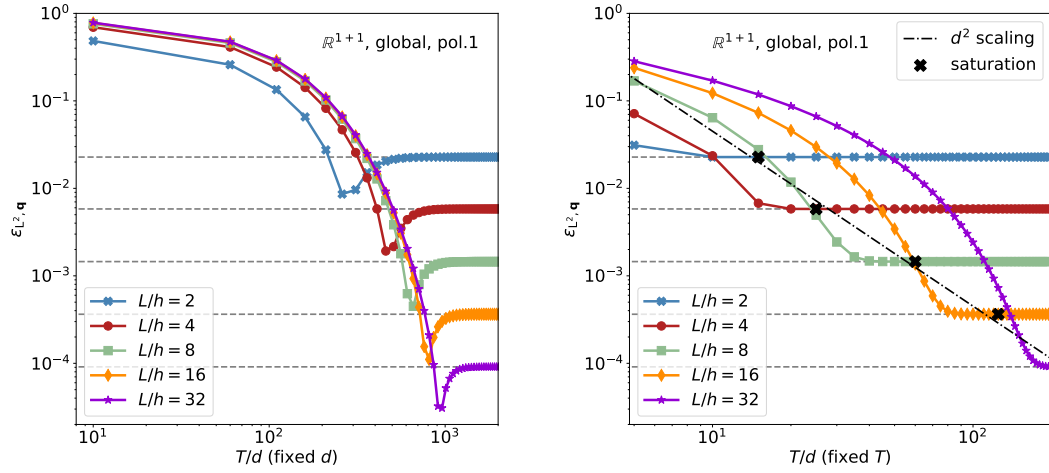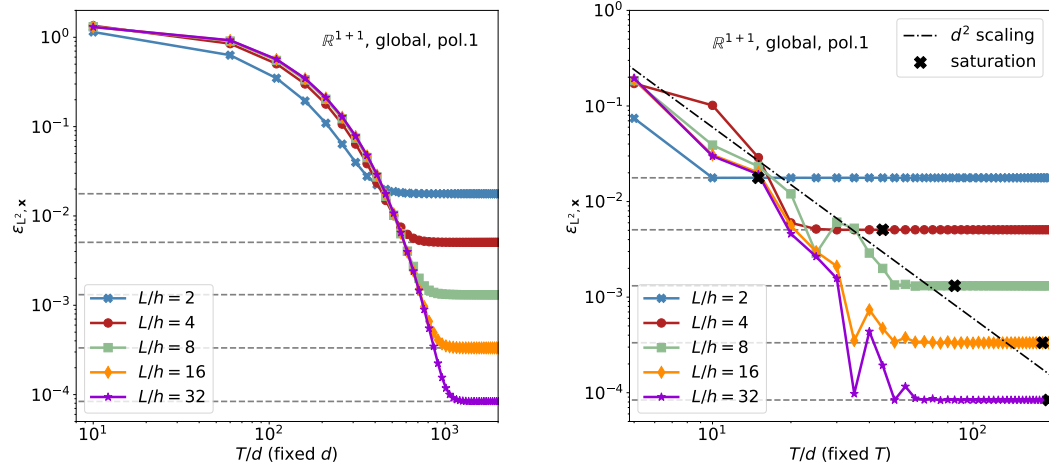
Figure 3.11: Spatial L^2 errors measured in the spatial-diffusion with spectral-advection problem with a time-dependent solver. The testing spatial diffusion problem is defined in $\mathbb{R}^{1+1}$ with homogeneously refined mesh and finite element base functions at polynomial order 1. The minimum L^2 errors corresponds to the steady-state solutions are displayed in dashed lines. The saturation positions in the right panel are chosen at where the relative difference between time-dependent and time-independent solutions is below 10^{-6}.

Figure 3.12: Spectral L^2 errors measured in the spatial-diffusion with spectral-advection problem with a time-dependent solver. The testing spatial diffusion problem is defined in $\mathbb{R}^{1+1}$ with homogeneously refined mesh and finite element base functions at polynomial order 1. The minimum L^2 errors corresponds to the steady-state solutions are displayed in dashed lines. The saturation positions in the right panel are chosen at where the relative difference between time-dependent and time-independent solutions is below 10^{-6}.

diffusive background [Hooper et al., 2009], or extended sources in galaxy clusters [BRUNETTI and JONES, 2014] and dwarf galaxies [Chen et al., 2016]. Reducing to the $\mathbb{R}^{1+1}$ dimension with spherical symmetries, the time-independent propagation equation $\partial_t \tilde{N} = 0$ is reformulated as

$$-\frac{1}{r^2}\partial_r(r^2\mathcal{D}\partial_r\tilde{N}) + \frac{1}{E^2}\partial_E(E^2\mathbf{b}\tilde{N}) = Q , \tag{3.63}$$

$$\partial_r\tilde{N}(r=0) = 0 , \tag{3.64}$$

$$\tilde{N}(r=r_{max}) = 0 , \tag{3.65}$$

$$\tilde{N}(E=E_{max}) = 0 . \tag{3.66}$$

We are interested in CREs reside within the energy range $E \in [10^{-2}, 10^3]$ GeV, where the dominant continuous energy loss mechanisms are Coulomb interactions (neglecting the degree of ionization), non-thermal bremsstrahlung (in strong-shielding limit), inverse Compton scattering and synchrotron emission, which can be approximated mono-chromatically (which means the energy loss rate is approximated as a function of CR energy alone) as

$$-\mathbf{b}(E) = \mathbf{b}_{ic} + \mathbf{b}_{sync} + \mathbf{b}_{coul} + \mathbf{b}_{brem} , \tag{3.67}$$

$$\mathbf{b}_{sync} = \frac{c\sigma_T}{4\pi}(B_0\gamma)^2$$
$$\simeq 4.96 \times 10^{-7}\gamma^2 \text{ GeV/Gyr} , \tag{3.68}$$

$$\mathbf{b}_{ic} = \frac{4}{3}c\sigma_T\omega\gamma^2$$
$$\simeq 2.08 \times 10^{-7}\gamma^2 \text{ GeV/Gyr} , \tag{3.69}$$

$$\mathbf{b}_{coul} = 2.7c\sigma_T n_H m_e c^2(6.85 + \ln\gamma)$$
$$\simeq 0.96\ln\gamma + 6.58 \text{ GeV/Gyr} , \tag{3.70}$$

$$\mathbf{b}_{brem} = \frac{175.5\alpha c\sigma_T}{8\pi}n_H m_e c^2\gamma$$
$$\simeq 0.02\gamma \text{ GeV/Gyr} , \tag{3.71}$$

where c is the light speed, σ_T is the Thomson cross-section, α is the fine structure constant. We assume a typical averaged magnetic field strength $B_0 = 4.0 \ \mu$G, averaged hydrogen density $n_H = 1.14 \text{ cm}^{-3}$, and constant background photon field energy density $w = 0.25 \text{ eV/cm}^3$. Fig. 3.13 presents the CRE energy loss rates as functions of its total energy. Although the energy loss modelling is not very realistic, it catches the basic feature of the dominating mechanisms at different electron energy range. In addition, the toy modelling of an isotropic spatial diffusion coefficient [Evoli et al., 2017] can be defined as

$$\mathcal{D}(E) = D_0(\frac{E/\text{GeV}}{B_0/\mu\text{G}})^{1/3}$$
$$\simeq 3.15 \times 10^{-2}\gamma^{1/3} \text{ kpc}^2/\text{Gyr} , \tag{3.72}$$

where $D_0 = 1.0 \times 10^2 \text{ kpc}^2/\text{Gyr}$. In analogy to the phenomenon where CREs are produced by the supernova explosion, we could roughly describe the source term Q as

$$Q(E,r) = Q_0 g_{snr}(E/\text{GeV})^{-\kappa}$$
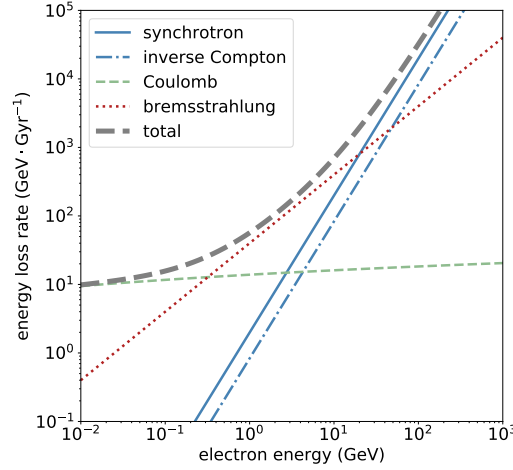$$\simeq 1.99 \times 10^6 \exp(-r/h)\gamma^{-2.2}\text{cm}^{-3}\text{GeV}^{-3}\text{Gyr}^{-1} , \tag{3.73}$$

Figure 3.13: CRE continuous energy loss rate in various mechanisms defined in the toy modelling. At low energy scale Coulomb interaction loss (dashed green curve) dominates until around 0.1 GeV level, from where Bremsstrahlung loss (dotted red curve) takes over. When CRE energy goes higher than 10 GeV magnitude, synchrotron loss (solid blue curve) and inverse Compton loss (dash-dot blue curve) become dominant mechanisms.

with $Q_0 = 1.0$ cm^{-3}GeV^{-3}Gyr^{-1}, $h = 0.5$ kpc, $\kappa = 2.2$, which are chosen for illustrative purpose. Alternatively, we can replace supernova-remnant-driven profile g_{snr} by a WIMP-annihilation-driven profile

$$g_{\mathrm{dm}}^2 = 2.56 \frac{h^6}{(h+r)^2(h^2+r^2)^2} \ , \tag{3.74}$$

which is known the Burkert profile [Burkert, 1996] for dark matter distribution in dwarf galaxies, where the square comes from how we estimate the annihilation cross-section and the constant 2.56 is set in this example for normalizing the total source density with respect to g_{snr}.

Differs from the testing case for spatial diffusion with spectral advection, here we have additional geometric tensors $\mathcal{T}_r = r^{-2}$ and $\mathcal{T}_q = E^{-3}$. The raw (before applying the upwind method) weak formulation of the time-independent left-hand-side consequently has more terms in the spatial domain, which reads

$$\sum_k \sum_{\beta,j} \mathcal{U}_k^{\beta j} \int_{\Omega_r} (v_i v_j) \Bigg[\oint_{\partial\Omega_q^k} w_\alpha (\mathcal{T}_q \tilde{\mathbf{b}}) \cdot \hat{n}_q w_\beta$$
$$- \int_{\Omega_q^k} (\nabla_q w_\alpha^k) \cdot (\mathcal{T}_q \tilde{\mathbf{b}}) w_\beta^k - \int_{\Omega_q^k} w_\alpha^k (\nabla_q \mathcal{T}_q) \cdot \tilde{\mathbf{b}} w_\beta^k \Bigg]$$
$$+ \int_{\Omega_q^k} (w_\alpha^k w_\beta^k) \Bigg[\int_{\Omega_r} (\mathcal{T}_r \nabla_r v_i + v_i \nabla_r \mathcal{T}_r) \cdot (\tilde{\mathcal{D}} \nabla_r v_j) \Bigg] \ , \tag{3.75}$$

where the effective advection coefficient $\tilde{\mathbf{b}} = E^2 \mathbf{b}$, and the effective diffusion coefficient $\tilde{\mathcal{D}} = r^2 \mathcal{D}$.

Fig.3.14 presents the spectral and spatial behaviour of the steady state solutions. The energy spectrum exhibits the expected steepening at around 0.1 GeV due to the transition from diffusion to advection domination and 10 GeV due to the transition of dominant continuous energy loss mechanism illustrated by Fig.3.13. Since the source term Q faces spatial suppression, CRE spectral steepening occurs around

lower energy scale and becomes more smooth at higher radii. Meanwhile, the radial flattening in the dark-matter (DM) induced CRE spectral distribution follows the fact that DM induced modelling provides more CREs at high radii than supernova-remnant (SNR) induced modelling.
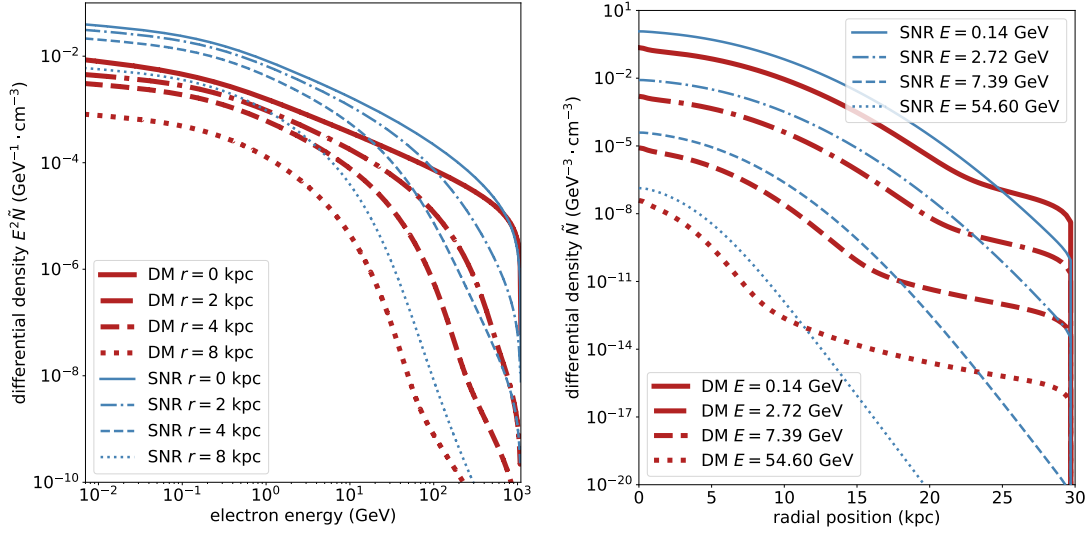

Figure 3.14: Spectral (left) and spatial (right) distribution of CRE differential density $E^2\tilde{N}$ at different radial and energy positions. Thick (red) curves represent results from CRE source distribution in analogy to DM annihilation while thin (blue) curves are from source distribution in analogy to supernova remnants.

3.4 Summary

As demonstrated above, we have successfully built up the framework for handling the high-dimensional PDE system. The multi-threading speedup and precision in solving simple advection-diffusion problems has been examined. We emphasize that this toolkit itself is not fully incomplete from a technical point of view, where we need further MPI parallelism and matrix free method in assembling the system matrix representatives. Towards its application in realistic and complicated CRE propagation, CR-GMF co-evolution and even the RMHD system, we need to implement more auxiliary back-end functions, especially a hyper-propagator class that consists of several single PDE objects. Technically in terms of the solving scheme, we can try to implement the goal-oriented adaptive refinement method [Oden and Prudhomme, 2001], and besides, the non-linear PDE system needs extra caution. In the end we should connect the `BIFET` toolkit into either the `hammurabi X` package or directly into the `IMAGINE` engine in order to realize our conceptual picture of consistent simulation and analysis of the Galactic synchrotron emission.

Chapter 4

Bayesian Analysis

4.1 Overview

Bayesian analysis is a powerful tool that connects the theoretical modeling, numerical simulation and observational data and forms a workflow for verifying and improving our understanding of the physical principles. Although in recent years we have witnessed the thriving of applying neural network and machine learning in scientific studies, Bayesian analysis however, thanks to its explicit mathematical definition in comparing various modellings, is reliable in the applications to which it is competent. In essence, the machine learning belongs to the algorithm modelling category of statistics which is accurate in characterizing the unknown nature without understanding the physical mechanism, while Bayesian analysis belongs to the data modelling that relies on specific description of response functions which bridge signal and data. In CMB foreground removal it is better to use machine learning since we do not need to understand the physical properties of the removed contamination, while for understanding the physics of Galactic component the Bayesian analysis is more efficient in model comparison.

Conventionally with laboratory experiments, we repeat certain physical processes and make statistical descriptions of signals which can be explicitly predicted by theories. However, comparing the simulated Galactic synchrotron emission to the observed Galactic emission maps provided by WMAP [Bennett et al., 2013], Planck [Planck Collaboration et al., 2018b], CPT [Keisler et al., 2011], BICEP and Keck Array [Ade et al., 2015], etc., is different from laboratory experiments because the Galaxy we are living in is as unique as the Universe we observe when study the cosmology. But thanks to the large-scale homogeneity and isotropy, i.e., the Universe is homogeneous roughly beyond 300 Mpc at present and is isotropic with tiny (10^{-5} temperature contrast in CMB) fluctuations, the cosmological observables can provide sufficient statistical descriptions. For constraining physical modellings of the Galactic components, we know that neither homogeneity nor isotropy applies any more and thus have to use the variance imprinted in the stochastic realizations of physical models to complete the statistical information of the Galactic observables.

In the early studies like Sun et al. [2008], Jaffe et al. [2010], Fauvet et al. [2011], only the large angular structures in the observables were considered, with the conventional assumption that turbulent fields do

not contribute to the large angular structures which are mainly determined by the regular fields. Better Bayesian analysis in the pixel domain was latter carried out by Jansson and Farrar [2012a,b] where a very complicated (though still phenomenological) modelling of the Galactic magnetic field distribution was constrained, but the Galactic variance was not considered and so it is unknown whether the results are biased. Some others like Beck et al. [2016], Vansyngel et al. [2018] turned to the angular power spectrum analysis which could give a better description of statistical property of the observables and so are not biased by the Galactic variance. However we need to keep in mind that the power spectrum itself is not sufficient in describing non-Gaussian patterns, and the numerical estimation of angular power spectrum is computationally expensive especially for a sky patch. We have seen that with a given parameter set, `hammurabi X` can make a fast prediction with an ensemble of realizations of the Galactic synchrotron emission. It is feasible to compare the repeatable simulations directly with the unique observation in the pixel domain, where an unconventional likelihood function is necessary.

Based on these motivations the `IMAGINE` consortium [Boulanger et al., 2018] has proposed the numerical tool, `IMAGINE`, along with the ensemble likelihood function for inferring the distribution and configuration of the Galactic components. In the following I will emphasize the likelihood function and its numerical implementation and provide simple testing examples for demonstrating the performance of `IMAGINE`.

4.2 IMAGINE

The `IMAGINE` package assembles pipelines (technically, instances of the *Pipelines* class) which use a variety of measured data sets to constrain parameterized models of the Galactic components. It collects simulated outputs (with the simulators linked to the pipeline) according to the Galactic models and compares those to the measured data sets through likelihood evaluations. External Bayesian sampling libraries are adopted for exploiting the multi-dimensional parameter space in order to provide robust posteriori estimations.

`IMAGINE` uniquely deals with the Galactic (co)variance, i.e., the fact that the Galaxy can be considered as a single and unique instance of the turbulent or random processes it contains while numerical simulations will render different realizations. `IMAGINE` computes observables from a finite set of different realizations of the turbulent fields and uses the mean and variance of the simulated observables to determine the likelihood in comparison to the actually measured data. In this way, the measured Galactic observables can be compared to the (non)-parametric modellings in a way that quantitatively includes the models' expected variations. Here we present detailed technical introductions and explanations to some (but not all) key functions and features implemented in the `IMAGINE` package.

For the record, the `IMAGINE` package was initially developed by Dr. Theo Steininger with his collaborators, where I participated in testing the likelihood functions. I later became in charge of the completion and upgrading of the package and providing technical support for its future development and application. The credit of ensemble Bayesian analysis belongs to the `IMAGINE` consortium.

4.2.1   Underlying Theory

Bayesian Inference

It is straight forward to consider a Galactic component (e.g., magnetic field, thermal electron density and cosmic ray electron density) as a scalar, vector or tensor field distribution with infinite degrees of freedom, by which we mean at any arbitrary position in the spatial domain a physical field possess a unique scalar, vector or tensor representation. In practice we should reduce the degrees of freedom to a finite number either by non-parametric or parametric modellings which approximate the field distribution with a certain level of simplification. The non-parametric modelling is flexible in adjusting its approximation precision (by refining the discretization resolution), but it is consequently expensive in application and it depends heavily on the quality of the measured data. In contrast, parametric modelling is suitable for gaining prominent physical insights with minimal computing cost and is flexible in encountering various types of observables (considering that different observables are sensitive to different physical quantities/features). In current work we focus on the Bayesian analysis with parametric modellings, but the method implemented in the numerical package is generic.

In terms of the Bayesian inference, parameter estimation and model comparison can be described as the following: A given model m that has a set of parameters θ shall be constrained by data d. This means that we are interested in the posterior probability density $P(\theta|d, m)$. Bayesian statistics provides us a quantitative prescription

$$P(\theta|d, m) = \frac{P(d|\theta, m)P(\theta|m)}{P(d|m)} \; , \tag{4.1}$$

where $P(d|\theta, m)$ is the likelihood of the data, $P(\theta|m)$ is the parameter prior, and $P(d|m)$ is the model's evidence. The latter guarantees the posterior's normalization and is given by

$$\mathcal{Z} = P(d|m) = \int_{\Omega_\theta} P(d|\theta, m)P(\theta|m)\mathrm{d}\theta \; , \tag{4.2}$$

where Ω_θ represents the parameter space/domain. In the nested sampling, the default sampling method in `IMAGINE` (with the `MultiNest` library), the parameter likelihood distribution is estimated by maximizing the evidence $\mathcal{Z}$, and so for comparing different models, e.g., m_1 and m_2, we can calculate the Bayes factor R_{bayes} as

$$R_{\mathrm{bayes}} = \frac{P(m_1|d)}{P(m_2|d)} = \frac{P(d|m_1)P(m_1)}{P(d|m_2)P(m_2)} = \frac{\mathcal{Z}_1 P(m_1)}{\mathcal{Z}_2 P(m_2)} \; . \tag{4.3}$$

Often there is no strong motivation for preferring one model over another which corresponds to setting the model prior ratio $P(m_1)/P(m_2)$ to unity. In this case, the model's evidence is the only source of information for model selection.

Galactic Variance

The likelihood $P(d|\theta, m)$ describes the probability to measure the data d if the reality was given by θ and m. By modeling the physical system this probability can be explicitly calculated for certain sets (θ, m). For this, one uses a forward simulation tool to compute observables like the Faraday rotation measure, synchrotron emission, and thermal dust emission. Given the measured data, by modeling the noise characteristics of the detector, a probability can be assigned to each simulated observable, which is

in principle a standard approach. However, when analyzing parametric models of random (or stochastic) fields one must be careful at this step because the random components are not analytically defined in the spatial domain. Generally speaking, parametric models specify the large scale structure of the Galactic field explicitly by parameterizing the geometry of its components, e.g., the Galactic disk and possibly its arms, halo, X-shaped components, and the field strength therein. In contrast, random components are modeled in terms of their statistical properties rather than explicit realizations. This means for a given parameter set θ, each realization is distinct from the others in the spatial domain while following the same random statistics, e.g., a certain power spectrum or/and a certain degree of anisotropy. As a consequence, the set (θ, m) corresponds not only to one, but rather an ensemble with infinitely many possible field realizations. For the calculation of a likelihood the measured observables must be compared with the ensemble average, which in practice is the simulated mean of a yet finite set of observable realizations that result from the corresponding field realizations. One may analytically work out the influence of various types of random fields on the observables with certain approximations and simplifications. However, to do a proper uncertainty quantification one must not neglect the so-called Galactic variance introduced by Jaffe et al. [2013], which becomes critical when the strength of a random field component dominates over that of the regular counterpart. This variance measures how strong the influence of a random field on each individual pixel of an observable sky-map is. Regions where the influence is high, that is where the observable variance is high, must be down-weighted upon comparing to the measured data, in contrast to regions where the randomness of the stochastic fields has little influence on the observable fluctuations. This makes it necessary to calculate instances of (θ, m) to be able to construct an estimate for the Galactic variance.

Ensemble Likelihood

The likelihood is the probability $P(d|\theta, m)$ to obtain the data d from a measurement under the assumption that reality is given by the model m that in turn is configured by the parameters θ. It is the key element to rate the probability of a stochastic sample. Assuming the generic case of a measurement with linear response function R of a signal s which involves additive noise n, the corresponding equation for the data d reads

$$d = R(s) + n \ . \tag{4.4}$$

If the measurement device is assumed to exhibit Gaussian noise characteristics with a covariance matrix C, i.e.

$$\mathcal{G}(n, C) \equiv \frac{1}{\sqrt{2\pi C}} \exp\left(-\frac{1}{2} n^\dagger C^{-1} n\right) \ , \tag{4.5}$$

the log-likelihood for a simulated signal that is the result of the evaluation of a model m with parameters θ, i.e. $s' = m(\theta)$, to have produced the measured data d is

$$\mathcal{L}(d|s') = -\frac{1}{2} \left(d - R(s')\right)^T C^{-1} \left(d - R(s')\right) - \frac{1}{2} \ln\left(|C|\right) \ . \tag{4.6}$$

In the context of `IMAGINE` the random/turbulent field models posses random components that are described by (m, θ) only stochastically. Marginalizing over those random degrees of freedom results in a

modification of the effective covariance term in Eq. 4.6, namely that the Galactic variance must be added to the data noise covariance. For the further discussion we consider the following quantities:

- The individual field samples within an ensemble of size N_{ens} are named s^i, with $i \in [1, N_{\mathrm{ens}}]$.

- The process of creating observables from s^i is encoded in the response R, e.g., simulating the Galactic synchrotron emission with `hammurabi X`.

- The simulated observables are denoted by $f^i = R(s^i)$.

- The measured observational data is named d.

Denoting furthermore the data's noise covariance by C_{obs}, the Galactic covariance by C_{sim} the log-likelihood reads

$$\mathcal{L}(d|f) = -\frac{1}{2}(d - \bar{f})^T (C_{\mathrm{obs}} + C_{\mathrm{sim}})^{-1}(d - \bar{f}) - \frac{1}{2}\ln\left(|C_{\mathrm{obs}} + C_{\mathrm{sim}}|\right) \;, \tag{4.7}$$

with the ensemble mean

$$\bar{f} = \frac{1}{N_{\mathrm{ens}}} \sum_{i=1}^{N_{\mathrm{ens}}} f^i \;. \tag{4.8}$$

The Galactic covariance C_{sim} reflects the fact that the observables posses an intrinsic variance because of the random/turbulent fields. For example, the higher the intrinsic variance, the more the likelihood will be flattened by the $(C_{\mathrm{obs}} + C_{\mathrm{sim}})^{-1}$ term. This means that the likelihood is less responsive to deviations from the ensemble mean for regions of high variance. Hence, there is the risk of overestimating random field contributions, since they are favored by the likelihood. However, this is compensated by the second term in Eq. 4.7, i.e., the covariance log-determinant $\ln\left(|C_{\mathrm{obs}} + C_{\mathrm{sim}}|\right)$.

The Galactic covariance C_{sim} is not known from pure observation, hence, we must estimate it from the ensemble of simulated results. Note that in this way the Galactic covariance is model dependent and the goodness of modelling is known from the Bayesian evidence. A classic approach for C_{sim} is to evaluate the dyadic product of the sample deviations from their mean:

$$\hat{S} = \frac{u^T u}{N_{\mathrm{ens}}} \;, \tag{4.9}$$

with

$$u^i = \left(f^i - \bar{f}\right) \tag{4.10}$$

as a row of the ensemble matrix u. Since the number of realizations in an ensemble is often much smaller than the number of dimensions (limited by the available computing resource) this classical covariance estimator is inaccurate. A more robust approach is to use a sophisticated estimator with a shrinkage target (e.g., a diagonal matrix) and a shrinkage factor. Here we adopt the Oracle Approximating Shrinkage (OAS) estimator introduced by Chen et al. [2011] where the estimator $\hat{\Sigma}$ for inevitable covariance is expressed as

$$\hat{\Sigma} = (1 - \rho)\hat{S} + \rho \frac{Tr(\hat{S})}{p} I \;, \tag{4.11}$$

where I represents the identity matrix. The shrinkage factor ρ is estimated by

$$\rho = \min \left[\frac{(1 - 2/N_{\mathrm{dim}})Tr(\hat{S}^2) + Tr^2(\hat{S})}{(N_{\mathrm{ens}} + 1 - 2/N_{\mathrm{dim}})(Tr(\hat{S}^2) - Tr^2(\hat{S})/N_{\mathrm{dim}})}, 1 \right] \ , \tag{4.12}$$

where the dimension (or the data size) of each observable realization is N_{dim} However, the OAS estimator has been designed for approximating covariance matrices in terms of quadratic forms, using it for determinant estimation yields rather poor results. For the time being we approximate the determinant $|C_{\mathrm{obs}} + C_{\mathrm{sim}}|$ by its trace:

$$\ln\left(|C_{\mathrm{obs}} + C_{\mathrm{sim}}|\right) \approx \ln\left(\mathrm{Tr}(C_{\mathrm{obs}} + \hat{\Sigma})\right) \ . \tag{4.13}$$

In practice we find this approximation serves the purpose of regularizing the random magnetic field strength. In the future upgrade of estimating the log-determinant we will consider the stochastic Chebyshev expansions introduced by Han et al. [2015].

4.2.2   Software Design

The `IMAGINE` package consists of three major logical components, which are the observable, simulator and Bayesian sampler. All the functions and features are designed for smoothly and conveniently bridging these three components into an integrated pipeline. Given a set of observational data with various types and sizes and even masks, `IMAGINE` is designed to categorize (e.g., by knowing the observational frequency) and distribute (e.g., rearrange data-sets under `IMAGINE` convention and/or distribute across computing nodes) the data and pass essential information to the simulator. The simulator is a highly customized part, where we define a few interfacing protocols related to physical field parameter parsing and observable handling. In general, a simulator should be able to produce ensembles of observables corresponding to the given input data. The Bayesian sampler is in charge of evaluating the likelihood function based on the given input data and simulated outputs at each sampling step it take in the allowed parameter space. The pipeline exchanges information between the Bayesian sampler and the simulator, so that once a temporary parameter set is sampled the simulator can reproduce the corresponding ensembles of observables and send them back to the Bayesian sampler for the next round of likelihood evaluation. In the following we introduce the main features and functions implemented around these logical components. The basic workflow is illustrated in Fig. 4.1, where the blue arrows represent the connection of modules and the red lines represent the actual connections among data, priors, variables, parameters and simulated outputs in the iteration of sampling process, the green blocks indicates the default external supporting libraries.
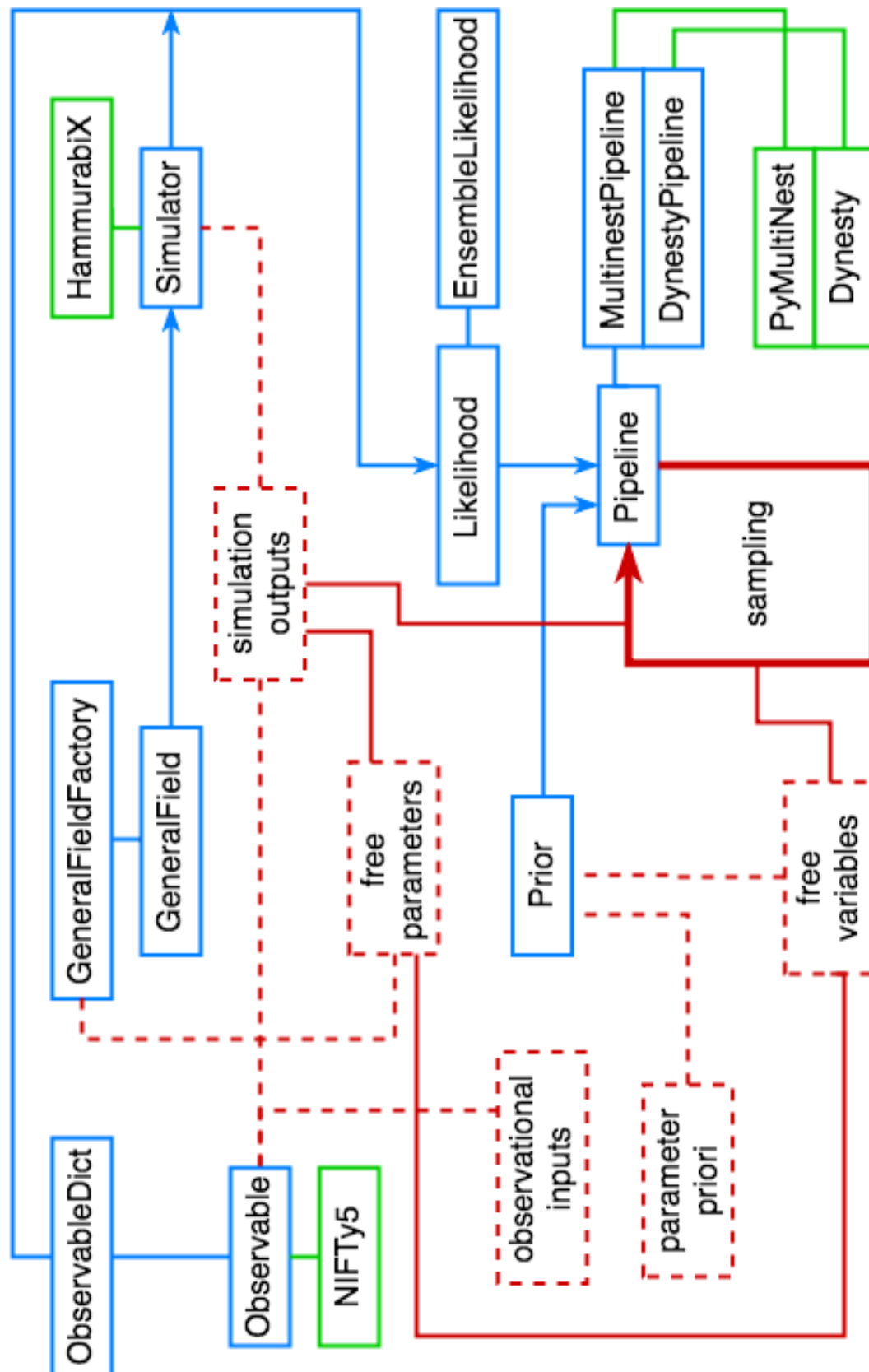
Figure 4.1: IMAGINE workflow.

Observables

Input data-sets, simulated outputs, mask maps and covariance matrices are all handled by the *ObservableDict* class in `IMAGINE`, due to the fact that all these quantities can be treated technically as arrays. In practice, each type of these quantities are used differently and so under the *ObservableDict* class we further define *Measurements*, *Simulations*, *Masks* and *Covariances* sub-classes. The universal feature in the *ObservableDict* class is that the fundamental data structure is the `Python` dictionary. And the elemental data structure under each dictionary entry is defined by the `NIFTy` library, which in essence distributes data into `Python` arrays and applies special structures on them. Note that the `NIFTy` library has built-in MPI support, and so it provides convenient functions for `IMAGINE` to distribute the likelihood computation and observable simulation.

The dictionary entries are defined universally in *ObservableDict* as `Python` tuples. The elements in each entry are observable name, observational frequency, observable size or `HEALPix` N_{side}, and finally the extra tag. It is straight forward to understand the first two entry elements, while the third element is made flexible for accommodating either plain arrays (e.g., masked sky maps or non-map data-sets) or `HEALPix` (full-sky) maps. The reason for treating masked sky maps separately from full-sky `HEALPix` maps is for saving memory for corresponding covariance matrices. The extra tag is designed mainly for dealing with polarized emission maps which have Stokes I, Q and U components. It is also convenient to have this extra tag entry in case like marking data sets in some special applications.

The major difference between *Measurements* and *Simulations* is the fundamental array shape allowed to possess. `IMAGINE` by default treats measurements (in other words, the measured data sets) as single realization ensembles logically, while the simulated outputs are taken as multiple realization ensembles. Note that the *Covariances* is fortunately independent of this "measured" and "simulated" definition. A covariance matrix can be either from the external input along with measured data sets, or from the internal calculation of the Galactic variance. The very same idea applies to the *Masks* sub-class as well, it hosts mask maps/arrays from the external input and applies the masking operation to both the measured data sets and the simulated outputs. The numerical operations like evaluating the Galactic variance and applying masking information are all supported by MPI parallelism.

We store observables in a `Python` dictionary (as the basic data structure in the *ObservableDict* class and its derived classes) so that each data-set can be identified by a unique key (or entry in the non-`Python` language). Each elemental content [1] of the dictionary in an instance of *ObservableDict* should be tagged with the following information:

```
1  ('name',
2   'observed frequency in GHz',
3   'size or HEALPix Nside',
4   'extra tag')
```

---

[1] The elemental content is defined in the *Observable* class designed with back-end support from `NIFTy` library, by which we mean a well defined data structure that contains information of the corresponding observables, i.e., a `HEALPix` array of the full-sky polarized synchrotron emission Stokes Q observed at 30 GHz with resolution $N_{\mathrm{side}} = 1024$.

Instead of contracting these separate pieces of information into a single key string, we define a tuple of strings as the form of the dictionary key so that they can be handled in a flexible way in practice. If any of these tags is redundant, it can be filled with string $'$nan$'$ by default. Now we introduce some conventions we set up for these tags:

The first tag, $'$name$'$, represents observable type, where we set default names and physical units for the commonly used observables as follows:

- $'$fd$'$ for the Faraday depth (in unit rad/m^2)

- $'$dm$'$ for the dispersion measure (in unit pc/cm^3)

- $'$sync$'$ for the synchrotron emission (units depend on the $'$extra tag$'$)

The second tag, $'$observed frequency in GHz$'$, specifies the observational frequency. It can be redundant for some observables like the Faraday depth or dispersion measure, in which case it can be set as $'$nan$'$. The value of this tag (the string will be translated to a floating point number) is always read in unit GHz.

The third tag, $'$size or HEALPix Nside$'$, stores either a `HEALPix` N_{side} value [2] or just the plan data size (or data dimension). This means that to store a plain data set one should use the data size as this key, while the N_{side} value must be used for storing `HEALPix` maps. The reason for distinguishing plain data-sets from `HEALPix` maps is that in `HEALPix` maps are the most commonly used data form and defined on the spherical coordinate.

The last tag, $'$extra tag$'$, commonly applies to diffuse polarized emission components. It however can be set as any string but by default we recommend $'$nan$'$ in order to avoid un-necessary troubles since at certain points in the `IMAGINE` workflow all the tags will be checked or compared automatically. Take the polarized Galactic synchrotron emission as an example, the tag convention is:

- $'$I$'$ for the total intensity (in unit K-cmb)

- $'$Q$'$ for Stokes Q (in unit K-cmb, IAU convention)

- $'$U$'$ for Stokes U (in unit K-cmb, IAU convention)

- $'$PI$'$ for polarization intensity (in unit K-cmb)

- $'$PA$'$ for polarization angle (in unit rad, IAU convention)

The most important method implemented in *ObservableDict* is the *append* function, for which the first input argument is the key tuple described above, and the second input argument can be either a `Numpy` *ndarray* or `NIFTy` *Field* object or an `IMAGINE` *Observable* object (the *Observable* class is internally defined and so not for users). Additionally, we require the 1D *ndarray* being not in the `Numpy` vector shape $(n,)$ but in $(1, n)$. The last argument is optional, which by default is *False* which indicates the input data is a `HEALPix` map, otherwise is a plain data without any special geometry.

In the following we present some application examples related to the *Measurements* and *Simulations* classes.

---

[2] A `HEALPix` map size is known as $12N_{\text{side}}^2$.

```python
1   '''
2   Examples of initializing empty Measurements instance
3   and appending new data under a certain key.
4   '''
5
6   # create an empty Measurements object
7   measure_dict = imagine.Measurements()
8
9   # append a HEALPix map
10  data = np.random.rand(3, 48)
11  measure_dict.append(('test', 'nan', '2', 'nan'), data)
12
13  # append a plain data-set
14  data = np.random.rand(1, 3)
15  measure_dict.append(('test', 'nan', '3', 'nan'), data, True)
16
17  '''
18  A typical usage of the append function is pushing simulations
19  realizations in to the Simulations object.
20  The major difference between the data structure in Measurements
21  and that in Simulations is that, under a given key, a Simulations
22  object allows multiple data appending, which is considered as
23  extending the ensemble size of the corresponding observable.
24
25  What follows is the call function of the hammurabi interfacing module,
26  as an practical example of using the append function in the Simulations
27  class
28  '''
29
30  def __call__(self,
31               field_list):
32      """
33      run hammurabi executable
34      pack up outputs in IMAGINE convention
35
36      Parameters
37      ----------
38      field_list: list of tuple
```

```
39          a list/tuple of GeneralField objects

40

41      Return

42      ------

43      object of Simulations class

44          a dictionary filled with simulated maps

45          hosts a certain number of simulation realizations

46          under each dictionary key

47      """

48

49      self.register_fields(field_list)  # register field info

50      sims = Simulations()  # execute hammurabi ensemble

51      for i in range(self._ensemble_size):

52          self.update_fields(field_list, i)  # update parameters

53          self._ham()  # execute hammurabi

54          for key in self._output_checklist:  # pack up outputs

55              sims.append(key, np.vstack([self._ham.sim_map[key]]))

56      return sims
```

A *Masks* object can be applied to objects of all other derived classes of *ObservableDict*, e.g., to simulated output or observational data, and also to covariance matrix. By convention, a mask map or mask array should be only a single array filled with binary value, i.e., either *True* or *False*, where *False* means that the corresponding pixel or data point in the raw data must be masked out. For matching a mask map to its targets, the masking function, *apply_mask*, conducts masking operation to each target with the same dictionary key as the mask map. Notice that a mask map applies to each target only once, and the ′size or Nside′ tag in the key of the masked target will be automatically updated so the mask can not be re-applied due to the mismatch in their keys. With practical snippets we further illustrate how the masking processes work in IMAGINE.

```
1   '''

2   Simple example of applying mask map,

3   where we assume the data variable contains the target

4   observables or covariance matrices

5   '''

6

7   mask = Masks()

8   mask.append(('test', 'nan', str(size), 'nan'), mask_values, plain=True)

9   # After the apply_mask function,

10  # the key ('test', 'nan', str(size), 'nan') will be changed into
```

```
11    # ('test', 'nan', str(size_of_masked_map), 'nan') automatically.

12    data.apply_mask(mask)
```

Fields and Factories

In the `IMAGINE` terminology, "fields" refers to any Galactic physical component such as the GMF, the thermal electron distribution, the CR distribution, etc. (because both vector and scalar fields are handled within the underlying `NIFTy` library). The base classes for handling such fields are called *GeneralField* and *GeneralFieldFactory* [3].

An `IMAGINE` *GeneralField* object can be read by simulators, which can use the information hosted by the object to simulate the corresponding physical component. A *GeneralField* object possesses a set of parameters, e.g., a GMF field object may host parameter values for pitch angles, scale radii and amplitudes, etc..

In contrast, the *GeneralFieldFactory* is designed as an intermediate layer of the infrastructure used by the Bayesian samplers to provide the connection between the sampling of points in the parameter space and the *GeneralField* object for triggering simulators. A *GeneralFieldFactory* object has a list of the full parameter set for the corresponding field, in addition to a list of controlling parameters specialized for the simulators in collaboration. *GeneralFieldFactory* also defines the allowed value ranges as well as default values for the parameters that either will or will not be explored by the Bayesian sampler.

At each sampling step, an `IMAGINE` pipeline asks *GeneralFieldFactory* objects for the next position in the parameter space and later receives a list of *GeneralField* objects that can be handed to the simulators in collaboration, which in turn provides simulated observables for comparison with the measured data. Technically, *GeneralField* objects do nothing more than informing the simulators (e.g., `hammurabi X` by default) of the updated parameter values. The reason for separately defining factories and fields is to easily enable future usages of other field implementations.

simulators

The default simulator is `hammurabi X` which has been introduced in Chap. 2. The simulator module is flexible for accommodating different and even multiple simulators as long as the interfacing module is consistent with the rest part of `IMAGINE` package. Generally speaking, `IMAGINE` package does not contain a built-in simulator but use pre-built/installed simulator library. Take `hammurabi X` for example, `IMAGINE` possess a copy of the `Python` wrapper of `hammurabi X` and based on the design of the wrapper we write an interfacing module which translates between the `IMAGINE` data and parameter convention and that in `hammurabi X`. The design is convenient for maintaining and upgrading either `IMAGINE` itself or catching up with updates in the simulators.

The other key feature in the simulator interfacing module is that since the sampler will call for new sets of simulated outputs at each sampling step, the simulation kernel will be either executed multiple times or required for producing multiple observables in a single execution. The detailed solution depends

---

[3]We use 'General' to avoid confusion with the *Field* class of the `NIFTy`library.

on specific design of a simulator and/or its `Python` wrapper.

Technically, the MPI support we built-in `IMAGINE` *Pipelines* requires that each computing node works on its own observable realizations and not communicating with other working nodes. The likelihood function evaluation is carried out collectively at the master node only. This means that any simulator in collaboration should at least have a multi-threading solution.

Likelihoods

The *Likelihoods* class and its derived classes define how to quantitatively compare the simulated and measured observables. The ensemble likelihood function discussed above is implemented in *EnsembleLikelihood* where covariance matrices from measurements are combined with the expected galactic variance from models that include stochastic components.

Likelihoods objects have to be initialized at least with measured data (measured covariance matrices and mask maps as optional input arguments) before executing the pipeline in which the likelihood functions are calculated. The optional input argument, object of *Covariances*, is not required to contain covariance matrices for all measured data. The Likelihood function is flexible for cases where part or all of the measured covariance matrices are not available. If the *EnsembleLikelihood* is used, then at each sampling position in the parameter space, an ensembles of simulated data for each type of observable is generated, so the Galactic variance of these observables can then be included in the likelihood calculation quantitatively. In order to present how to use *Likelihoods*, we display the definition of its *init* and *call* functions.

```python
1   '''
2   The first few lines of the init and call functions of Likelihoods
3   '''
4
5   def __init__(self,
6               measurement_dict,
7               covariance_dict=None,
8               mask_dict=None):
9           '''
10          Arguments
11          ---------
12          measurement_dict: Measurements object
13          covariance_dict: Covariances object
14          mask_dict: Masks object
15          '''
16
17  def __call__(self,
18              observable_dict):
```

```
19          '''
20          Arguments
21          ---------
22          observable_dict: Simulations object
23
24          Return
25          ------
26          log-likelihood value
27          '''
28          assert isinstance(observable_dict, Simulations)
29          # check dict entries
30          assert (observable_dict.keys() ==
31                  self._measurement_dict.keys())
```

Bayesian samplers

IMAGINE makes use of external nested sampling libraries, MultiNest [Feroz et al., 2009], which is written in FORTRAN with MPI support. Nested sampling is a Monte Carlo method developed by Skilling [2006], that is capable of directly estimating the relation between the likelihood function and the prior mass. It is unique in the fact that nested sampling is specifically made for usage in Bayesian problems, giving the evidence as its primary result instead of the posterior probability. The major benefits from nested sampling are: First, it reduces calculations from multi-dimensional parameter/variable domain into the one-dimensional prior domain, which makes it easier for handling models with huge number of parameters. Secondly, it calculates evidence directly and is efficient in avoiding local minimums which often trap the conventional Markov chains. Nested sampling works with a set of live points. In each sampling step, the point that has the lowest likelihood value gets replaced by a new one with a higher likelihood value. As this method progresses, the new points sample a smaller and smaller prior volume. The algorithm thus traverses through nested shells of the likelihood.

pipelines

IMAGINE pipelines are defined within the *Pipelines* class. The design of pipelines focus only on the single requirement, that is in each sampling step before evaluating the likelihood function, the pipeline has to spawn a finite number of processes for simulating observables with the same temporary parameter/variable set. Technical efforts are devoted to making fast simulations and execution of the sampler simultaneously.

The current MPI solution provided in IMAGINE (with the MultiNest library) is to pause before likelihood evaluation in the sampler and use the computing notes to simulate observable ensembles in parallel, then the the likelihood calculations are conducted in the master node followed up by scattering the results to each computing node accordingly (since each node is executing a portion of the parameter/variable

domain).

MPI support

ObservableDict has MPI support inherited from the `NIFTy` library, and corresponding changes in data distribution are listed as follows:

- *Measurements*: function *append* in the MPI mode reads a single realization of data (non-distributed) with each key, users have to ensure the data is universally defined on all nodes.

- *Covariances*: function *append* in the MPI mode reads either distributed data, or non-distributed according to the input shape. If reading non-distributed covariance matrix, users have to ensure the data is universally defined on all nodes.

- *Simulations*: function *append* in the MPI mode reads distributed data, where each node is considered as hosting a certain number of realizations of the ensemble of simulated observables.

- *Masks*: function *append* in the MPI mode reads non-distributed data, but then broadcasts each mask map to all computing nodes. This is designed for the convenience in masking process.

The *MultinestPipeline* inherits MPI support from the `MultiNest` library. At each sampling step, different computing nodes pick up different variable (corresponds to free parameters which users want to explore) positions and communicate after the log-likelihoods being evaluated. `IMAGINE` do not interfere with the parallelism inside the `MultiNest`, instead, in each sampling step *MultinestPipeline* caches the variable positions on each node first, then generates ensembles of observable realizations in parallel, and finally returns the evaluated log-likelihood value to each node. At the front end, users should only know that by executing `IMAGINE` routine in the MPI mode, the true ensemble size for each sampling step and each observable is defined as *ensemble_size* parameter multiplied by the number of MPI nodes.

4.2.3 Precision and Performance

`IMAGINE` is designed, and so expected, to recognize correctly the random field contributions to the observables, especially when it is much larger than that of the regular fields. In addition, we also need to check if the parameter constraining process is affected by the finite number of realizations in each observable ensemble. To perform a fast and illustrative verification, we propose two toy models which are named as the linear and quadratic model. For the linear model we define an observable y as a function of the (angular) position x

$$y_{\text{linear}}(x) = \cos(x)\mathcal{G}(a, b, s) \,, \tag{4.14}$$

where $\mathcal{G}$ represents a Gaussian distribution with mean value controlled by parameter a, standard deviation controlled by parameter b and random seed controlled by s. The random seed is necessary from the technical point of view, it also defines explicitly the measured mock data or simulated output. As the same modeling is used for generating simulated observable ensembles, s controls each realization precisely

where two realizations with the same seed are identical. Meanwhile, the quadratic model is defined as

$$y_{\text{quadratic}}(x) = [\sin(x)\mathcal{G}(a, b, s)]^2 \ , \tag{4.15}$$

where the major difference from the linear model is that the observable has quadratic dependency (or response) on the random component.

The linear model is designed for mimicking the Faraday rotation phenomenon, where the Faraday depth depends linearly on the random magnetic field and thermal electron density. The quadratic model is designed for mimicking the synchrotron or dust emission, where the random magnetic field energy density plays a major role. It is interesting to notice that the Galactic (co)variance in the linear and quadratic models are dramatically different, as illustrated in the left panels of Figures 4.2 and 4.3. The random component in the linear model provides an extra Gaussian fluctuation, so even if the random field modeling is missing in constraining parameters, i.e., by replacing the $\mathcal{G}$ term by only the constant a in observable simulation, the estimation on a will not be biased but only suffered from a large uncertainty given enough measurements. However this is not true in the quadratic model because the random component contributes to the observable with its variance, and so an incompetent Bayesian analysis will always be biased. In the right panels of Figures 4.2 and 4.3 we demonstrate that IMAGINE is able to retrieve correct estimations on both the regular and random field parameters even when the random component dominates. Since the measurement uncertainty is not important in the testing cases, we set relatively small noise fields for the mock data generations.
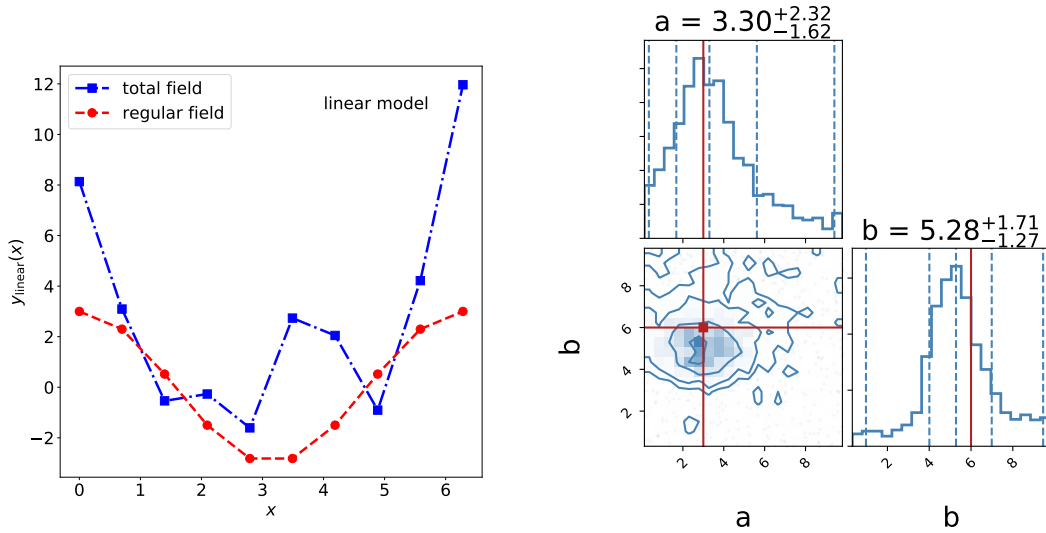

Figure 4.2: Left: Linear model of the mock observable, the random field contributes a Gaussian fluctuation on top of the regular field (red). Right: Parameters of the linear model estimated by IMAGINE, where the true values are marked in red, the dashed lines represents the 2nd, 16th, 5th, 86th and 98th quantiles respectively.

Note that in estimating the parameters with IMAGINE, the simulated observables are produced with the same toy models [4] as described in Eq. 4.14 and Eq. 4.15 while the only difference is that the random

---

[4]Simulating observables with different models than the mock data is an issue about modelling itself, and so independent of the Bayesian analysis.
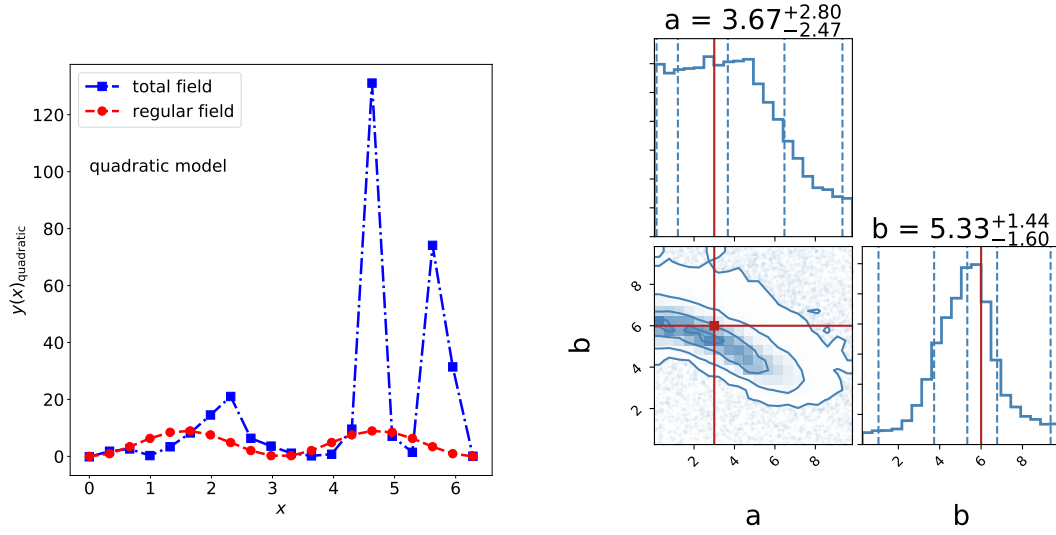
Figure 4.3: Left: Quadratic model of the mock observable, the random field contributes a Gaussian fluctuation on top of the regular field (red). Right: Parameters of the quadratic model estimated by `IMAGINE`, where the true values are marked in red, the dashed lines represents the 2nd, 16th, 5th, 86th and 98th quantiles respectively.

seed for each realization is different. As we are using only a finite number of realizations in each simulation ensemble, we should ensure that this limitation along with the OAS covariance estimator does not bias the parameter estimation. In Fig. 4.4 we repeat the `IMAGINE` estimation pipeline several times with different simulation ensemble sets, and find out the distributions differs from each other slightly (which is reasonable and acceptable) but are statistically highly consistent.
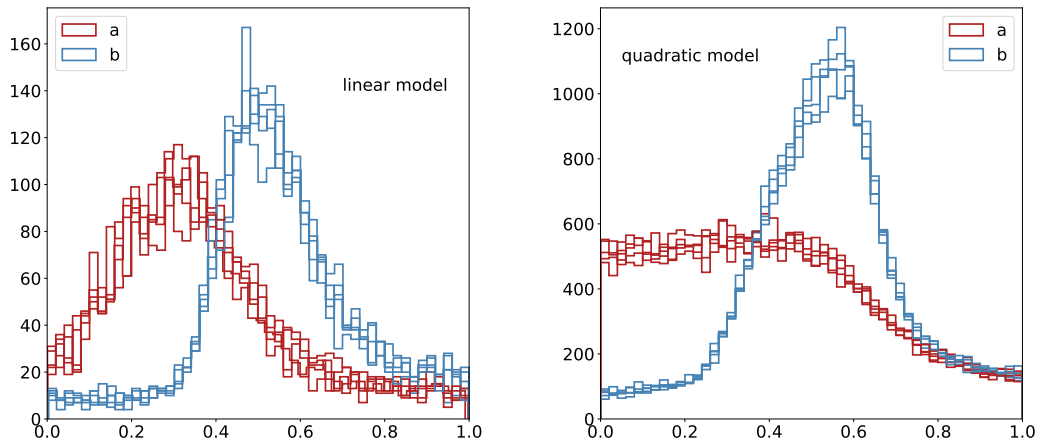

Figure 4.4: Distributions of logical variables corresponds to parameter a and b estimated by `IMAGINE` with different simulation ensemble sets.

With these two simple tests, we can conclude that the `IMAGINE` package and the ensemble likelihood meet our expectation very well and show a promising potential in inferring the turbulent field distribution

from the Galactic emission measurements. For readers who are interested in using `IMAGINE`, the fast testing cases are suitable practicing materials.

4.3   Summary

In this chapter we have presented the complete design of the `IMAGINE` package with MPI support. At the minimal application level, we currently are able to handle the Galactic synchrotron emission and Faraday depth either independently or jointly with `hammurabi X`, while for other observables we need to adjust the interface accordingly. The capability in parameter estimation according to illustrative models has been verified, but not yet profiled in detail. The basic conclusion we can draw is that the Bayesian pipeline works for distinguishing Galactic (co)variance from data noise, and the results appear to be robust with finite simulation ensemble size. The current release is ready and practically feasible for scientific tasks in studying the Galactic emissions with partial-sky real/mock data.

We still see some further improvements can be done in the near future, in order to make the routine practically appropriate for full-sky and high resolution analysis. First of all, we are not extremely satisfied with the log-determinant estimation of the covariance matrix, the performance of this step can directly affect the efficiency and precision of the Bayesian analysis. Secondly, the back-end Bayesian sampler is either written in `FORTRAN` or `Python` which are both not the ideal languages in modern high-performance computing, since `FORTRAN` is not convenient for maintaining while `Python` is practically slow. As a matter of fact, we may not even need the `NIFTy` library support which duplicates the memory consumption at certain places, and so an aggressive upgrade plan can involve rewriting the observable handler (especially for calculations related to the covariance matrices) and the multi-nest sampler in `C++` or `Julia` with better MPI support under the current `IMAGINE` framework. Considering the future application of `IMAGINE`, we emphasize that nested MPI support and even GPU acceleration will be appreciated.

It is also possible to consider including non-parametric modelling analysis and/or machine learning algorithms under the framework, where the interface for handling measured and simulated data sets is generic. For these potential upgrades, we will only have to adjust and specialize part of the current design in the future.

CONCLUSION

In this thesis we have presented three numerical packages prepared for carrying out the idea of consistent analysis for the Galactic synchrotron emission and the physical components associated. First of all, we introduced `hammurabi X` for simulating the Galactic synchrotron emission according to given distributions or descriptions of physical components. The precision and performance of `hammurabi X` is crucial for getting correct observational implications of various Galactic field structures. Then, for removing the repeatedly defined mechanisms or processes and rebuilding the connections among the Galactic components, we proposed the `BIFET` for solving high-dimensional PDE systems. Currently we have finished the basic framework design and tested the solving routine with high-dimensional advection-diffusion examples. According to the testing results we observed that the adaptive mesh refinement works as expected and solution precision scales correctly with mathematical expectation. These two numerical tools are designed to support the consistent simulation pipeline, while for comparing the simulated results with observational measurements we developed `IMAGINE`. By using the ensemble likelihood function and the multi-nest samplers, `IMAGINE` can handle the Galactic (co)variance properly and in turn provide unbiased estimation on model parameters. `hammurabi X` has been integrated inside `IMAGINE` as its default observable simulator, while `BIFET` still needs further improvements due to the complication in solving a non-linear PDE system. As `IMAGINE` has gone through its first upgrade, it becomes feasible to carry out Bayesian analyses for synchrotron emission with independent parametric models of Galactic components.

We have implemented the first phase of our scientific goal, i.e., to analyze the influence of random GMF on the Galactic synchrotron emission. By checking the angular power spectrum of synchrotron polarization at 30 GHz, we find there are multiple reasons for observing B/E < 1.0. With the global random GMF realizations, the synchrotron B/E ratio is affected by the divergence-free property itself which was not expected and even ignored in previous studies. It also shows up with the global realizations that spatial alignment is also responsible for tuning the synchrotron B/E. Meanwhile with the local realizations where parameterized MHD magnetic turbulence is adopted, we find consistent numerical results for synchrotron B/E ratio at perturbative regime where the random GMF strength is much lower than that of the regular field. For both types of realizations, we manage to go beyond the perturbative regime and find evolution in the synchrotron B/E ratio for the first time. This first phase work can be easily extended to include the Galactic dust emission and the first level of consistency we defined in the beginning, and give more useful information of the general properties of the Galactic emissions and their potential correlation which is useful for studying the CMB foreground removal and the distribution of

Galactic components.

For `hammurabi X`, we would like to focus on improving the random GMF generators with more physical features. The alignment of the random GMF around local filaments (including helicity) and non-Gaussianity will be interesting extensions, through which we can study the joint effect of the magnetic field alignment and its spectral anisotropy. In `hammurabi X`, both the global and local generators are designed to allow in the future the addition of non-Gaussianity, e.g., with the method introduced by Vio et al. [2001], helicity, e.g., with the method instructed by Kitaura and Enßlin [2008] and more realistic modeling, e.g., with local filaments studied by Bracco et al. [2018]. We intend to extend `hammurabi X` for further studies of Galactic Faraday rotation, dust emission and free-free absorption by including (where possible) the coupling between the random GMF and the thermal electron and dust distributions implemented in similarly calibrated numeric implementations. For studying the global GMF structure we would also like to include realistic Galactic geometry like the Galactic warp and flare studied by Chen et al. [2019] based on measured Cepheids.

The future plans for technical improvements of `IMAGINE` and `BIFET` have been discussed in the corresponding chapters. `BIFET` is suitable for carrying out fast and precise simulation of CRE propagation with the random magnetic field realizations generated by `hammurabi X`. By doing so, we could try to study the implications of magnetic field in the CMB foreground with a more realistic starting point, e.g., the frequency scaling of synchrotron and dust emissions and the possible correlation between them. `IMAGINE` will be a powerful tool for inferring Galactic components by comparing ensemble simulations of observables. The Galactic random fields, and their effect known as the Galactic (co)variance, have troubled us for many years. Now according to the testing results presented earlier, we feel confident in near future to provide convincing and robust analyses for understanding the observable sensitive properties of the random fields.

We emphasize that our long term project is to combine all three packages together and realize the 2nd level consistency in the Galactic emission analyses. This dissertation can be considered as our numerical efforts which are necessary for non-linear, high-dimension, high-precision and high-resolution studies in the CMB foreground removal and Galactic environment.

Bibliography

Georges Aad et al. A particle consistent with the Higgs Boson observed with the ATLAS Detector at the Large Hadron Collider. *Science*, 338:1576–1582, 2012. doi: 10.1126/science.1232005.

B. P. Abbott et al. Observation of Gravitational Waves from a Binary Black Hole Merger. *Phys. Rev. Lett.*, 116(6):061102, 2016. doi: 10.1103/PhysRevLett.116.061102.

Kazunori Akiyama et al. First M87 Event Horizon Telescope Results. IV. Imaging the Central Supermassive Black Hole. *The Astrophysical Journal*, 875(1):L4, apr 2019. ISSN 2041-8213. doi: 10.3847/2041-8213/ab0e85.

Charles L. H. Hull, Philip Mocz, Blakesley Burkhart, Alyssa A. Goodman, Josep M. Girart, Paulo C. Cortés, Lars Hernquist, Volker Springel, Zhi-Yun Li, and Shih-Ping Lai. Unveiling the Role of the Magnetic Field at the Smallest Scales of Star Formation. *The Astrophysical Journal*, 842(2):L9, jun 2017. ISSN 2041-8213. doi: 10.3847/2041-8213/aa71b7.

A. Aab et al. Observation of a large-scale anisotropy in the arrival directions of cosmic rays above 8×10^{18} eV. *Science*, 357(6357):1266–1270, sep 2017. ISSN 0036-8075. doi: 10.1126/science.aan4338.

S. M. Leach, J.-F. Cardoso, C. Baccigalupi, R. B. Barreiro, M. Betoule, J. Bobin, A. Bonaldi, J. Delabrouille, G. de Zotti, C. Dickinson, H. K. Eriksen, J. González-Nuevo, F. K. Hansen, D. Herranz, M. Le Jeune, M. López-Caniego, E. Martínez-González, M. Massardi, J.-B. Melin, M.-A. Miville-Deschênes, G. Patanchon, S. Prunet, S. Ricciardi, E. Salerno, J. L. Sanz, J.-L. Starck, F. Stivoli, V. Stolyarov, R. Stompor, and P. Vielva. Component separation methods for the PLANCK mission. *Astronomy & Astrophysics*, 491(2):597–615, nov 2008. ISSN 0004-6361. doi: 10.1051/0004-6361:200810116. URL http://www.aanda.org/10.1051/0004-6361:200810116.

Planck Collaboration, Y. Akrami, et al. Planck 2018 results. IV. Diffuse component separation. jul 2018a. URL http://arxiv.org/abs/1807.06208.

Pengjie Zhang, Jun Zhang, and Le Zhang. ABS: an analytical method of blind separation of CMB from foregrounds. *Monthly Notices of the Royal Astronomical Society*, 484(2):1616–1626, apr 2019a. ISSN 0035-8711. doi: 10.1093/mnras/stz091.

P. A. R. Ade et al. Joint Analysis of BICEP2/ Keck Array and Planck Data. *Physical Review Letters*, 114(10):101301, mar 2015. ISSN 0031-9007. doi: 10.1103/PhysRevLett.114.101301.

N. Krachmalnicoff, C. Baccigalupi, J. Aumont, M. Bersanelli, and A. Mennella. Characterization of foreground emission on degree angular scales for CMB B -mode observations. *Astronomy & Astrophysics*, 588:A65, 2016. ISSN 0004-6361. doi: 10.1051/0004-6361/201527678.

M. I. R. Alves, F. Boulanger, K. Ferrière, and L. Montier. The Local Bubble: a magnetic veil to our Galaxy. *Astronomy & Astrophysics*, 611:L5, mar 2018. ISSN 0004-6361. doi: 10.1051/0004-6361/201832637. URL https://www.aanda.org/10.1051/0004-6361/201832637.

R. D. DAVIES, R. S. BOOTH, and A. J. WILSON. Interstellar Magnetic Fields determined from Zeeman Effect Measurements. *Nature*, 220(5173):1207–1210, dec 1968. ISSN 0028-0836. doi: 10.1038/2201207a0.

Vincent L. Fish, Mark J. Reid, Alice L. Argon, and Karl M. Menten. Interstellar Hydroxyl Masers in the Galaxy. II. Zeeman Pairs and the Galactic Magnetic Field. *The Astrophysical Journal*, 596(1):328–343, oct 2003. ISSN 0004-637X. doi: 10.1086/377081.

Georgia V. Panopoulou, Brandon S. Hensley, Raphael Skalidis, Dmitry Blinov, and Konstantinos Tassis. Extreme starlight polarization in a region with highly polarized dust emission. *Astronomy & Astrophysics*, 624:L8, apr 2019. ISSN 0004-6361. doi: 10.1051/0004-6361/201935266.

N. Oppermann et al. An improved map of the Galactic Faraday sky. *Astronomy & Astrophysics*, 542:A93, jun 2012. ISSN 0004-6361. doi: 10.1051/0004-6361/201118526.

Sebastian Hutschenreuter, Sebastian Dorn, Jens Jasche, Franco Vazza, Daniela Paoletti, Guilhem Lavaux, and Torsten A. Enßlin. The primordial magnetic field in our cosmic backyard. *Classical and Quantum Gravity*, 35(15):154001, mar 2018. ISSN 13616382. doi: 10.1088/1361-6382/aacde0.

Insu Han, Dmitry Malioutov, and Jinwoo Shin. Large-scale Log-determinant Computation through Stochastic Chebyshev Expansions. mar 2015.

M. A. Brentjens and A. G. de Bruyn. Faraday rotation measure synthesis. *Astronomy & Astrophysics*, 441(3):1217–1228, oct 2005. ISSN 0004-6361. doi: 10.1051/0004-6361:20052990.

S. E. Clark, J. E.G. Peek, and M. E. Putman. Magnetically aligned H i fibers and the rolling hough transform. *Astrophysical Journal*, 789(1), 2014. ISSN 15384357. doi: 10.1088/0004-637X/789/1/82.

S. E. Clark, J. Colin Hill, J. E.G. Peek, M. E. Putman, and B. L. Babler. Neutral Hydrogen Structures Trace Dust Polarization Angle: Implications for Cosmic Microwave Background Foregrounds. *Physical Review Letters*, 115(24), 2015. ISSN 10797114. doi: 10.1103/PhysRevLett.115.241302.

S. E. Clark. A New Probe of Line-of-sight Magnetic Field Tangling. *The Astrophysical Journal*, 857(1):L10, apr 2018. ISSN 2041-8213. doi: 10.3847/2041-8213/aabb54.

A. Lazarian, Ka Ho Yuen, Hyeseung Lee, and J. Cho. Synchrotron Intensity Gradients as Tracers of Interstellar Magnetic Fields. *The Astrophysical Journal*, 842(1):30, 2017. doi: 10.3847/1538-4357/aa74c6.

Luke Chamandy, Anvar Shukurov, and A. Russ Taylor. STATISTICAL TESTS OF GALACTIC DY-NAMO THEORY. *The Astrophysical Journal*, 833(1):43, 2016. doi: 10.3847/1538-4357/833/1/43.

Paul Charbonneau. Solar Dynamo Theory. *Annual Review of Astronomy and Astrophysics*, 52(1):251–290, aug 2014. ISSN 0066-4146. doi: 10.1146/annurev-astro-081913-040012.

Ramon Khanna. Generation of magnetic fields by a gravitomagnetic plasma battery. *Monthly Notices of the Royal Astronomical Society*, 295(1):L6–L10, mar 1998. ISSN 00358711. doi: 10.1046/j.1365-8711.1998.29511447.x.

E. N. Parker. The Dynamical State of the Interstellar Gas and Field. *The Astrophysical Journal*, 145:811, sep 1966. ISSN 0004-637X. doi: 10.1086/148828.

Evan Heintz and Ellen G. Zweibel. The Parker Instability with Cosmic Ray Streaming. *The Astrophysical Journal*, 860(2):97, mar 2018. ISSN 1538-4357. doi: 10.3847/1538-4357/aac208.

J.L. Han. Observing Interstellar and Intergalactic Magnetic Fields. *Annual Review of Astronomy and Astrophysics*, 55(1):111–157, aug 2017. ISSN 0066-4146. doi: 10.1146/annurev-astro-091916-055221.

Hua-bai Li, Min Fang, Thomas Henning, and Jouni Kainulainen. The Link between Magnetic Fields and Filamentary Clouds: Bimodal Cloud Orientations in the Gould Belt. *Monthly Notices of the Royal Astronomical Society*, 436(4):3707–3719, oct 2013. ISSN 00358711. doi: 10.1093/mnras/stt1849.

Y. Zhang, Z. Guo, H. H. Wang, and H-b Li. Anchoring Magnetic Fields in Turbulent Molecular Clouds. II. From 0.1 to 0.01 pc. *The Astrophysical Journal*, 871(1):98, jan 2019b. ISSN 1538-4357. doi: 10.3847/1538-4357/aaf57c.

L. Page et al. Three-year wilkinson microwave anisotropy probe (wmap) observations: Polarization analysis. *The Astrophysical Journal Supplement Series*, 170(2):335, 2007.

X. H. Sun, W. Reich, A. Waelkens, and T. A. Enßlin. Radio observational constraints on Galactic 3D-emission models. *Astronomy & Astrophysics*, 477(2):573–592, jan 2008. ISSN 0004-6361. doi: 10.1051/0004-6361:20078671.

T. R. Jaffe, J. P. Leahy, A. J. Banday, S. M. Leach, S. R. Lowe, and A. Wilkinson. Modelling the Galactic magnetic field on the plane in two dimensions. *Monthly Notices of the Royal Astronomical Society*, 401(2):1013–1028, jan 2010. ISSN 00358711. doi: 10.1111/j.1365-2966.2009.15745.x.

T. R. Jaffe, K. M. Ferrière, A. J. Banday, A. W. Strong, E. Orlando, J. F. Macías-Pérez, L. Fauvet, C. Combet, and E. Falgarone. Comparing polarized synchrotron and thermal dust emission in the galactic plane. *Monthly Notices of the Royal Astronomical Society*, 431(1):683–694, feb 2013. ISSN 00358711. doi: 10.1093/mnras/stt200.

Ronnie Jansson and Glennys R. Farrar. A NEW MODEL OF THE GALACTIC MAGNETIC FIELD. *The Astrophysical Journal*, 757(1):14, sep 2012a. ISSN 0004-637X. doi: 10.1088/0004-637X/757/1/14.

Xiao-Hui Sun and Wolfgang Reich. The Galactic halo magnetic field revisited. *Research in Astronomy and Astrophysics*, 10(12):1287–1297, dec 2010. ISSN 1674-4527. doi: 10.1088/1674-4527/10/12/009.

Katia Ferrière and Philippe Terral. Analytical models of X-shape magnetic fields in galactic halos. *Astronomy & Astrophysics*, 561:A100, jan 2014. ISSN 0004-6361. doi: 10.1051/0004-6361/201322966.

Philippe Terral and Katia Ferrière. Constraints from Faraday rotation on the magnetic field structure in the Galactic halo. *Astronomy & Astrophysics*, 600:A29, apr 2017. ISSN 0004-6361. doi: 10.1051/0004-6361/201629572.

Anvar Shukurov. Introduction to galactic dynamos. nov 2004.

Anvar Shukurov, Luiz Felipe S. Rodrigues, Paul J. Bushby, James Hollins, and Jörg P. Rachen. A physical approach to modelling large-scale galactic magnetic fields. *Astronomy & Astrophysics*, 623:A113, mar 2019. ISSN 0004-6361. doi: 10.1051/0004-6361/201834642.

Ronnie Jansson and Glennys R. Farrar. The Galactic Magnetic Field. *The Astrophysical Journal*, 761(1):L11, oct 2012b. ISSN 2041-8205. doi: 10.1088/2041-8205/761/1/L11.

Marcus C. Beck, Alexander M. Beck, Rainer Beck, Klaus Dolag, Andrew W. Strong, and Peter Nielaba. New constraints on modelling the random magnetic field of the MW. *Journal of Cosmology and Astroparticle Physics*, 2016(5):056–056, may 2016. ISSN 14757516. doi: 10.1088/1475-7516/2016/05/056.

F. Vansyngel, F. Boulanger, T. Ghosh, B. Wandelt, J. Aumont, A. Bracco, F. Levrier, P. G. Martin, and L. Montier. Statistical simulations of the dust foreground to cosmic microwave background polarization (Corrigendum). *Astronomy & Astrophysics*, 618:C4, oct 2018. ISSN 0004-6361. doi: 10.1051/0004-6361/201629992e.

Robert R. Caldwell, Chris Hirata, and Marc Kamionkowski. Dust polarization and ISM turbulence. *The Astrophysical Journal*, 839(2):91, apr 2016. ISSN 1538-4357. doi: 10.3847/1538-4357/aa679c.

D. Kandel, A. Lazarian, and D. Pogosyan. Can the observed e/b ratio for dust galactic foreground be explained by sub-alfvénic turbulence? *Monthly Notices of the Royal Astronomical Society: Letters*, 472(1):L10–L14, 2017. doi: 10.1093/mnrasl/slx128.

D. Kandel, A. Lazarian, and D. Pogosyan. Statistical properties of Galactic CMB foregrounds: Dust and synchrotron. *Monthly Notices of the Royal Astronomical Society*, 478(1):530–540, nov 2018. ISSN 13652966. doi: 10.1093/mnras/sty1115.

A. Pouquet, U. Frisch, and J. Léorat. Strong MHD helical turbulence and the nonlinear dynamo effect. *Journal of Fluid Mechanics*, 77(2):321–354, sep 1976. ISSN 0022-1120. doi: 10.1017/S0022112076002140.

Axel Brandenburg, Andrea Bracco, Tina Kahniashvili, Sayan Mandal, Alberto Roper Pol, Gordon J. D. Petrie, and Nishant K. Singh. E and B Polarizations from Inhomogeneous and Solar Surface Turbulence. *The Astrophysical Journal*, 870(2):87, jul 2019. doi: 10.3847/1538-4357/aaf383.

Jungyeon Cho and A. Lazarian. Compressible sub-alfvénic mhd turbulence in low- β plasmas. *Phys. Rev. Lett.*, 88:245001, May 2002. doi: 10.1103/PhysRevLett.88.245001.

George B. Rybicki and Alan P. Lightman. *Radiative processes in astrophysics*. Wiley, 1979. ISBN 0471827592.

A. Waelkens, T. Jaffe, M. Reinecke, F. S. Kitaura, and T. A. Enßlin. Simulating polarized Galactic synchrotron emission at all frequencies. *Astronomy & Astrophysics*, 495(2):697–706, feb 2009. ISSN 0004-6361. doi: 10.1051/0004-6361:200810564.

K. Dolag, B. M. Gaensler, A. M. Beck, and M. C. Beck. Constraints on the distribution and energetics of fast radio bursts using cosmological hydrodynamic simulations. *Monthly Notices of the Royal Astronomical Society*, 451(4):4277–4289, dec 2015. ISSN 13652966. doi: 10.1093/mnras/stv1190.

Eric R. Switzer and Adrian Liu. Erasing the variable: Empirical foreground discovery for global 21 cm spectrum experiments. *Astrophysical Journal*, 793(2), apr 2014. ISSN 15384357. doi: 10.1088/0004-637X/793/2/102.

J. L. West, T. Jaffe, G. Ferrand, S. Safi-Harb, and B. M. Gaensler. When Disorder Looks Like Order: A New Model to Explain Radial Magnetic Fields in Young Supernova Remnants. *The Astrophysical Journal*, 849(2):L22, nov 2017. doi: 10.3847/2041-8213/aa94c4.

R. Adam et al. Planck intermediate results. *Astronomy & Astrophysics*, 596:A104, jan 2016. ISSN 0004-6361. doi: 10.1051/0004-6361/201628522.

Takuya Akahori, Dongsu Ryu, Jongsoo Kim, and B. M. Gaensler. Simulated faraday rotation measures toward high galactic latitudes. *Astrophysical Journal*, 767(2), mar 2013. ISSN 15384357. doi: 10.1088/0004-637X/767/2/150.

Alexei G. Kritsuk, Raphael Flauger, and Sergey D. Ustyugov. Dust-Polarization Maps for Local Interstellar Turbulence. *Physical Review Letters*, 121(2), nov 2018. ISSN 10797114. doi: 10.1103/PhysRevLett.121.021104.

François Boulanger et al. IMAGINE: a comprehensive view of the interstellar medium, Galactic magnetic fields and cosmic rays. *Journal of Cosmology and Astroparticle Physics*, 2018(08):49, 2018.

K. M. Gorski, E. Hivon, A. J. Banday, B. D. Wandelt, F. K. Hansen, M. Reinecke, and M. Bartelmann. HEALPix: A Framework for High-Resolution Discretization and Fast Analysis of Data Distributed on the Sphere. *The Astrophysical Journal*, 622(2):759–771, apr 2005. ISSN 0004-637X. doi: 10.1086/427976.

Andrew W. Strong and Igor V. Moskalenko. Propagation of Cosmic-Ray Nucleons in the Galaxy. *The Astrophysical Journal*, 509(1):212–228, dec 1998. ISSN 0004-637X. doi: 10.1086/306470.

Carmelo Evoli, Daniele Gaggero, Andrea Vittino, Giuseppe Di Bernardo, Mattia Di Mauro, Arianna Ligorini, Piero Ullio, and Dario Grasso. Cosmic-ray propagation with DRAGON2: I. numerical solver

and astrophysical ingredients. *Journal of Cosmology and Astroparticle Physics*, 2017(02):015–015, feb 2017. ISSN 1475-7516. doi: 10.1088/1475-7516/2017/02/015.

Reinhard Schlickeiser. *Cosmic ray astrophysics.* Springer, 2002. ISBN 3540664653.

Gene M. Amdahl. Validity of the single processor approach to achieving large scale computing capabilities. In *Proceedings of the April 18-20, 1967, spring joint computer conference on - AFIPS '67 (Spring)*, page 483, New York, New York, USA, 1967. ACM Press. doi: 10.1145/1465482.1465560.

Joao Alves, Françoise Combes, Andrea Ferrara, Thierry Forveille, and Steve Shore. Planck 2015 results. *Astronomy & Astrophysics*, 594:E1, feb 2016. ISSN 0004-6361. doi: 10.1051/0004-6361/201629543.

Planck Collaboration, P. A. R. Ade, et al. Planck 2015 results. XXV. Diffuse low-frequency Galactic foregrounds. *Astronomy & Astrophysics*, 594:A25, jun 2015. ISSN 0004-6361. doi: 10.1051/0004-6361/201526803.

David Alonso, Javier Sanchez, and Anže Slosar. A unified pseudo - C_ℓ framework. *Monthly Notices of the Royal Astronomical Society*, 484(3):4127–4151, apr 2019. ISSN 0035-8711. doi: 10.1093/mnras/stz093.

Wayne Hu and Martin White. CMB anisotropies: Total angular momentum method. *Physical Review D*, 56(2):596–615, jul 1997. ISSN 0556-2821. doi: 10.1103/PhysRevD.56.596.

Wayne Hu. Reionization Revisited: Secondary Cosmic Microwave Background Anisotropies and Polarization. *The Astrophysical Journal*, 529(1):12–25, jan 2000. ISSN 0004-637X. doi: 10.1086/308279.

Siyao Xu and Bing Zhang. INTERPRETATION OF THE STRUCTURE FUNCTION OF ROTATION MEASURE IN THE INTERSTELLAR MEDIUM. *The Astrophysical Journal*, 824(2):113, apr 2016. doi: 10.3847/0004-637x/824/2/113.

Marilena LoVerde and Niayesh Afshordi. Extended Limber approximation. *Physical Review D*, 78(12):123506, dec 2008. ISSN 1550-7998. doi: 10.1103/PhysRevD.78.123506.

Jens Keiner, Stefan Kunis, and Daniel Potts. Using NFFT 3—A Software Library for Various Nonequispaced Fast Fourier Transforms. *ACM Transactions on Mathematical Software*, 36(4):1–30, aug 2009. ISSN 00983500. doi: 10.1145/1555386.1555388.

Pasquale Blasi, Elena Amato, and Pasquale D. Serpico. Spectral breaks as a signature of cosmic ray induced turbulence in the Galaxy. *Physical Review Letters*, 109(6):061101, jul 2012. ISSN 0031-9007. doi: 10.1103/PhysRevLett.109.061101.

Carmelo Evoli, Pasquale Blasi, Giovanni Morlino, and Roberto Aloisio. Origin of the Cosmic Ray Galactic Halo Driven by Advected Turbulence and Self-Generated Waves. *Physical Review Letters*, 121(2):021102, jul 2018. ISSN 0031-9007. doi: 10.1103/PhysRevLett.121.021102.

C. Pfrommer, R. Pakmor, K. Schaal, C. M. Simpson, and V. Springel. Simulating cosmic ray physics on a moving mesh. *Monthly Notices of the Royal Astronomical Society*, 465(4):4500–4529, mar 2017. ISSN 13652966. doi: 10.1093/mnras/stw2941.

Mateusz Ruszkowski, H. Y. Karen Yang, and Ellen Zweibel. Global simulations of galactic winds including cosmic ray streaming. *The Astrophysical Journal*, 834(2):208, feb 2016. ISSN 1538-4357. doi: 10.3847/1538-4357/834/2/208.

R. Farber, M. Ruszkowski, H. Y. K. Yang, and E. G. Zweibel. Impact of Cosmic Ray Transport on Galactic Winds. *The Astrophysical Journal*, 856(2):112, jul 2017. ISSN 1538-4357. doi: 10.3847/1538-4357/aab26d.

Joshua Wiener, S. Peng Oh, and Ellen G. Zweibel. Interaction of Cosmic Rays with Cold Clouds in Galactic Halos. *Monthly Notices of the Royal Astronomical Society*, 467(1):stx109, oct 2016. ISSN 0035-8711. doi: 10.1093/mnras/stx109.

M. J. Rees. Proton Synchrotron Emission from Compact Radio Sources. *Astrophysical Letters*, 2:1, 1968.

R. Kissmann. PICARD: A novel code for the Galactic Cosmic Ray propagation problem. *Astroparticle Physics*, 55(9):37–50, mar 2014. ISSN 09276505. doi: 10.1016/j.astropartphys.2014.02.002.

Rafael Alves Batista et al. CRPropa 3—a public astrophysical simulation framework for propagating extraterrestrial ultra-high energy particles. *Journal of Cosmology and Astroparticle Physics*, 2016(05):038–038, may 2016. ISSN 1475-7516. doi: 10.1088/1475-7516/2016/05/038.

Andrew W. Strong, Igor V. Moskalenko, and Vladimir S. Ptuskin. Cosmic-ray propagation and interactions in the Galaxy. *Annual Review of Nuclear and Particle Science*, 57(1):285–327, jan 2007. ISSN 0163-8998. doi: 10.1146/annurev.nucl.57.090506.123011.

Isabelle A. Grenier, John H. Black, and Andrew W. Strong. The Nine Lives of Cosmic Rays in Galaxies. *Annual Review of Astronomy and Astrophysics*, 53(1):199–246, aug 2015. ISSN 0066-4146. doi: 10.1146/annurev-astro-082214-122457.

M. Tanabashi et al. Review of Particle Physics. *Physical Review D*, 98(3):030001, aug 2018. ISSN 2470-0010. doi: 10.1103/PhysRevD.98.030001.

M. Di Mauro, F. Donato, N. Fornengo, R. Lineros, and A. Vittino. Interpretation of AMS-02 electrons and positrons data. *Journal of Cosmology and Astroparticle Physics*, 2014(04):006–006, apr 2014. ISSN 1475-7516. doi: 10.1088/1475-7516/2014/04/006.

C. C. Popescu, R. Yang, R. J. Tuffs, G. Natale, M. Rushton, and F. Aharonian. A radiation transfer model for the Milky Way: I. Radiation fields and application to high-energy astrophysics. *Monthly Notices of the Royal Astronomical Society*, 470(3):2539–2558, sep 2017. ISSN 0035-8711. doi: 10.1093/mnras/stx1282.

R. M. Kulsrud and C. J. Cesarsky. The Effectiveness of Instabilities for the Confinement of High Energy Cosmic Rays in the Galactic Disk. *Astrophysical Letters*, 8:189, March 1971.

Dan Hooper, Pasquale Blasi, and Pasquale Dario Serpico. Pulsars as the sources of high energy cosmic ray positrons. *Journal of Cosmology and Astroparticle Physics*, 2009(01):025–025, jan 2009. ISSN 1475-7516. doi: 10.1088/1475-7516/2009/01/025.

GIANFRANCO BRUNETTI and THOMAS W. JONES. COSMIC RAYS IN GALAXY CLUSTERS
AND THEIR NONTHERMAL EMISSION. *International Journal of Modern Physics D*, 23(04):
1430007, mar 2014. ISSN 0218-2718. doi: 10.1142/s0218271814300079.

Jingjing Chen, Greg L. Bryan, and Munier Salem. Cosmological simulations of dwarf galaxies with
cosmic ray feedback. *Monthly Notices of the Royal Astronomical Society*, 460(3):3335–3344, 2016.
ISSN 13652966. doi: 10.1093/mnras/stw1197.

A. Burkert. The Structure of Dark Matter Halos in Dwarf Galaxies. *Symposium - International Astro-
nomical Union*, 171(1):175–178, jul 1996. ISSN 0074-1809. doi: 10.1017/s0074180900232324.

J.T. Oden and S. Prudhomme. Goal-oriented error estimation and adaptivity for the finite element
method. *Computers & Mathematics with Applications*, 41(5-6):735–756, mar 2001. ISSN 08981221.
doi: 10.1016/S0898-1221(00)00317-5.

C L Bennett, D Larson, J L Weiland, N Jarosik, G Hinshaw, N Odegard, K M Smith, R S Hill, B Gold,
M Halpern, E Komatsu, M R Nolta, L Page, D N Spergel, E Wollack, J Dunkley, A Kogut, M Limon,
S S Meyer, G S Tucker, and E L Wright. NINE-YEAR WILKINSON MICROWAVE ANISOTROPY
PROBE (WMAP) OBSERVATIONS: FINAL MAPS AND RESULTS. *The Astrophysical Journal
Supplement Series*, 208(2):20, sep 2013. ISSN 0067-0049. doi: 10.1088/0067-0049/208/2/20.

Planck Collaboration, Y. Akrami, et al. Planck 2018 results. I. Overview and the cosmological legacy of
Planck. jul 2018b.

R. Keisler et al. A MEASUREMENT OF THE DAMPING TAIL OF THE COSMIC MICROWAVE
BACKGROUND POWER SPECTRUM WITH THE SOUTH POLE TELESCOPE. *The Astrophysical
Journal*, 743(1):28, dec 2011. ISSN 0004-637X. doi: 10.1088/0004-637X/743/1/28.

L. Fauvet, J. F. Macías-Pérez, J. Aumont, F. X. Désert, T. R. Jaffe, A. J. Banday, M. Tristram, A. H.
Waelkens, and D. Santos. Joint 3D modelling of the polarized Galactic synchrotron and thermal dust
foreground diffuse emission. *Astronomy & Astrophysics*, 526:A145, feb 2011. ISSN 0004-6361. doi:
10.1051/0004-6361/201014492.

Y. Chen, A. Wiesel, and A. O. Hero. Robust Shrinkage Estimation of High-Dimensional Covariance
Matrices. *IEEE Transactions on Signal Processing*, 59:4097–4107, September 2011. doi: 10.1109/TSP.
2011.2138698.

F. Feroz, M. P. Hobson, and M. Bridges. MultiNest: an efficient and robust Bayesian inference tool for
cosmology and particle physics. *Monthly Notices of the Royal Astronomical Society*, 398(4):1601–1614,
oct 2009. ISSN 00358711. doi: 10.1111/j.1365-2966.2009.14548.x.

J. Skilling. Nested sampling for general bayesian computation. *Bayesian Analysis*, 1:833–860, 2006.

Roberto Vio, Paola Andreani, and Willem Wamsteker. Numerical Simulation of Non-Gaussian Random
Fields with Prescribed Correlation Structure. *Publications of the Astronomical Society of the Pacific*,
113(786):1009–1020, aug 2001. ISSN 0004-6280. doi: 10.1086/322919.

F. S. Kitaura and T. A. Enßlin. Bayesian reconstruction of the cosmological large-scale structure: Methodology, inverse algorithms and numerical optimization. *Monthly Notices of the Royal Astronomical Society*, 389(2):497–544, sep 2008. ISSN 00358711. doi: 10.1111/j.1365-2966.2008.13341.x.

A. Bracco, S. Candelaresi, F. Del Sordo, and A. Brandenburg. Is there a left-handed magnetic field in the solar neighborhood? *Astronomy & Astrophysics*, 621:A97, jan 2018. ISSN 0004-6361. doi: 10.1051/0004-6361/201833961.

Xiaodian Chen, Shu Wang, Licai Deng, Richard de Grijs, Chao Liu, and Hao Tian. An intuitive 3D map of the Galactic warp's precession traced by classical Cepheids. *Nature Astronomy*, 3(4):320–325, apr 2019. ISSN 2397-3366. doi: 10.1038/s41550-018-0686-7.

Axel Brandenburg, Tina Kahniashvili, and Alexander G. Tevzadze. Nonhelical inverse transfer of a decaying turbulent magnetic field. *Physical Review Letters*, 114(7):075001, feb 2015. ISSN 10797114. doi: 10.1103/PhysRevLett.114.075001.

Joshua S Speagle. dynesty: A Dynamic Nested Sampling Package for Estimating Bayesian Posteriors and Evidences. apr 2019.

Ellen G. Zweibel. The microphysics and macrophysics of cosmic rays. *Physics of Plasmas*, 20(5):055501, may 2013. ISSN 1070-664X. doi: 10.1063/1.4807033.

J. E. G. Peek and Blakesley Burkhart. Do Androids Dream of Magnetic Fields? Using Neural Networks to Interpret the Turbulent Interstellar Medium. may 2019.